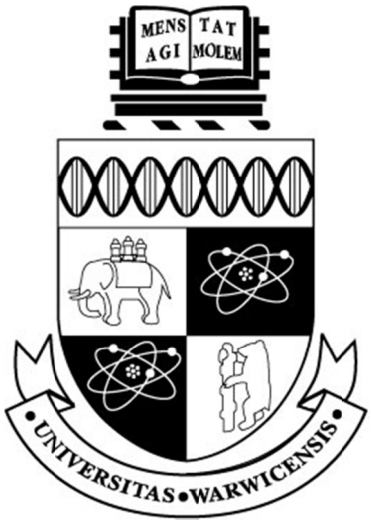

Structure and Applications of Chemically Modified Graphene

by

Priyanka Ajay Pandey

Thesis

Submitted to the University of Warwick
for the degree of

Doctor of Philosophy

Department of Physics

November 2012

THE UNIVERSITY OF
WARWICK

Contents

List of Tables

List of Figures

Acknowledgments

I would like to express my sincere thanks to my supervisor Dr. Neil R. Wilson for his tremendous guidance throughout this work. I really appreciate his willingness to answer my every question, his patience during my PhD and in going through several drafts of my thesis.

I would like to thank all my collaborators for help with all the work in this thesis. Firstly, I would like to extend my thanks to Dr. Richard Beanland, Dr. Jeremy Sloan, and Dr. Ana Sanchez for my training on the microscopes and the helpful discussions. I would like to thank Dr. Gavin Bell for the help with X-ray Photoelectron Spectroscopy. I would also like to thank Steve York for my training and technical support during this work. The interdisciplinary nature of my work involved collaborations with Dr. Jon Rourke from department of Chemistry and Dr. James Covington from the School of Engineering, University of Warwick. I am grateful for their patience in training me and letting me use their lab facilities. I have also received technical support from Rob Johnston and Dr. Sue Burrows from the Department of Physics and Frank Courtney and Ian Griffith form the School of Engineering. I am thankful to Midlands Physics Alliance Graduate School for funding my PhD.

I would like to thank Adam Dyson for solving all my problems with Mathematica. Special thanks to all the members in our office; Assma Wahra, Adam Dyson, Alex Marsden, Volker Keinhorst, Keith Evans, Reza Kashtiban, Steve Hindmarsh and Steve York for their invaluable help and keeping the office atmosphere positive and lively. Big thanks to

Catarina Casteleiro, John Halpin, Alan Burtan, Natalia Parzyk and Amna Hassan for making the lunch times enjoyable.

Finally I would like to thank my Husband (Ajay Pandey) and my parents (Krishna Prabhat Mishra and Rekha Mishra) whose boundless support has made this work possible. I want to thank all my family members for keeping patience and encouraging me throughout my PhD. I would like to dedicate this thesis to my son (Shivan Pandey) who is the greatest joy in my life.

Declarations

This thesis is submitted to the University of Warwick in partial fulfilment of the requirements for the degree of Doctor of Philosophy. I declare that this thesis contains an account of my own work, except where otherwise specifically indicated, performed at the University of Warwick under the supervision of Dr. Neil R. Wilson between October 2008 to October 2012.

The samples of chemically modified graphenes (CMGs) were synthesized in collaboration with Dr. Jonathan P. Rourke, Department of Chemistry, University of Warwick. The sensor measurements were carried out in collaboration with Dr. James A. Covington, School of Engineering, University of Warwick. The samples of fluorinated copper phthalocyanine-CMG were fabricated in collaboration with Prof. Tim S. Jones, Department of Chemistry, University of Warwick. Part of the metal-CMG samples was prepared in collaboration with Prof. Brian J. Hickey, School of Physics and Astronomy, University of Leeds. The metal-CMG results were analysed in collaboration with Dr. Gavin R. Bell, Department of Physics, University of Warwick

No part of this thesis has been submitted for examination at any other institution.

Parts of this work have been published or submitted for publication:

- Pandey, P. A.; Wilson, N. R.; Covington, J. A., Pd-Doped Reduced Graphene Oxide Sensing Films for H_2 Detection. Sensors and Actuators B Submitted.
- Pandey, P. A.; Rochford, L. A.; Keeble, D. S.; Rourke, J. P.; Jones, T. S.; Beanland, R.; Wilson, N. R., Resolving the Nanoscale Morphology and Crystallographic

Structure of Molecular Thin Films: F_{16}CuPc on Graphene Oxide. Chemistry of Materials 2012, 24, 1365-1370.

- Pandey, P. A.; Bell, G. R.; Rourke, J. P.; Sanchez, A. M.; Elkin, M. D.; Hickey, B. J.; Wilson, N. R., Physical Vapor Deposition of Metal Nanoparticles on Chemically Modified Graphene: Observations on Metal–Graphene Interactions. Small 2011, 7, 3202-3210.

- Rourke, J. P.; Pandey, P. A.; Moore, J. J.; Bates, M.; Kinloch, I. A.; Young, R. J.; Wilson, N. R., The Real Graphene Oxide Revealed: Stripping the Oxidative Debris from the Graphene-like Sheets. Angewandte Chemie International Edition 2011, 50, 3173-3177

- Wilson, N. R.; Pandey, P. A.; Beanland, R.; Rourke, J. P.; Umberto., L.; Rowlands, G.; Römer, R. A., On the structure and topography of free-standing chemically modified graphene. New Journal of Physics 2010, 12, 125010.

- Pandey, P. A., Chemically Modified Graphene: An ultrathin support film for transmission electron microscopy. Infocus 2010, 19, 59-65.

- Wilson, N. R.; Pandey, P. A.; Beanland, R.; Young, R. J.; Kinloch, I. A.; Gong, L.; Liu, Z.; Suenaga, K.; Rourke, J. P.; York, S. J.; Sloan, J., Graphene Oxide: Structural Analysis and Application as a Highly Transparent Support for Electron Microscopy. ACS Nano 2009, 3, 2547-2556.

Parts of this work have been presented by the present author at national and international conferences:

Oral presentations

- Pd-on-Graphene: A Sensitive, Selective, Hydrogen Gas Sensor – NanoteC, France, 2011

- Thin Film Growth on Chemically Modified Graphene – NanoteC, UK, 2010

- Structure and Morphology of Organic Thin Films on Chemically Modified Graphene – Condensed Matter and Materials Physics Conference, UK, 2010

- Chemically Modified Graphene: Structural Analysis and Applications – Condensed Matter and Materials Physics Conference, UK, 2009

Poster presentations

- Physical Vapour Deposition of Metal Nanoparticles on Chemically Modified Graphene, and their Application for Hydrogen Sensing – Graphene, Spain, 2011

- Thin films on Chemically Modified Graphene – Microscience, UK, 2010

Abstract

Owing to its extraordinary electrical, optical, and mechanical properties, graphene has emerged as a promising material for a variety of applications in the future. However, not all these applications will be able to employ or require pristine graphene; hence several alternative methods have developed for the mass production of graphene and related materials. Graphene oxide (GO), a material closely related to graphene, allows engineering of its chemical composition by means of chemical, thermal, and electrochemical methods. This provides an opportunity to tune physical and chemical properties of graphene. This work reports on investigations of the structure of chemically modified graphenes (CMGs) derived from GO, interactions of metals and organic thin films with CMG, and application of metal-CMG as a hydrogen gas sensor.

GO was fabricated by a modified Hummers method. GO, being insulating, was reduced by hydrazine and thermal annealing to produce reduced graphene oxide (rGO). The CMG sheets were deposited on TEM grids and on Si/SiO_2 substrates for characterization by atomic force microscopy, transmission electron microscopy (TEM), x-ray photoelectron spectroscopy, and Raman spectroscopy. The structural analysis of GO performed by TEM revealed that in GO, on average, the underlying carbon lattice maintains the symmetry and lattice-spacings of graphene. Compositional analysis disclosed that the as-produced GO is actually made of oxidized graphene like sheets strongly attached with oxidative debris that make the as produced GO hydrophilic and insulating.

In the TEM, both GO and reduced GO (rGO) were nearly transparent and stable under the electron beam and hence they made excellent supports to study the growth of thin organic and metal films deposited by physical vapour deposition. The study revealed the interactions of organic molecules, fluorinated copper phthalocyanine, with CMG and packing of the molecules in the crystal structure. Film-thicknesses from sub-monolayer to tens of monolayers were analysed. In the study of metal thin film growth, the factors determining the growth and morphology of different metals-on-CMG were studied. Fine control over the size and coverage of nanoparticles were achieved. This control was used to combine Pd nanoparticles and rGO to design selective, highly sensitive, and practical hydrogen gas sensor.

Chapter 1. **Introduction**

Graphene, a layer of carbon atoms arranged in a 2 dimensional (2D) hexagonal lattice, has recently gained a great amount of attention from the research communities all over the world. The research is not limited to a particular field, but instead involves interests from physics, chemistry, engineering, material science as well as biology.[1-3] The explosion of research is due to the unique electrical and optical properties arising from the 2D crystal structure of the sp^2 carbon atoms.[4] Although the concept of 'graphene' has existed as a layer of graphite and has been studied theoretically for more than 60 years,[5] experimental studies on the material's properties gained impetus after the fabrication of free standing graphene by Geim and co-workers in 2004.[4] Previously, it was believed that strictly 2D materials should not exist as they are thermodynamically unstable.[4] As a result, although the other forms of sp^2 carbon structures i.e. graphite (3D), carbon nanotubes (3D) and fullerenes (0D) (*Figure 1.1*) have been discovered and studied for decades, the studies

on 2D graphene were limited to mostly theoretical aspects. Although surface scientists have previously reported the growth of 2D graphene layers on metals[6] the fabrication of free standing graphene layers remained challenging for a long time.

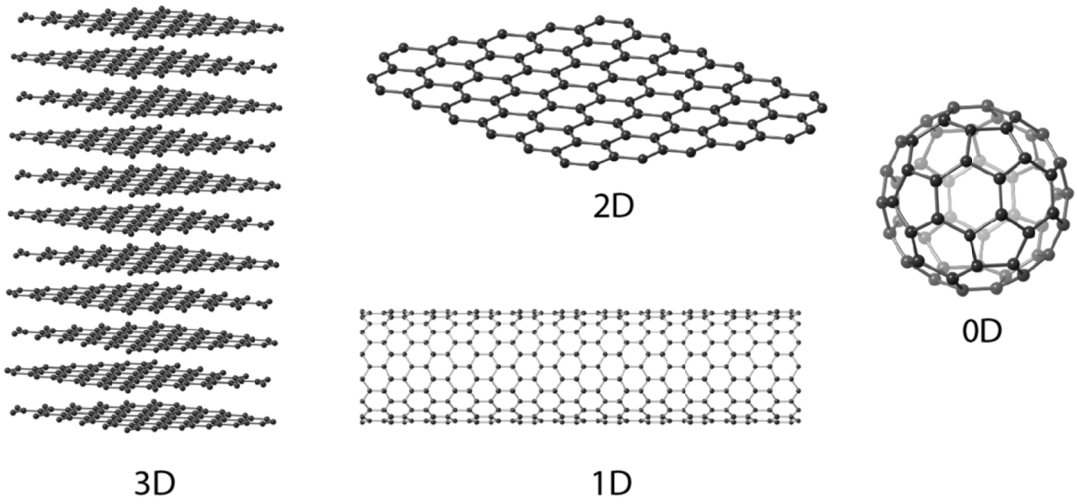

Figure 1.1 Crystal structures of different sp^2 carbon allotropes – (3D) graphite, (2D) graphene, (1D) carbon nanotube and (0D) fullerene molecule. The models were made using Crystal Maker ™.

Carbon structures with sp^2 bonds are extraordinary as they can form assemblies with every dimensionality (0 – 3D). Graphene is the basis for the study of structure of graphite, carbon nanotubes, and fullerenes and hence turns out to be the most studied of all the sp^2 carbon structures.[7] As a result, with the production of free standing graphene, it was quickly picked up by the researchers already working on other forms of sp^2 carbon structures.

It has been demonstrated that graphene possesses exceptionally high charge carrier mobility (>200000 cm^2/Vs),[8] thermal conductivity (~5000 $Wm^{-1}K^{-1}$) higher than that of carbon nanotubes (CNTs),[9] optical transparency (97.7 %)[10] and outstanding mechanical properties (Youngs modulus ~1.0 TPa).[11] Besides the study of fundamental properties of graphene, a large number of reports have focused on graphene based heterostuctures. Graphene is being used to make graphene-polymer composites resulting in improved

electrical, thermal, mechanical and other properties of the polymer;[12, 13] graphene-metal structures i.e., sheets decorated with metal nanoparticles have shown enhanced catalytic and sensing properties;[14-16] and graphene-organic heterostructures are being studied for optoelectronic applications.[17] All these studies indicate wide-ranging future applications involving graphene-hybrid structures. Thus, the field has various avenues to focus on, and hence a dramatic rise in the number of reports involving graphene has been observed.

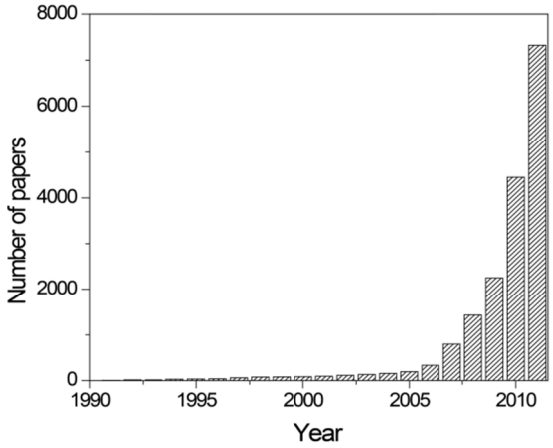

Figure 1.2 Number of publications containing the term 'graphene' per year according to the Web of Science.

According to the Web of Science, over 26000 reports have been published that include the term graphene since 2004, as shown in the *Figure 1.2*. It is not appropriate to address all this work here, instead the properties of graphene oxide and graphene hybrid structures will be highlighted.

1.1 Structure of graphene

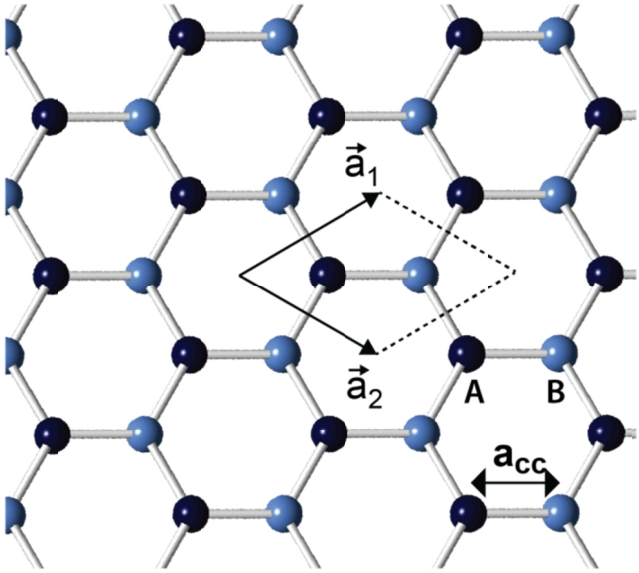

Figure 1.3 Crystal structure of graphene showing the unit cell with the lattice vectors $\boldsymbol{a_1}$ *and* $\boldsymbol{a_2}$ *and the nearest neighbour distance as* $\boldsymbol{a_{cc}}$*. A and B are the two in-equivalent carbon atoms.*

The crystal structure of graphene is no different from a layer of graphite (*Figure 1.3*). The crystal lattice of graphene (*Figure 1.3*) consists of two atoms, A and B, per unit cell and the coordinates of the lattice vectors are defined as $\vec{a}_1 = \sqrt{3}a_{cc}(\sqrt{3}/2, 1/2)$ and $\vec{a}_2 = \sqrt{3}a_{cc}\left(\sqrt{3}/2, -1/2\right)$ where, $a_{cc} =$ 1.42 Å is the distance between the nearest carbon atoms. When the single layers of graphene are stacked in AB Bernal stacking the result is multilayer graphene, and beyond 10 layers it is graphite.[4] In graphite with AB stacking, every other layer of graphene is shifted in the horizontal plane such that the A – carbon atom of the upper layer lies on top of the B – carbon atom of the lower layer.

The lateral dimensions of graphene can range between large sheets measuring hundreds of microns[4] to nano-ribbons that are a few nanometers wide.[18] The interlayer

spacing in graphite is 0.34 nm however the thickness of graphene can vary from ~0.4 – 1 nm depending on the substrate and the amount of adsorbed species.[19]

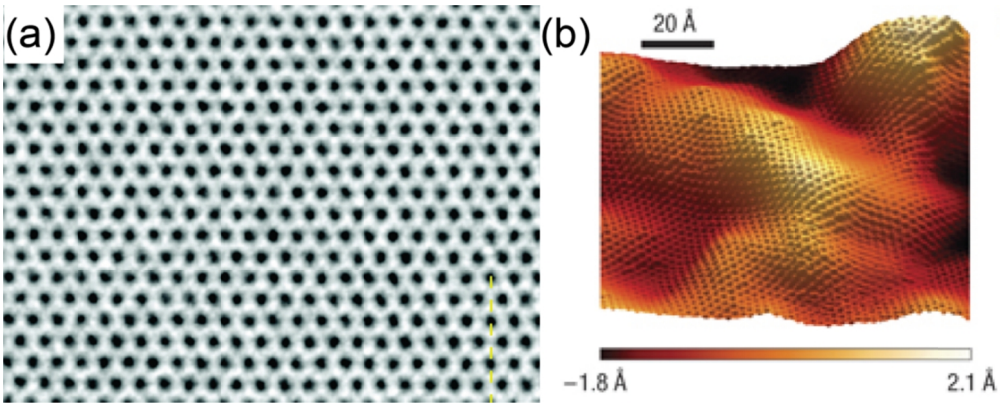

Figure 1.4 (a) Transmission electron microscopy image of a single layer graphene sheet; atoms appear white. (b) Scanning tunnelling microscopy image of a graphene sheet on Si/SiO_2. (a) and (b) reproduced from Meyer et al.[20] and Zhang et al.[21] respectively.

The atomic structure of free standing graphene can be seen in a high resolution transmission electron microscope (TEM) as shown in *Figure 1.4a* (reproduced from Meyer et al.[20]). The carbon atoms in graphene appear white in the image. TEM has been used as a powerful technique to study the lattice structure and defects in graphene at the atomic scale.[20, 22] The topography of a mechanically exfoliated graphene sheet, deposited on a Si/SiO_2 substrate, obtained using scanning tunnelling microscope (STM) is shown in *Figure 1.4b* (reproduced from Zhang et al.[21]). Topographical corrugations can be clearly seen. The microscopic corrugations or ripples have also been observed on suspended graphene in TEM and the thermodynamic stability of the 2D layers has been attributed to these ripples.[23] In addition, the surface topography has been found to depend on the substrate; when supported on mica, the topography has been reported to be atomically flat for graphene[24] as well as graphene oxide.[25]

Electronic structure

Since in a carbon atom there are 6 electrons, the ground state electronic configuration is – $1s^2, 2s^2, 2p^2$ i.e. the outermost 4 electrons are available for covalent bonding. In sp^2 hybridisation, the outermost 2s and 2p orbitals, with 2 electrons in each, combine to give 3 electrons in 3 sp^2 orbitals and 1 electron in the p_z orbital perpendicular to the plane of graphene. Each carbon atom shares 3 planar σ bonds with the 3 neighbouring carbon atoms using the sp^2 orbitals. This leaves the π electrons in the p_z orbital weakly bound to the nucleus, and hence delocalised. The σ bands have filled shells and they are not involved in the charge transport. The delocalized p_z electrons of the neighbouring carbon atoms interact laterally, leading to the formation of a half filled π band with the π (bonding) and π^* (antibonding) states.

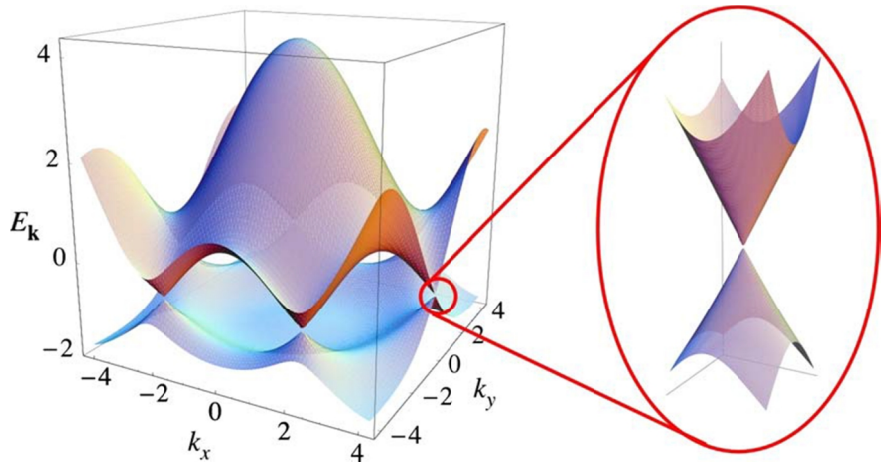

Figure 1.5 Electronic dispersion relation in a graphene lattice with the enlargement showing the band structure around a Dirac point. Reproduced from Castro Neto et al.[26]

The majority of the outstanding (opto)electronic properties of graphene are a consequence of the transport of the π electrons in the graphene lattice. The electronic structure of graphene is well-known as graphene was used to understand the electronic structure of graphite by Wallace[5] in 1947. The energy dispersion relation in graphene,

calculated using a tight binding model, is shown in *Figure 1.5* (reproduced from Castro Neto et al.[26]). The two states, also known as the valence (π) and conduction (π^*) bands, of the π band are symmetric and touch at the corners of the K points also known as the Dirac points. As a result graphene is a zero gap semiconductor or a semimetal. The bands appear exactly conical, showing a linear dispersion, around the Dirac points.

1.2 Fabrication of graphene

History

Graphene is a name originally given to a planar sheet of carbon atoms possessing graphitic structure.[27] The earliest evidence of exfoliation of graphite can be traced back to more than 170 years ago, when Schafhaeutl, reported exfoliation of graphite by treating graphite with nitric acid and sulphuric acid in 1840.[28] After more than a decade, in 1855, Brodie reported synthesis of graphite oxide by treating graphite with nitric acid and potassium chlorate.[29] Today, graphene oxide, a material precursor to chemically modified graphene (CMG), is most commonly prepared by the Hummers and Offeman method (1958)[30] and sometimes by the Staudenmaier method (1898)[29] used for oxidising graphite.

Growth of graphene on metal surfaces also has a surprisingly long history. Monolayer graphite like structures, formed as a result of segregation of carbon, on the surface of Pt can be traced back to 1968.[31, 32] Metals such as Ni, Pd, and Co also have been used for growth of graphene in the past.[33, 34]

Also, growth of graphene by sublimation of silicon carbide (SiC) has been known for a while. Low electron energy diffraction (LEED) patterns of monolayer graphite, prepared by sublimation of SiC at high temperature and under ultra-high vacuum (UHV), have been reported since 1975.[35]

Mechanical exfoliation of highly oriented pyrolytic graphite (HOPG) to thin islands have been reported by Ruoff and co-workers in 1999.[36] Finally, Geim and co-workers mechanically exfoliated graphite to achieve free standing graphene using a 'scotch tape' in 2004.[37]

Current methods of fabrication

Since the explosion of research in the field of graphene, versatile methods of fabrication have been developed; as a result, the term graphene is used to refer to a variety of planar hexagonal carbon materials with different compositions. At present, the most commonly used methods for synthesizing graphene are (1) micromechanical cleavage,[37] (2) sublimation of SiC (001),[38] (3) growth on metals and (4) exfoliation of graphite oxide. Although, every method has its own advantages and disadvantages the 'exfoliation of graphite oxide' method stands out as it provides a simple and inexpensive route to large scale production of solution processable graphene.

Micromechanical cleavage – this method involves peeling of HOPG layers using a 'scotch tape' and provides graphene sheets with the least number of defects.[4] The quality of graphene is excellent for fundamental studies; however, the method is too laborious and expensive for large scale production.

Sublimation of SiC – this process involves heating the SiC substrates in ultrahigh vacuum to 1000 – 1500 ℃; during annealing the Si sublimates and the carbon left behind has been shown to have graphitic structure.[39] This method facilitates large scale production of graphene directly onto semiconducting or insulating substrates and hence the devices are compatible with the existing micro-electronic technology. But this method is expensive because SiC is expensive and it requires high temperature annealing and UHV conditions.

Growth on metals – crystalline graphene has been grown on a number of metals, such as Ni, Pt, Pd, Co, Cu, Ir or Ru, by either precipitation of absorbed carbon or by physical or chemical vapour deposition of gaseous precursors like methane.[6, 40, 41] From these metals, Cu has been shown to be promising because large area and mostly single layer graphene sheets can be produced.[42, 43]

Exfoliation of graphite oxide – graphite is oxidised to graphite oxide via the Hummers method which involves treating graphite with concentrated sulphuric acid and potassium permanganate. A mild sonication of aqueous suspension of graphite oxide gives exfoliated sheets of graphene oxide (GO).[44] GO is a sheet of carbon atoms randomly decorated with oxygen containing functional groups such as epoxy, hydroxyl, carbonyl and carboxyl.[45] These groups make as produced GO insulating. GO can be reduced to make it conducting for device applications. Treatments with reducing agents such as hydrazine and/or low temperature annealing result in conducting sheets named as reduced GO (rGO).[44]

Reduction of GO – most commonly, GO is first deposited on a desired substrate by spin coating, or drop-casting, and then reduction is carried out. Different techniques for reducing GO include high temperature annealing in inert or reducing atmospheres,[46, 47] using arc discharge method,[48] microwave assisted reduction,[49] reduction using hydrazine and hydrazine plus annealing.[44, 50, 51] The conductivity of rGO reduced by hydrazine alone is rather low 10^{-2} – 10^{1} S/cm; with a combination of hydrazine and annealing, the conductivity has been increased to 10^{2} S/cm.[46] Hydrazine is highly toxic and flammable hence a number of reports have come up with alternative approaches, for example reduction by hydrohalic acid which results in conductivity ~300 S/cm.[52] The most conductive films of rGO have been reported by vacuum annealing at 1100 °C; the conductivity was 1800 S/cm.[53]

Although, several reducing methods have been developed, the conductivity in rGO sheets is still a few orders of magnitude lower than that of pristine graphene sheets, mainly because of the incomplete reduction and remaining defects. Yet, the inexpensive method of fabrication and ability to provide stable suspensions in a variety of organic solvents[54, 55] make this technique extremely useful for large scale production of graphene based materials.

Additionally, the functional groups make GO advantageous over pristine graphene as the optical and electrical properties of these sheets can be tuned by using chemical and heat treatments.[56] The ability of these sheets to form covalent as well as non-covalent (based on π-π interactions) bonds encourages the fabrication of a wide variety of hybrid structures such as transistors, sensors, optoelectronic devices etc.[57, 58]

1.3 Structure of graphene oxide

Understanding the structure of GO is crucial for the development for applications based on CMGs. As graphene oxide is obtained from exfoliation of graphite oxide its structure can be related to the structure of a layer of graphite oxide. Although the first evidence for the synthesis of graphite oxide in the literature is more than 170 years old[28] the exact structure is still unclear. From a number of X-ray and electron diffraction studies, it has been found out that the interlayer spacing varies with water content (ranging between 0.5 to 1.1 nm).[29, 59] However, the in-plane structure has been a matter of debate for a long time.[59-61]

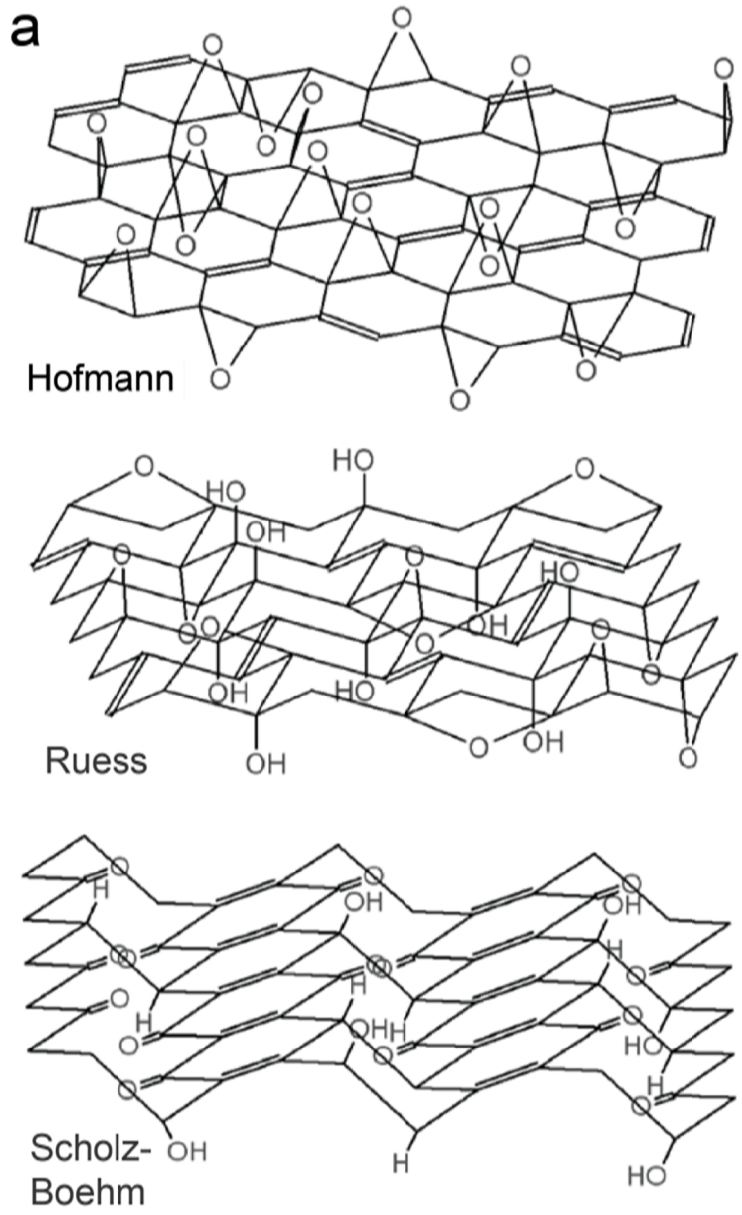

Figure 1.6a Structures of graphite oxide proposed by Hofmann, Ruess, and Scholz-Boehm. (Reproduced from Szabo et al.[61])

In the literature, a number of models for the structure of the basal plane of graphite oxide have been proposed. *Figure 1.6a and b* show the prominent models proposed: the Hofmann model (1939),[61] the Ruess model (1946),[61] the Scholz-Boehm model (1957),[61] the Nakajima-Matsuo model (1988)[60], the Lerf-Klinowski model (1998)[62] and the model proposed by Szabo et al. (2006).[61]

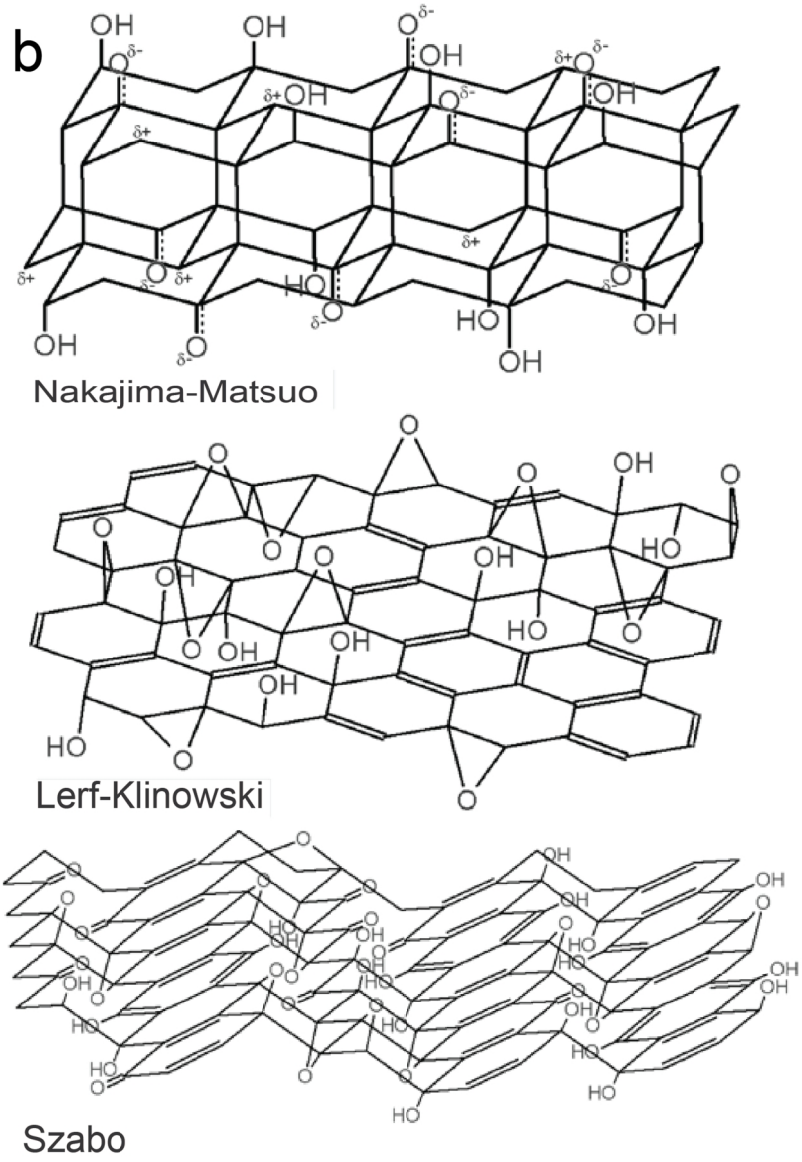

Figure 1.7b Structures of graphite oxide proposed by Nakajima-Matsuo, Lerf Klinowski and Szabo and coworkers. (Reproduced from Szabo et al.[61])

As shown in *Figure 1.6a*, the Hofmann model proposed that the epoxy groups were randomly attached to the hexagonal lattice structure of carbon atoms. The Ruess model suggested that hydroxyl and 1,3 epoxide groups are attached randomly to the wrinkled sheet of sp^3 carbon atoms. The Scholz-Boehm model also suggested wrinkled sheets of carbon atoms attached to random carbonyl and hydroxyl groups. As shown in *Figure 1.6b,* the Nakajima-Matsuo model is similar to Scholz-Boehm model but with electron

delocalisation on the epoxy groups. All these models relied on the findings of elemental analysis, chemical reactivity and X-ray diffraction studies.[63] Lerf and coworkers used solid state nuclear magnetic resonance and obtained a model similar to the Hofmann model but with random epoxy and hydroxyl groups. The most recent model proposed by Szabo et al., is a mixture of Scholz-Boehm and Ruess models, suggesting a sp^3 carbon backbone.

Previously, there have been a few reports on the electron diffraction studies of graphite oxide and the presence of hexagonal structure with lattice parameters matching those of graphite has been observed.[59, 64] The models showing amorphous structure of sp^3 carbon atoms (Ruess, Scholz-Boehm, Nakajima-Matsuo, and Szabo) would not produce electron diffractions with lattice parameters of graphite. Clearly, these models are rather incompatible and do not agree even on the basics of the structure such as the lattice parameters or type of bonding between the carbon atoms.

Subsequently, investigations on the structure of graphene oxide have suggested it to be mostly amorphous.[65, 66] In studies, using high resolution TEM, the structure of GO on average has shown disordered regions, and the regions containing sp^2 carbon atoms are only a few nanometers in dimensions.[67, 68] For example, *Figure 1.7* (reproduced from Erickson et al.[67]) shows atomic resolution TEM image of graphene oxide displaying nanoscopic graphitic regions in between amorphous regions.

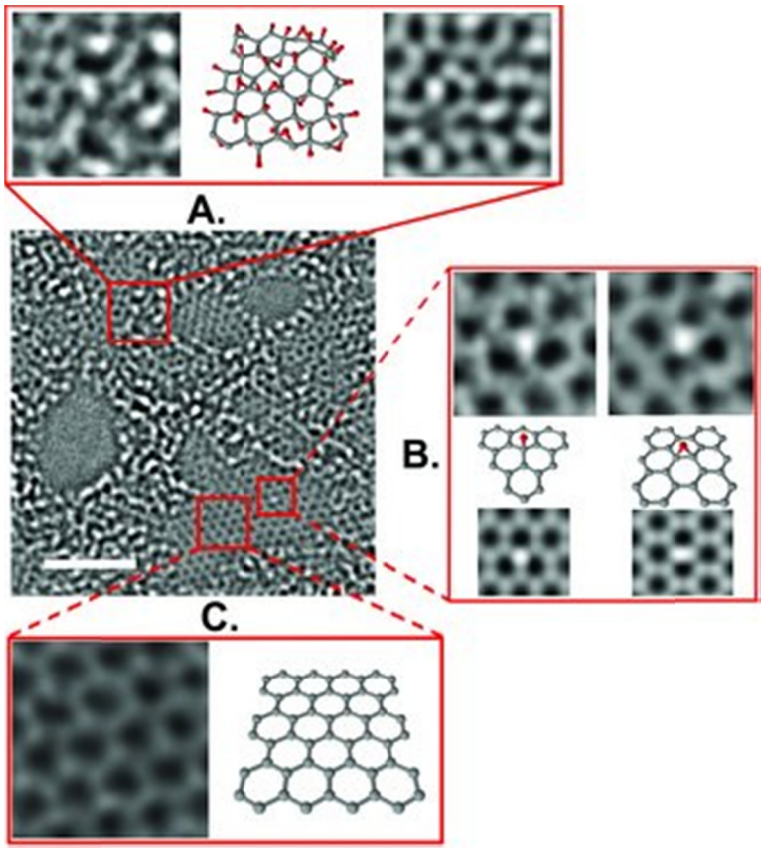

Figure 1.8 Atomic resolution TEM image of graphene oxide (scale bar – 2 nm). The enlargements at the top and bottom and to the right of the main image show the respective structures along with the proposed models showing (carbon - gray and oxygen – red in the models). The corresponding simulated TEM images are also shown in the top and right enlargements. Reproduced from Erickson et al.[67]

In another report, the evolution of the structure of GO was studied by progressively heating GO in UHV and performing in situ X-ray photoelectron spectroscopy (XPS) analysis. A model of GO proposed on the basis of this study is shown in *Figure 1.8* (reproduced from Mattevi et al.[56]). The GO structure was considered to be made of isolated graphitic domains surrounded by oxidised sp^3 carbon structures (*Figure 1.8a).* It was suggested that, as GO is progressively heated the graphitic clusters interact via formation of new sp^2 clusters and upon further reduction, percolation of sp^2 clusters occur creating conducting pathways.

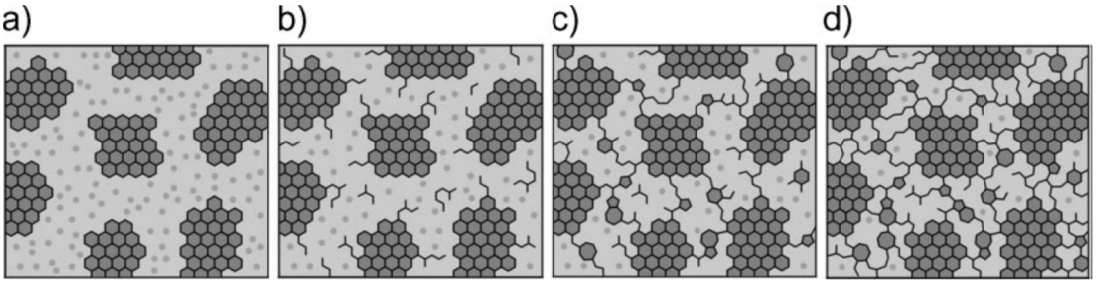

Figure 1.9 Proposed model of GO at different stages of reduction by heating at – (a) room temperature, (b) ~100 °C (c) ~220 °C and (d) ~500 °C. Reproduced from Mattevi et al.[56]

Besides the structure and bonding of carbon atoms in the basal plane, the composition and percentage of the functional groups is also vague. Studies have found that epoxy, hydroxyl and carbonyl are attached to the basal plane of the carbon skeleton while carboxyl groups are mainly on the edge sites.[62, 69] However, the exact positions and ratios in which these groups are present are not known. A number of theoretical investigations on the structure of graphene oxide have also been reported. Density functional theory (DFT) calculations[70] have found 1,2 ether to be energetically more stable than 1,3 ether. In the same study it was found that, in a 2 × 2 cell the epoxy and hydroxyl groups are stable when in close proximity. In another DFT study on a 2 × 2 cell,[71] a combination of 1 epoxy and 4 hydroxyl was found to be the most stable configuration. More recent theoretical studies have found localised ordering of the epoxy and hydroxyl groups.[72] Despite the number of reports that have been published, the structure of the basal plane of carbon atoms and the precise composition of the functional groups is still unresolved.

1.4 Hybrid graphene structures

For wider applications of graphene or CMGs, understanding their interaction with other materials is essential. Graphene and its derivatives have been integrated with a

number of materials for applications such as transparent electrodes,[44, 73] field effect transistors,[74, 75] catalysis,[76] sensors,[3, 57] etc. As much of the research is focussed on electronic and organic based optoelectronic applications, the investigation of interactions of metals and organic molecules with graphene is vital.

Metal-graphene structures

Metal morphology on graphene is affected by several factors, such as deposition method used, graphene substrate, and deposition conditions such as rate and temperature.[77, 78] Metals on graphene have been deposited by physical[79, 80] and chemical[81, 82] methods and the metal morphologies have been significantly different in the two cases.

GO based metal-graphene structures produced by chemical processing have been reported several times.[81, 83] In chemical processing the metal based precursors directly react with GO or rGO sheets, in suspension or on substrate, to give graphene-metal nanoparticle composites with homogenous distribution of a uniform sized and predefined shape of metal nanoparticles. In these cases the size, shape and distribution of the metal nanoparticles are determined by the chemical approach and not by the graphene-metal interactions. Additionally, these processes cause covalent modification of the graphene sheet, which affects the intrinsic structure of the graphene.[84]

On the other hand, metals deposited by evaporation have been studied on graphene grown on metal substrates.[78, 85] However, in these situations the interaction between graphene and the metal substrate dominates the electronic structure of graphene.[6] Hence the morphology of the metal deposited does not depend on the metal and graphene interactions alone.

Theoretically, metal-graphene interactions have been studied more extensively. For example, the sites acquired by the metal adatom on the graphene lattice; doping of

graphene by metal adsorption, type of bonding between metal atom and graphene, and hence the morphology of the metal film on graphene have been predicted.[86-88]

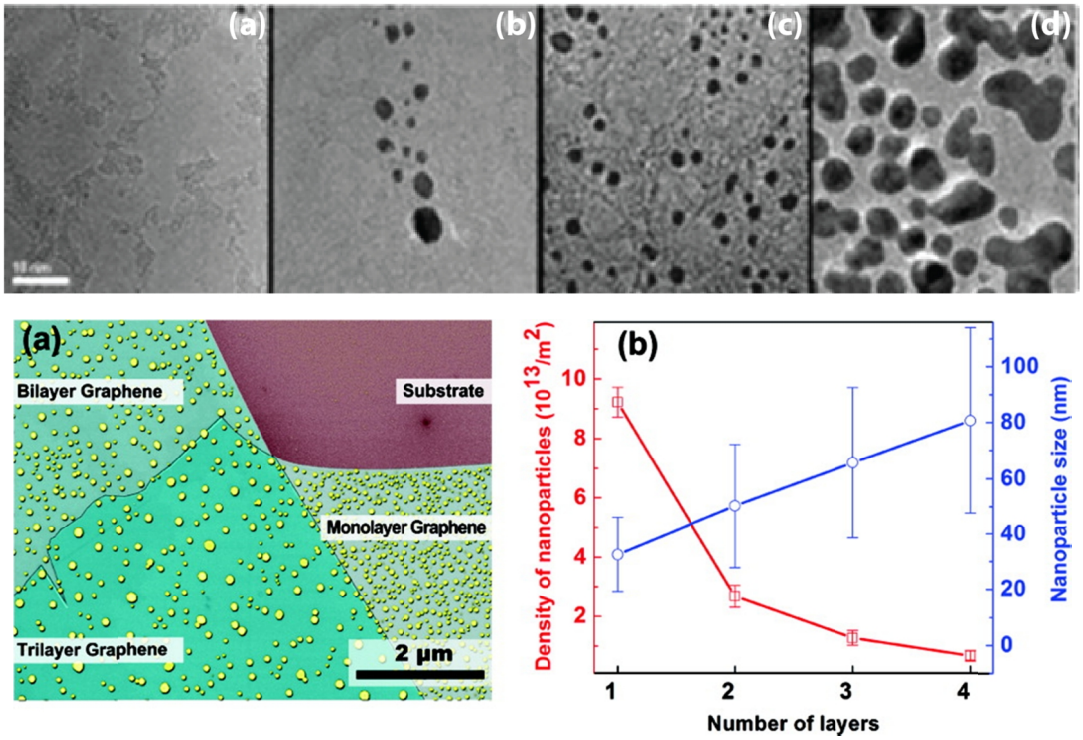

Figure 1.10 ***(Top)*** *TEM images of a single layer of graphene (grown on copper via CVD) evaporated with Au of thicknesses (a) < 0.1 nm with sparse coverage, (b) < 0.1 nm showing occasional clusters, (c) 0.12 nm, and (d) 2.12 nm. scale bar is 10 nm in all images (reproduced from Zan et al.[89]).* ***(Bottom)*** *(a) SEM image of layer dependent morphology of Au nanoparticles evaporated on mechanically exfoliated graphene on Si/SiO_2 substrate. (b) Number density and particle size varying as a function of number of graphene layers (reproduced from Zhou et al.[80]).*

Also, there have been a few reports on metals evaporated on graphene that was either suspended or supported on an insulating substrate (mostly Si/SiO_2).[79, 80, 90, 91] These studies have often concentrated on the interaction of gold evaporated on graphene and confusing results have been obtained. Zan et al. have reported that Au atoms do not stick to the single layer pristine graphene or hydrogenated graphene; instead the Au clusters are found near to the surface contaminations (*Figure 1.9 top,* reproduced from Zan et al.[89]). On

the other hand a number of reports have found layer dependent morphology of metals, including Au, evaporated on graphene[80, 90, 92] (*Figure 1.9 bottom,* reproduced from Zhou et al.[80]). The bottom of *Figure 1.9* clearly demonstrates the effects of number of layers on the morphology of Au-on-graphene. The layer dependence has been attributed to the electrostatic interactions between the graphene and metal.[90]

More recently, there has been an increase in the number of reports on the interaction between metal and graphene. Metal deposition via plasma sputtering has resulted in random scattering and electron localisation in graphene;[93] moreover, layer by layer removal of graphene layers by sputter coating with zinc followed by dissolution in acid has also been observed.[94] Metal-mediated hole formation in suspended graphene has been observed and is attributed to the lowering of the energy of vacancy formation in graphene in the presence metal atoms.[95]

Another important aspect of the metal-graphene interaction is the understanding of the type and level of doping in graphene due to the amount and type of the metal deposited. In a recent report, the effect of the size of Au clusters on the type of doping in graphene was demonstrated. It was found that the isolated Au nanoparticles result in n-type doping while thin films result in p-type doping in graphene. The difference in the doping properties were recognized as the difference in the interfacial interactions between the graphene and Au nanoparticles or film.[96]

All these results indicate that for metal deposition by evaporation the metal-graphene interactions play an important role in determining the final metal morphology on graphene. However, the experimental evidence of the major factors governing the growth and morphology of these metals on free standing graphene is still inadequate.

Organic-graphene structures

Currently, the market standard for transparent electrodes is indium tin oxide (ITO), and its use is faced with several issues. Besides being brittle, indium is inadequately transparent in the infra-red region, unstable towards acid and base conditions, and also expensive as the resources on the earth are depleting.[97] Graphene, with its excellent electrical properties, high stretchability, tunable work function and high transmittance, is a promising candidate for transparent conductors in optoelectronic devices.[97] A sizable class of optoelectronic devices, like organic light emitting diodes (OLEDs), liquid crystal displays (LCD), touch screens, organic field effect transistors (OFETs), involve organic materials.

To date, the most promising method to produce large area, highly conducting and transparent graphene films for photovoltaic cells is the CVD method.[42, 74] The high efficiency (power conversion efficiency = 1.71 %) in these devices has been credited to the non-covalent bonding of the graphene layer with the organic layer (pyrene buanoic acid succidymidyl ester) in the layered structure of the cell.[98] More recently, graphene based devices with power conversion efficiency value of 8.6 % were fabricated and the performance was attributed to the doping of the graphene sheets from the organic layer (bis(trifluoromethanesulfonyl)amide [$(CF_3SO_2)_2NH$]) in the device.[99]

Due to the simple solution processing, rGO films have been utilised as transparent electrodes.[44, 46] Fabrication of optoelectronic devices incorporating rGO sheets combined with organic semiconductors has been reported.[100] In the report on organic thin film transistors, the rGO electrodes have shown lower contact resistance than Au electrodes due to the π-π interaction between the semiconducting layer (organic molecules) and the rGO.[100] The major issue in using rGO as a replacement for ITO, is the high sheet resistance in rGO. Although, GO possesses high optical transparency, it is insulating. The reduction process makes GO conducting but does not fully recover the graphene lattice. As a result,

rGO possesses remnant oxygen groups and defects and hence low conductivity values. GO films reduced by vacuum annealing at 1100 ℃ have shown a lowest sheet resistance of ~800 Ω/sq. with transmittance of 82 % at 550 nm.[53] The sheet resistance of ITO is ~10 – 30 Ω/sq. with transparency greater > 90 % at 550 nm.[101] As already discussed in Section 1.2, the research is on-going and these issues have been the focus of several reports.

Moreover, the as-produced GO has also been used in polymer solar cells as a high performance hole transport layer.[102] Thus, CMG sheets with different functionality could result in fully solution processed and flexible devices.

The important factor to be considered in fabrication of these devices is the interaction of organic molecules with graphene sheets. The understanding of these interfaces and ability to manipulate them is crucial to enhance the absorption of light and to control the charge transport properties. One of the results in this thesis focuses on the interaction of a molecular semiconductor, fluorinated copper phthalocyanine (F_{16}CuPc) with CMG.

1.5 Outline of thesis

The focus of the work in this thesis is the fabrication of graphene via exfoliation of graphite oxide, understanding its structure and studying the interactions of the CMG with other materials, like metals and organic molecules with relevance for applications. CMG was prepared by the Hummers method and conventional TEM imaging and diffraction were the most frequently used characterisation techniques.

The details of CMG synthesis and typical characterisations are given in Chapter 2. One of the major questions in the study of the field of CMG is the structure of GO. The investigations on the lattice structure and chemical composition of GO are discussed in Chapter 3. The highly transparent nature of GO under TEM investigation, as discussed in

Chapter 3, is utilised to perform the study on the interactions and growth of different metals and the molecular semiconductor, $F_{16}CuPc$, on CMG sheets. The results are presented in Chapter 4. The insight on the metal-graphene interactions is utilised to fabricate dense nanoparticle arrays on rGO for hydrogen gas sensing. In Chapter 5 the fabrication and working of Pd coated rGO devices as hydrogen gas sensors is demonstrated. Finally in Chapter 6, conclusions are drawn from the whole body of work and suggestions made for future avenues of investigation.

Chapter 2. **Methods and Materials**

2.1 Experimental techniques – TEM

In this work, the standard techniques that were used are atomic force microscopy (AFM), scanning electron microscopy (SEM), x-ray photoelectron spectroscopy (XPS), Raman spectroscopy, and thermogravimetric analysis (TGA); however, the most frequently used technique was TEM. The predominantly used methods were low magnification imaging and selected area electron diffraction (SAED). A JEOL 2000FX fitted with Gatan SC–1000 Orius charge coupled device (CCD) camera at Warwick was used for all low magnification imaging and diffraction work here.

The basic principles involved in the formation of a magnified image are the same in a light microscope (LM) and an electron microscope (EM). The major differences between the EM and LM are the radiations used and the way in which they are bent.

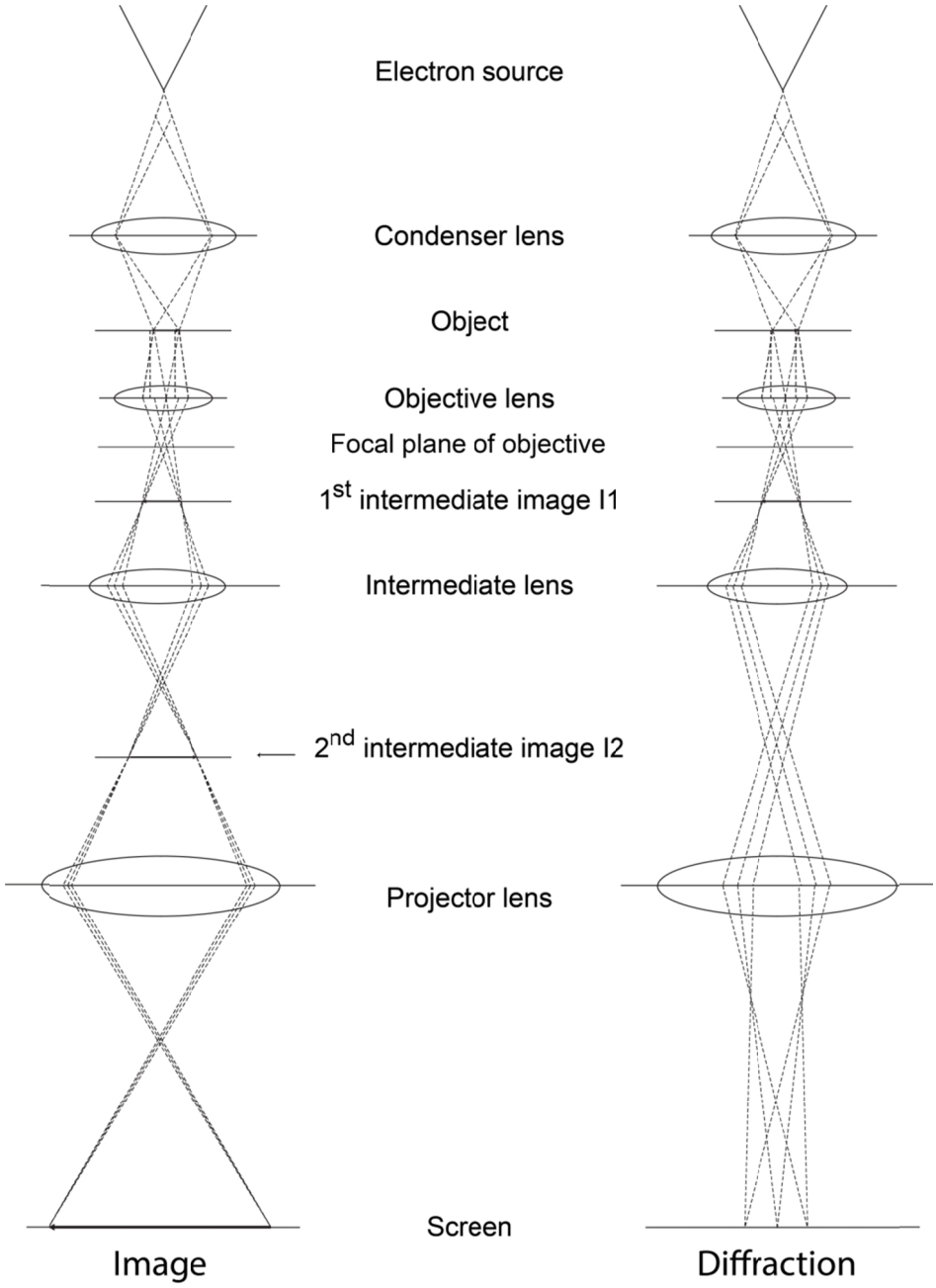

Figure 2.1 Schematic of ray paths of electrons in the TEM under (left) imaging and (right) diffraction conditions. Adapted from ref.[103]

Figure 2.1 shows a simple sketch of the path of electron beams in a TEM under (left) imaging and (right) diffraction conditions. In an electron microscope, a beam of electrons accelerated at hundreds of kV, is focused into a small, thin, coherent beam by the use of the condenser lens. When a TEM is operated at 200 kV a beam of electrons of

wavelength 0.025 Å is formed. This beam is restricted by the condenser aperture, which excludes the electrons scattered at high angle. The beam then strikes the specimen and parts of it are transmitted depending upon the thickness and electron transparency of the specimen. As the electrons pass through the sample, they are scattered by the electrostatic potential set up by the constituent elements in the specimen. After passing through the specimen they pass through the electromagnetic objective lens which focuses all the electrons scattered from one point of the specimen into one point in the image plane (1^{st} intermediate image I1). Optional objective apertures can be used to enhance the contrast by blocking out the high-angle diffracted electrons. The final image magnification is controlled by the intermediate and projector lenses. The image strikes the phosphor screen and light is generated, allowing the user to see the image.

TEM images can be acquired in bright field or dark field imaging mode. A bright field image is acquired by inserting an aperture in the objective lens which does not allow the Bragg reflections to pass through to the final image and therefore the direct beam and any low angle inelastic beams form the final image. Images can also be formed by excluding the direct beam i.e. using one of the diffracted beams and the image so formed is called the dark field image. The contrast in a TEM image is mainly of two types: mass-thickness contrast and diffraction contrast. The areas in the specimen of higher thickness or with atoms of greater atomic number (Z) scatter electrons more strongly and therefore appear darker in bright field images and brighter in dark field images. Diffraction-contrast arises when the electrons are Bragg scattered. The contrast is as a result of differences in the intensities of the electrons scattered into Bragg reflections and is called diffraction contrast.

As shown in *Figure 2.1* (right) the focal plane of the objective lens is the place where the electrons scattered in the same direction by the sample are collected into a

single point and a diffraction pattern is formed. To view the diffraction pattern the intermediate lens system can be set to focus on the focal plane of the objective; the pattern is then magnified by the projector lens and observed on the screen. A pattern from a selected area of the specimen can be obtained by inserting an aperture situated in the plane of the first intermediate image. This gives selected area electron diffraction (SAED) patterns.

2.2 Synthesis and characterisation

CMG provides a route to produce large scale, solution processable graphene and opens possibilities for modification and further functionalization of graphene.[84, 104] GO is a member of the CMG family and is the first step towards fabrication of a wide variety of CMGs.

2.2.1 Synthesis of graphene oxide

Graphene oxide can be synthesized by using the Brodie, Staudenmeir, or Hummers method.[50] In this work a modified Hummers method as reported by Eda et al., [44] is used.

Modified Hummers method: 5 g of graphite powder was mixed with a solution of 4.5 g of KNO_3 and 169 ml of concentrated H_2SO_4 and placed in an ice bath. This mixture was continuously stirred and 22.5 g of $KMnO_4$ was slowly added over a period of 1 hour. The mixture was left to stir for another 2 hours in the ice bath and then removed from the ice bath and left to stir continuously for 5 days. This resulted in a black viscous liquid. To this, 500 ml aqueous solution of 5 wt% H_2SO_4 was added over 1 hour while stirring continuously. After stirring for a further 2 hours, 30 wt.% aqueous solution of 15 g of H_2O_2 was added to the mixture and left to stir for a further 2 hours. The oxidised mixture turned dark brown in colour. This mixture was washed by adding 500 ml aqueous solution of 3 wt.

% H_2SO_4, and 0.5 wt. % H_2O_2, leaving to precipitate for 2 days and then discarding the clear supernatant. The procedure of washing was repeated 10 times. The resulting dark brown slurry was dispersed in de-ionised (DI) water by mild sonication to give an aqueous colloidal suspension of GO.

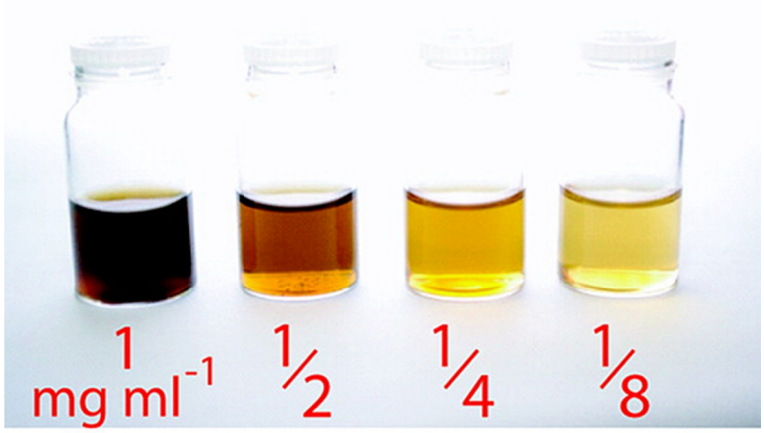

Figure 2.2 Aqueous dispersions of GO of concentrations 1, 1/2, 1/4, and 1/8, mg ml^{-1} from left to right.

Vacuum filtration: Vacuum filtration was an important step to get rid of all the water soluble contaminants in the GO suspension obtained using the modified Hummers method. This step was carried out for all the GO based samples produced in this study.

A mixed cellulose membrane (Millipore), having an average pore size of 0.22 µm, was used to vacuum filter the GO dispersion. A thin, uniform film of GO was formed on the filtration membrane whilst the water soluble contaminants were washed through. The filtration membranes were dried in a vacuum desiccator, and then the GO films were peeled off resulting in a free-standing graphene oxide paper which is convenient for storage. When required, the graphene oxide paper can be re-dispersed at known concentrations in water by mild sonication or stirring *Figure 2.2* shows GO dispersions of concentrations 1, 0.5, 0.25 and 0.13 mg ml^{-1}.

Deposition on a substrate: GO can be deposited from an aqueous suspension directly onto substrates such as silicon oxide (300 nm SiO_2 on degenerately doped Si) for further study. SiO_2 is hydrophobic and has been previously treated with 3-amino-propyltriethoxysilane prior to deposition of GO.[68] Here, O_2-plasma treatment (Quorum Technologies Plasma Etcher-Asher-Cleaner) was used (100 W for 2 minutes), to make the SiO_2 hydrophilic. After this, two different approaches were used.

Spin Coating: graphene oxide suspension was placed on the substrate and the substrate was rotated at 3000 rpm for 45 s. The acceleration and deceleration times were 0.1 s. This technique is efficient as it results in a controllable and uniform distribution of GO sheets. As discussed in Section 2.2.2, a near monolayer coverage was obtained with GO concentration of 1 mg ml^{-1}. For higher concentrations of GO (5 – 10 mg ml^{-1}) longer spin coating time (60 s) was required for complete drying of the film.

TEM Grids: samples for TEM were prepared by drop casting GO dispersion on lacey carbon grids. Prior to drop casting the lacey carbon grids were air-plasma cleaned for 20 s to make them hydrophilic. Some samples were also prepared by drop casting GO dispersion on lacey carbon grids that were sputter coated with Au at rate of 5 nm/min. These can be used to calibrate GO diffraction patterns (DP) against gold DP as will be shown in Chapter 3.

Reduction of GO: in this study two techniques were used for reducing GO.

Reduction in suspension: 112 μl of ammonia solution (35 wt. % Fisher Scientific) and 17.6 μl of hydrazine monohydrate solution (62 wt.%, Fisher Scientific) were added to 10 ml of 1 mg ml^{-1} GO suspension and the mixture was left to stir for 1 h at 90 °C.[51] The mixture slowly turned black over the hour. These rGO dispersions were used to coat TEM grids by drop casting.

Figure 2.3 Aqueous dispersions of 0.5 mg ml^{-1} GO (left) and rGO (right).

Reduction on the substrate: as reported by Becerill et al. a two-step reduction was followed.[46] GO spin coated on Si/SiO_2 substrate was placed in a small petri dish which was then placed in a larger petri dish containing 1 ml of hydrazine anhydrous (98 %, Sigma Aldrich). The whole system was sealed using a glass cover and parafilm and placed in an oil bath at 40 ℃ for 18 h. The samples were then washed with DI water, dried, and, then heated at 300 ℃ in air for 1 h.

2.2.2 Characterisation of chemically modified graphene

AFM topography was obtained using an Asylum Research MFP3D AFM in tapping mode. Figure 2.4a shows the AFM height image of a GO film spin coated on Si/SiO2 substrate from a suspension of concentration 1 mg ml-1. The image clearly shows a layer of fully exfoliated GO sheets. This layer shows uniform thickness and almost full coverage on the substrate. The lateral dimensions of these sheets range from 100 nm to 2 µm. Occasionally, a second layer is also visible on top of the first GO layer.

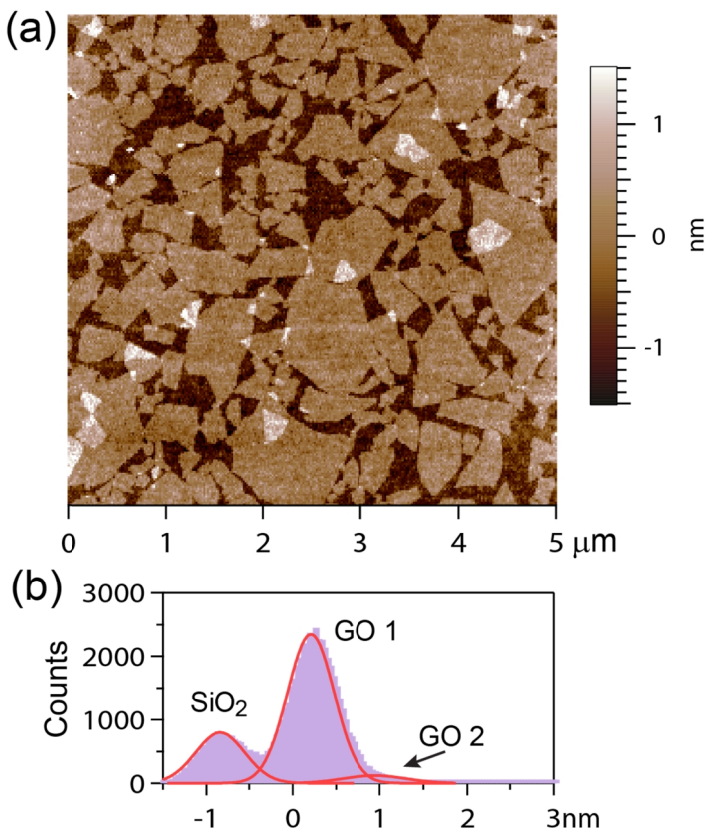

Figure 2.4 (a) AFM topography of GO (1 mg ml^{-1}) spin coated on Si/SiO$_2$ (b) histogram plot of the topography showing peaks from the substrate, a single layer of GO (GO 1) and 2 layers of GO (GO 2). Gaussian fits to the individual peaks are shown in red. These can be used to give an accurate indication of layer thickness.

Figure 2.4b shows a histogram plot of the height data. The peaks in the histogram plot from the substrate (SiO_2), first layer of GO (GO 1), and the second layer of GO (GO 2) are fitted using Gaussian fits, shown in red. The difference in the positions of SiO_2 and GO 1 peaks gives a thickness of 1.0 nm for the GO layer on the substrate. In the same way, the thickness of second layer is measured to be 0.7 nm. From several such images the thickness of a GO layer was found to vary between 0.7 – 1.2 nm. The interlayer spacing in graphite is 0.34 nm, however, GO layers are expected to be thicker due to the presence of oxygen groups and adsorbed water molecules[105] and the thickness also depends on the substrate and adsorbed species.[19] Isolated flakes of rGO made by reducing GO on the substrate were also measured to be between 0.7 and 1.2 nm thick.

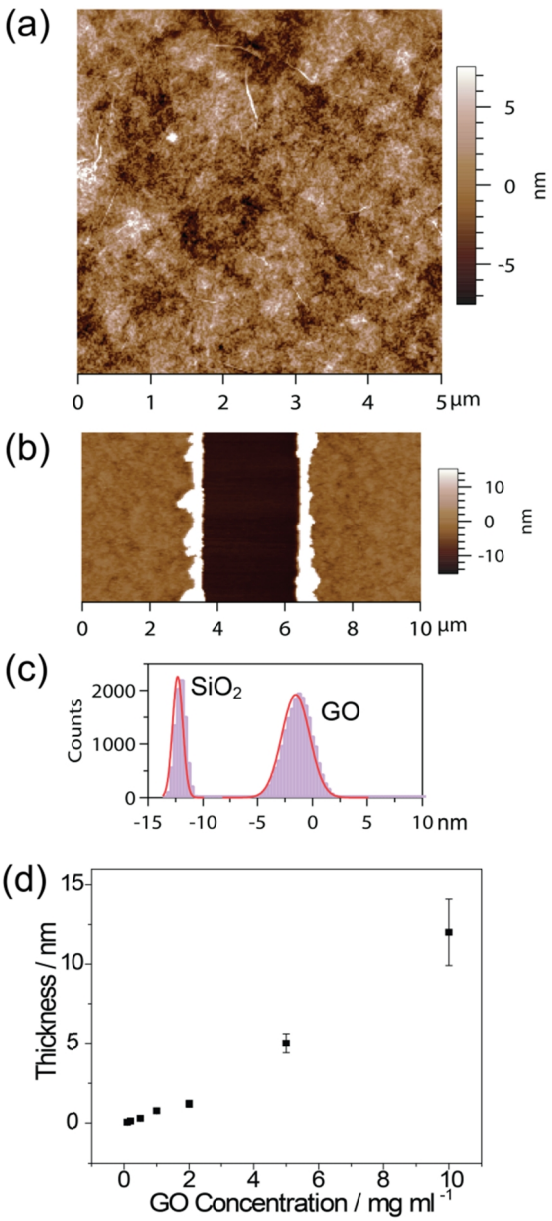

Figure 2.5 (a) AFM topography of GO (10 mg ml^{-1}) spin coated on Si/SiO_2 substrate (b) AFM topography of GO layer showing a 2.5 µm wide trench created by scanning the region in contact mode. (c) Histogram plot of the topography in (b) showing peaks from substrate and GO film. (d) Plot of thicknesses of GO films as a function of its concentration in water.

Various concentrations of homogeneous suspension of GO in water were prepared by sonicating GO paper in DI water. *Figure 2.5a* shows AFM topography (tapping mode) of a continuous layer of GO film obtained from a suspension of 10 mg ml^{-1} GO. In order to measure the thickness of a continuous film, a trench was made in the film by scanning the sample in contact mode. The topography of the region was then scanned in tapping mode; *Figure 2.5b* shows AFM topography of one such region. From the histogram plot (*Figure 2.5c*) of the region the thickness of the film is measured to be 10.7 nm.

The concentration of GO suspensions was varied from 0.2 to 10 mg ml^{-1} and the thicknesses of spin coated GO films were measured using AFM. Note, for concentrations below 1 mg ml^{-1} the effective thickness values were averaged over the substrate area. The thickness of the GO films as a function of GO concentration in water is plotted in *Figure 2.5d*. The plot shows an approximately linear relationship between the measured thickness and the GO concentration in water. A similar relationship between GO thickness and concentration was obtained by Becerill et al.[46]

Thicker films were also made by multiple coating; double spin coating of 5 and 10 mg ml^{-1} GO suspensions resulted in films with thicknesses 15 $\pm$ 2 and 32 $\pm$ 2 nm respectively.

Figure 2.6 shows a comparative study of GO and rGO (formed by exposure to hydrazine and then thermal annealing in air at 300 ℃) using TGA, x-ray diffraction (XRD) analysis and Raman spectroscopy. TGA measurements were done on a Metler-Toledo TGA/DSC1 with a heating rate of 10 °C min^{-1} in air flow, XRD on a Panalytical X'Pert Pro MRD (copper target, λ = 0.154 nm), and Raman spectroscopy on a Renishaw 1000 spectrometer with 633 nm laser excitation at low power of < 0.5 mW to avoid sample damage.

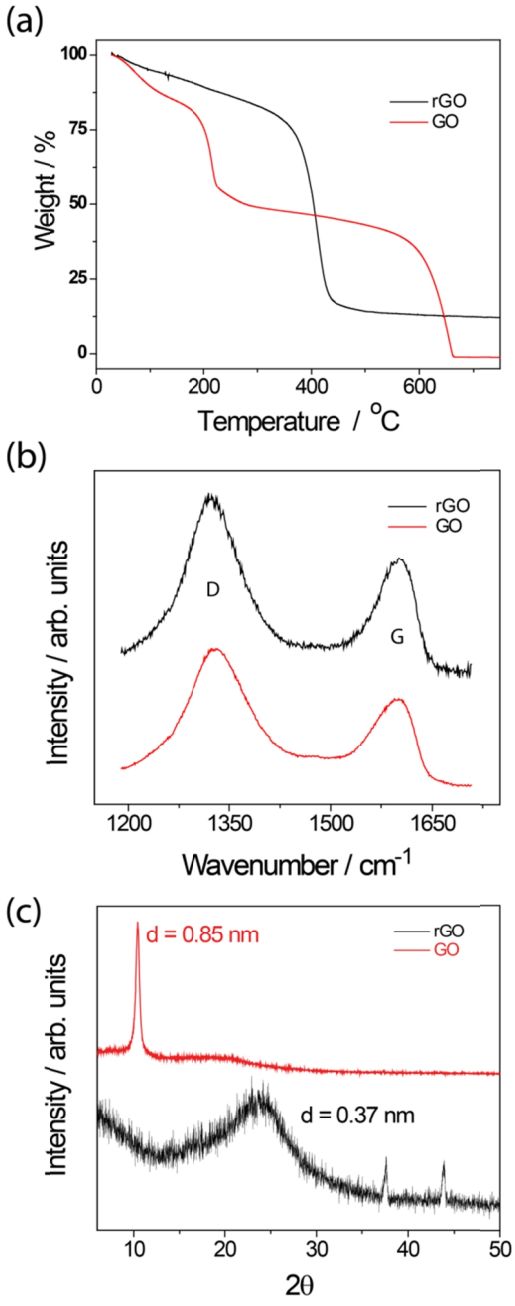

Figure 2.6 (a) Thermogravimetric analysis rGO and GO papers, (b) Raman Spectra of GO and rGO deposits on the Si/SiO_2 substrates and (c) XRD of rGO and GO papers. TGA courtesy of Dave Hammond and XRD courtesy of Luke Rochford, Department of Chemistry and John Halpin, Department of Physics, University of Warwick. Raman spectra courtesy of Dr. Ian Kinloch from The University of Manchester.

Suspensions of GO and rGO were vacuum filtered and the resulting materials were analysed using TGA in air. In the TGA plot, *Figure 2.6a*, the mass losses in GO and rGO below 200 ℃ are assigned to adsorbed water vapour.[66, 106] GO shows a significant mass loss at around 200 ℃ which has previously been assigned to the loss of functional groups[66] and the carbon structure burns completely at around 600 ℃. TGA of rGO shows a small mass loss around 200 ℃ and a major mass loss at around 400 ℃ which could be due to burning

of the rGO structure as the reduction processes introduce irreversible defects in the lattice. After this the rGO is thermally stable beyond 700 ℃.

Figure 2.6b shows the Raman spectra of monolayer GO and rGO on the substrate in the region 1100 – 1800 cm^{-1}. The spectra are similar; for both GO and rGO the G peak at ~1600 cm^{-1}) indicates presence of graphite like structure while the D peak (GO – 1328 cm^{-1} and rGO – 1322 cm^{-1}) arises as a result of disorder in the structure. Here, the ratio of the D to G peaks for GO is 2.0 and that for rGO is 1.9, consistent with previous reports.[68]

For XRD the GO paper was used as prepared. The suspension of rGO was filtered through an alumina membrane (pore size 0.02 μm, Whatman anodisc filter membrane) and the rGO paper on the filter membrane was heated in air at 300 ℃ for 1 hr. *Figure 2.6c* shows the XRD plot obtained for GO and rGO papers. GO shows a sharp peak at $2\theta = 10.4°$, a layer spacing of 0.85 nm, indicating presence of functional groups and intercalated water molecules. rGO shows a peak around 23 – 24° corresponding to a significantly decreased layer spacing in the range 0.37 – 0.39 nm. This peak is weak and broad as the rGO sheets do not form a well dispersed suspension and hence result in less ordering in the rGO paper. The layer spacing values in GO and rGO are consistent with previous reports.[66, 106] The weak peaks in rGO at around 35° and 45° are from the alumina filter membrane.

Figure 2.7 shows XPS spectra of GO and rGO films deposited on Au coated silicon substrates. X-ray photoelectron spectroscopy (XPS) experiments were performed on a Scienta ESCA300 spectrometer at the National Centre for Spectroscopy and Surface Analysis, Daresbury Laboratory, UK. Samples for XPS were prepared by spin coating a 1 mg ml^{-1} aqueous suspension of GO on Au coated silicon substrates. rGO samples were made by following the reduction on the substrate method (Section 2.2.1).

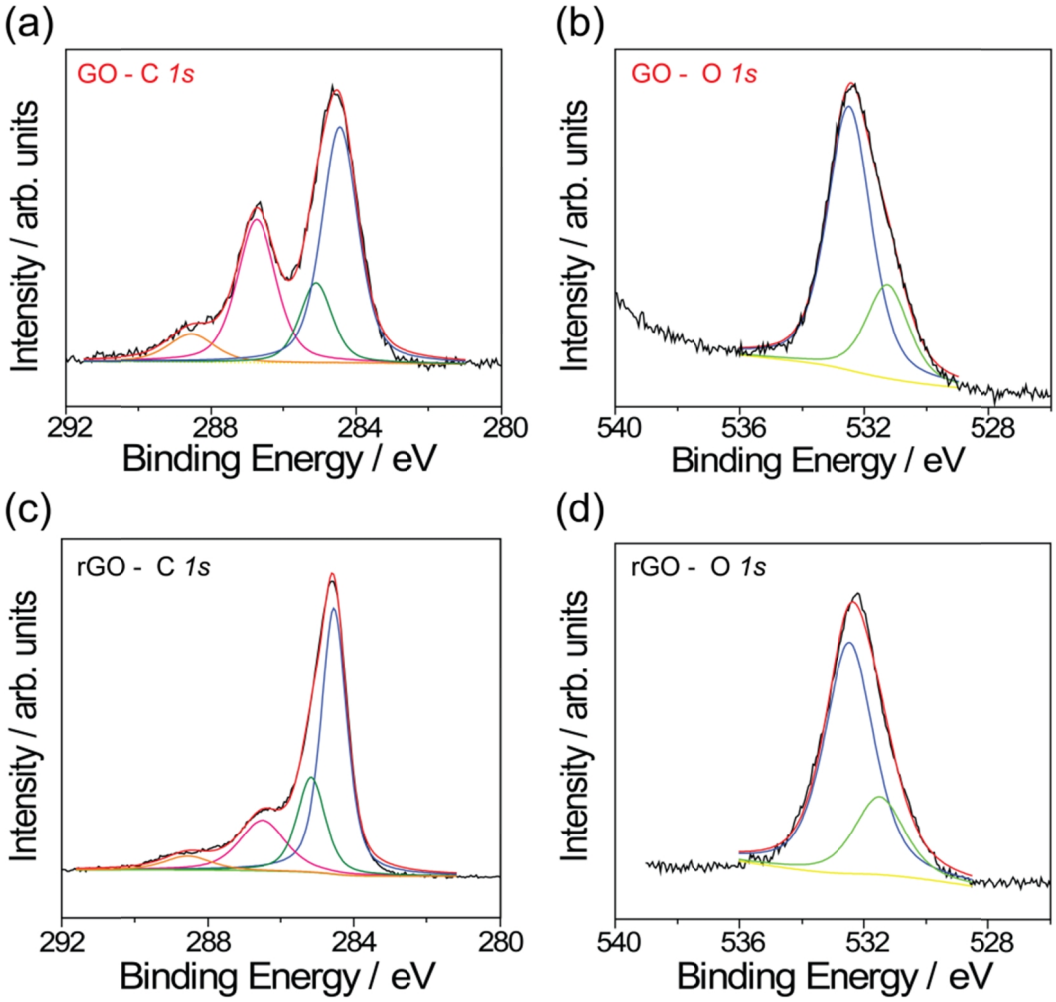

Figure 2.7 X-ray photo-electron spectra of GO and rGO; (a) C 1s and (b) O 1s core level spectra from GO; (C) C 1s and (b) O 1s core level spectra from rGO. Substrates for XPS were prepared by Dr. Neil Wilson, University of Warwick.

Figures 2.7a and b are the C *1s* and O *1s* core level spectra of GO and *Figures 2.7 c* and *d* show the C *1s* and O *1s* core level spectra of rGO. Au *4f* spectra (not shown here) from the substrate provided in situ calibration of the C *1s* and O *1s* peak positions. All of the spectra (black curves) were deconvoluted by fitting Voigt peaks, shown in colour. The background shown in yellow was fit using a Shirley + linear background. The sum of the peaks is shown in red curves. In both C *1s* spectra, the peaks are assigned to C-C sp^2 at 284.6 ± 0.2 eV[55] (blue), C-C sp^3 at 285.2 ± 0.2 eV (green), epoxy and hydroxyl groups at

286.6 ± 0.2 eV (pink) and carboxyl group at 288.6 ± 0.2 eV (orange).[45, 55, 107, 108] In both O *1s* spectra, the peaks are assigned to epoxy and hydroxyl at 532.5 ± 0.2 eV (blue), carboxyl group at 531.3 ± 0.2 eV (green).[45]

From the C *1s* peaks it is evident that the amount of functional groups is significantly reduced in the rGO sample. The C:O ratios from the carbon and oxygen peaks are 2.2:1 for GO and 5.1:1 for rGO. The C:O ratio from the C *1s* peak alone is 1.7:1 for GO and 5.4:1 for rGO.

However, the C:O ratio obtained from the C *1s* peaks alone does not reflect the true stoichiometry of GO because: (1) the adsorbed amorphous carbon and carbons attached to hydrogen are accounted for in the carbon sp^3 peak and (2) in the epoxy-hydroxyl peak, for every carbon atom, an oxygen atom is assumed although an epoxy group has 2 carbon atoms attached to 1 oxygen atom (distinguishing between hydroxyl and epoxy groups in XPS is difficult). Further, comparison of the C *1s* to the O *1s* peak does not give the true picture either, since O *1s* core level accounts for oxygen atoms attached to the graphene lattice as well as those from adsorbed H_2O and CO_2 molecules. However, XPS gives useful insight into the stoichiometry before and after reduction.

Electrical characterisation

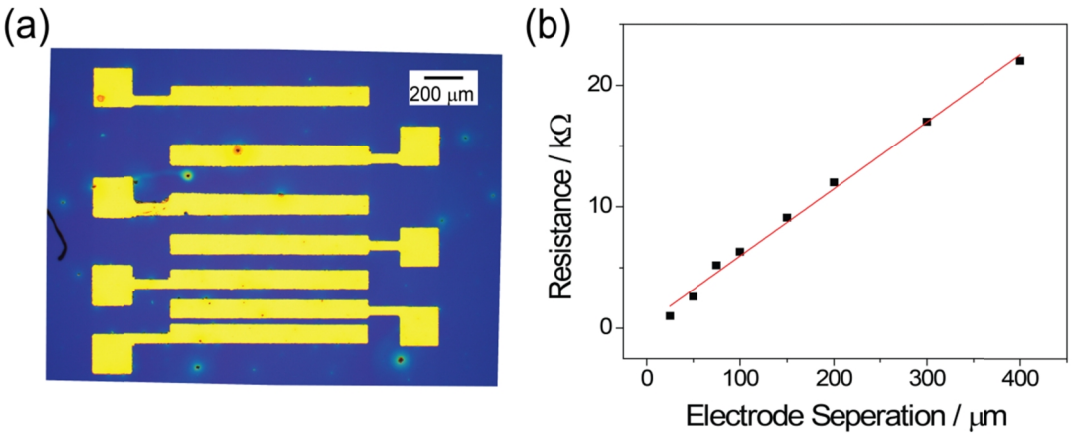

Figure 2.8 (a) Optical image of a rGO device showing part of the electrode configuration. (b) device resistance as a function of the electrode separation.

GO suspension (5 mg ml^{-1}) was spin coated on the Si/SiO_2 substrates with predefined Cr/Au contacts. The thickness of the GO film was 5.0 ± 0.6 nm. After reduction on the surface the thickness decreased to 2.9 ± 0.5 nm implying a decreased interlayer spacing of ~ 0.4 nm, consistent with the XRD results.

Figure 2.8a is an optical microscope image of a typical rGO device (thickness ~3 nm) showing the electrode configuration for electrical characterisations (electrical characterisation substrates were prepared by Dr. Neil Wilson, University of Warwick). The plot in *Figure 2.8b* shows a linear relationship between device resistance and electrode separation, implying that the resistances are intrinsic to rGO rather than just contact resistances. From measurements over a number of similarly prepared devices, the conductivity was found to be between 20 and 90 S/cm and the sheet resistance ranging between 40 and 200 kΩ/sq. consistent with other reports in the literature.[47] Although similarly prepared, the rGO devices always showed a wide range of electrical conductivity values,[46] presumably due to variations in amount of remnant oxygen groups, defects and sizes of rGO platelets amongst the devices.

These devices were also measured before reduction but the resistance in the GO films were too high for our measurement capabilities.

2.2.3 Growing graphene by chemical vapour deposition

Graphene was grown on Cu by chemical vapour deposition (CVD). Growth of graphene on copper is a surface catalysed process and hence often self-limiting to a single layer.[42] In a typical procedure, a copper foil (99.5 % purity, 25 µm thick, Alfa Aesar product number 13382) was cut into 2×4 cm strips and loaded into a quartz tube placed inside a tube furnace. The quartz tube was then evacuated to a base pressure of 10^{-3} mbar. Flow of hydrogen gas (purity 99.999%) was established at 2 standard cubic centimetre per minute

(sccm) (controlled by mass flow controllers) at all times during the growth process. The copper foil was heated to 1000 ℃ at a rate 15 ℃/min and annealed for 20 minutes before flowing methane (purity 99.95 %) at 35 sccm for 10 min. The furnace was then cooled down to 100 ℃ and the Cu strip was removed from the furnace.

Transfer of graphene to alternate substrate: graphene grows on both sides of the copper. Layers of methylmethacryalate (MMA) and polymethylmethacyalate (PMMA) were spin coated onto one side of the graphene on Cu and the whole stack was placed on top of a solution of Cu etchant ($FeCl_3$, Alfa Aesar 44583) with PMMA side up. The copper substrate was dissolved in the Cu etchant within 2-3 hours and the stack of graphene/MMA/PMMA was scooped out on a glass slide, rinsed in DI water, and finally scooped out from the DI water on top of the desired substrate (Si/SiO_2 or TEM lacey grids). The substrate supported film was left to dry overnight in a vacuum desiccator. The MMA/PMMA layer was then dissolved by washing the film-on-substrate in acetone and then isopropanol (IPA). The graphene-on-substrate was finally dried under a nitrogen stream.

Generally these graphene layers showed cracks after transfer hence for electrical characterisation a second layer of graphene was deposited on top of the first graphene layer following the above mentioned procedure again.

2.2.4 Characterisation of CVD graphene

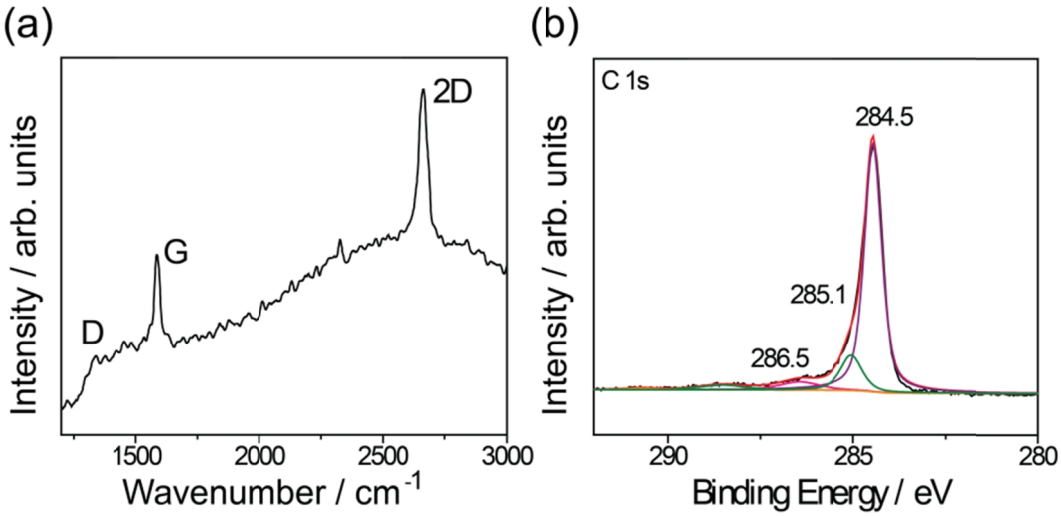

Figure 2.9 (a) Raman spectrum of graphene on Cu and (b) XPS showing C 1s core level in graphene. Raman spectrum courtesy of Dr. Ian Kinloch from The University of Manchester.

Figure 2.9a shows a Raman spectrum of graphene as grown on Cu. The spectrum was obtained on a Renishaw 1000 spectrometer with 633 nm laser excitation. The G and 2D peaks were fitted with single Lorentzian peak fits at around 1587 cm^{-1} and 2665 cm^{-1} respectively; the width of the 2D peak was 39 cm^{-1}. A weak D peak is seen at around 1330 cm^{-1}. The ratio of the intensities of 2D and G peak is 3.4. The width of the 2D, and the ratio of intensities of G and 2D are consistent with monolayer graphene.[42]

XPS experiments were performed on a Scienta ESCA300 spectrometer at the National Centre for Spectroscopy and Surface analysis, Daresbury Laboratory, UK. *Figure 2.9b* is a C *1s* core level XPS spectrum showing the C–C sp^2 peak at around 284.5 eV, C-C sp^3 and C–H at around 285.1 eV and a weak peak at around 286.5 eV indicating adsorbates containing oxygen.

For electrical characterisation of the CVD grown graphene, double layers of graphene were transferred on to the substrates with predefined contacts as for the rGO.

The films yielded conductivity of 6000 ± 900 S/cm and a sheet resistance of 2.2 ± 0.4 kΩ which is higher than expected for graphene and could be attributed to cracks in the film.[109]

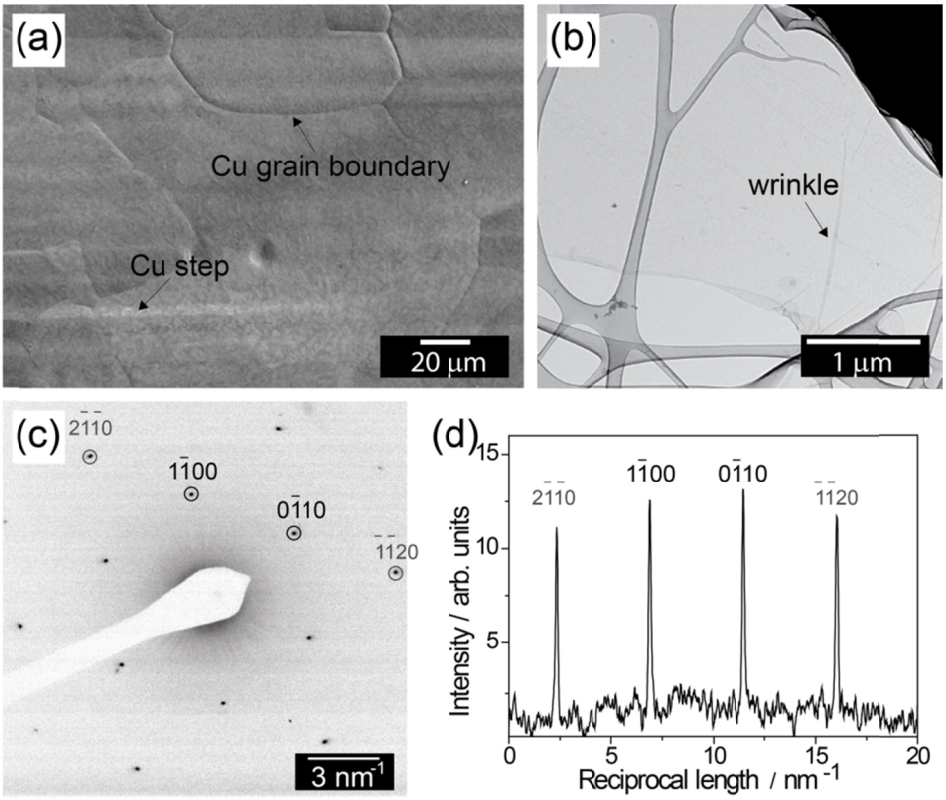

Figure 2.10 (a) SEM image of graphene on Cu. (b) Bright field TEM image of graphene on a lacey grid. (c) Inverted SAED pattern from the region of graphene shown in (b). (d) Intensity distribution across the spots indexed in (c).

Graphene, as grown on copper, is shown in the SEM image in *Figure 2.10a.* Graphene shows full coverage and Cu steps and grain boundaries are visible in the image. *Figure 2.10b* is a TEM image of a graphene sheet supported on a lacey grid. The top right corner is part of the copper TEM grid. The graphene sheet appears nearly transparent and is easily identified by the presence of wrinkles in the sheet. SAED pattern from the central region of the sheet is shown in *Figure 2.10c* (contrast inverted for clarity). The pattern shows a hexagonal set of spots, marked with Miller – Bravais indices. The pattern was calibrated using Au (111) ring patterns (not shown here) and lattice spacings were

measured. The lattice spacing d_{10} (corresponding to $1\bar{1}00$ spots) was measured to be 0.2128 $\pm$ 0.0010 nm. The intensity plot across the marked spots in the pattern is shown in *Figure 2.10d*. The ratio of the intensities of $1\bar{1}00$ to $2\bar{1}\bar{1}0$ type of spots was ~1.1 consistent with single sheet of graphene as in reports[25] and explained in Chapter 3.

2.3 Summary

Homogenous and stable suspensions of GO obtained by a modified Hummers method were used throughout this work. AFM showed fully exfoliated sheets of GO and the thickness of single GO sheets was found to range between 0.7 and 1.2 nm. The interlayer spacing in a GO paper was 0.85 nm, measured using XRD. The XPS measurements showed the presence of functional groups, such as hydroxyl, epoxy, carbonyl and carboxyl; the carbon to oxygen ratio was roughly 2:1 in these samples. As a result the GO sheets were found to be insulating. Raman measurements showed the presence of D and G peaks indicative of the presence of disorder and graphite like structure in GO. Thus the typical characterisations of GO and rGO samples gave results consistent with the reports in literature.[63, 68]

Reduction of a GO paper resulted in a decreased interlayer spacing of ~0.4 nm. Raman spectra showed typical D and G peaks. XPS measurements showed a considerable increase in the C:O ratio of rGO films, ~5:1. As a result the conductivity in these sheets was found to increase, between 20 – 90 S/cm consistent with previous reports.[44, 46]

Also, graphene sheets on Cu were prepared by CVD and typical characterisations were performed. The Raman, XPS and TEM measurements showed the presence of graphitic structure. The conductivity of these sheets was found to be 6000 $\pm$ 900 S/cm.

The samples prepared and characterised in the way mentioned in this chapter formed the basis of all the studies reported in this thesis.

Chapter 3. **Structure of CMG**

GO, a type of chemically modified graphene (CMG), is usually derived from exfoliation of graphite oxide. Even though, graphite oxide was synthesized more than 150 years ago[110] its precise structure and composition are still unclear. Graphite oxide had shown a strong evidence of crystalline structure,[59] but until recently, GO was thought to be predominantly amorphous or semi-amorphous with sp^3 hybridized carbon atoms containing hydroxyl and epoxy groups.[65, 66] The accepted properties of GO included its hydrophilic and insulating nature and a C:O ratio of roughly 2:1. On average, the structure of GO was considered to be comprised of a carbon backbone randomly decorated with oxygen containing functional groups such as hydroxyl (C–OH), epoxy (C–O–C), carbonyl (O=C-H) and carboxyl group (–COOH).[45, 105] However, there was no agreement on the structure of GO such as the local arrangement of the functional groups or the structure of the carbon backbone.[63, 68]

The study of the structure of GO is important for understanding its properties and for applications. In this study the structure of GO was analysed to understand the local arrangement of the carbon atoms, detect the presence of any ordering and get insight into the average chemical and physical structure. This study of the structure of GO is divided into two parts 1) TEM study of the structure of graphene oxide and reduced graphene oxide (rGO) and 2) study of the effect of base washing of the as-produced graphene oxide. Our TEM study showed that the as-produced GO possesses ordered graphene like regions over length scales > 10 nm indicating that the oxygen groups form scattered regions of disorder without affecting the average crystal lattice of the GO. The structure of GO was also compared to that of rGO and was found to be similar to rGO. Further insight into the structure of aGO was obtained by treating GO with NaOH; and it was found that the as produced GO is composed of functionalized graphene sheets decorated by strongly bound oxidative debris (OD).

3.1 Structural analysis of CMG in TEM

TEM investigations of graphene have shown that the crystal lattice and carbon to carbon bond length in graphene is identical to that of the basal plane of graphite.[23, 111] Here, TEM was used to analyse the structure of GO and rGO; it was found that GO and rGO not only preserve the hexagonal lattice structure of the parent graphite but also the carbon to carbon bond length.

3.1.1 Insight into the structure of CMG from TEM investigations

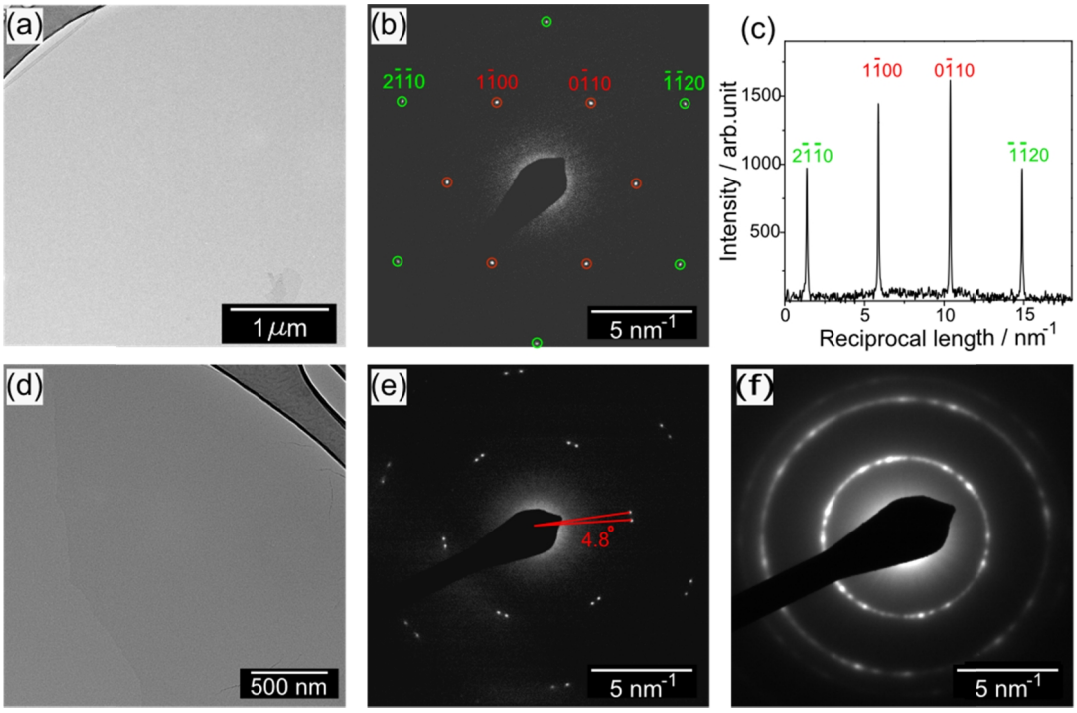

Figure 3.1 (a) TEM image of a single GO sheet on lacey carbon grid. (b) SAED from the centre of the region in (a). (c) Intensity profile across the diffraction spots labelled in (b). (d) TEM image of double layer GO on lacey grid. (e) SAED pattern from the centre of double sheet region in (d). (f) SAED pattern from a thin GO film.

For the study of GO by TEM, a dilute suspension of GO was drop cast onto a lacey carbon grid and dried for 30 minutes in air. The bright field TEM image in *Figure 3.1a* shows GO as a nearly transparent background and the lacey carbon support as a dark feature in the top left corner; around the support a small wrinkle in the GO can be seen. Using an aperture of size 0.6 µm, a selected area electron diffraction (SAED) pattern was obtained from this region of the GO sheet, *Figure 3.1b*. The pattern clearly displays sharp spots arranged in a hexagonal configuration. The spots are indexed according to Miller-Bravais (hkil) indexing used for hexagonal structures.[112] The intensity profile in *Figure 3.1c* across the indexed spots in (b) clearly shows that the $1\,\bar{1}00$ – type reflections marked in

red are more intense than the $2\bar{1}\bar{1}0$ – type reflections (in green). For the hexagonal pattern in *Figure 3.1c* the ratio of intensity of $1\bar{1}00$ to $2\bar{1}\bar{1}0$ type reflections was obtained to be 1.4 ± 0.1. From 10 diffraction patterns containing a single set of hexagonal spots the ratio was found to be 1.5 ± 0.2.

The SAED pattern revealed that GO not only exhibits a crystalline structure but also possesses hexagonal symmetry. The presence of sharp spots indicates short range order in GO, over length scales at least of the order of the coherence length of the electron beam (a few nm under the conditions used here) as discussed later in this section. The single hexagonal pattern without splitting of any of the spots indicates the occurrence of a long range orientational order over at least the size of the selected area aperture which was 0.6 μm. Additionally, no spots other than those corresponding to a hexagonal structure are visible, suggesting that oxygen groups in GO do not form any superlattice structure. Although the as-prepared GO showed a significant oxygen content with C:O ratio of approximately 2:1 (see Chapter 2), the functional groups do not significantly deform the average underlying hexagonal structure inherent from graphite. A hexagonal crystal structure has been observed for graphite oxide[59] hence the hexagonal spot pattern here alone does not prove the presence of graphene oxide rather than graphite oxide. In the A–B stacked graphitic structures it has been found that the diffraction intensity of $2\bar{1}\bar{1}0$ – type reflections is higher than that of $1\bar{1}00$ – type reflections because of interference between the electrons from A – type and B – type layers;[64] while for a single sheet of graphene the intensity of $1\bar{1}00$ – type reflections is higher.[113] The implications of the intensity ratios in A–B stacked graphite, along with further analysis of the GO diffraction pattern, is presented later in this section. The result that the GO here contains single sheets is also consistent with the thickness of GO sheets measured by AFM and the XRD interlayer spacings, (Chapter 2).

Figure 3.1d shows a sheet of GO (right) on top of another sheet (left) with the lacey support visible in the top right corner. The existence of the double layer of GO is identified by the difference in contrast between the two layers in the bright field TEM image. The SAED pattern (*Figure 3.1e*) obtained from the double layer of GO shows two sets of hexagonal patterns superimposed upon each other and the angle of misalignment of the patterns gives the angle of orientation between the double layers, here 4.8°. In *Figure 3.1f* the SAED pattern is obtained from a thin film of GO produced by vacuum filtration (0.22 μm pore size Nitrocellulose filter membrane, Millipore) of a GO suspension. The pattern shows concentric rings with the inner ring corresponding to $1\,\bar{1}00$ reflections more intense than the outer ring corresponding to $2\bar{1}\bar{1}0$ reflections.

Single sheet regions can show splitting of spots due to wrinkles; but multisheet regions always showed multiple sets of spots, with inner spots brighter than the outer ones, suggesting complete exfoliation of the layers. Study of SAED patterns from several multi-sheet regions did not indicate any preferential angle of orientation between the sheets. The SAED from GO thin films displayed circular rings instead of a hexagonal set of spots, as the hexagonal set of spots from each GO layer have merged to form rings with the inner ring more intense than the outer. This implies that each sheet of GO in the film is acting as a single crystal and there exists no preferential angle of orientation between the overlapping sheets. This also explains some of the confusion over whether GO is amorphous. The structure within a single sheet is crystalline, but the random stacking between the layers results in a ring pattern for thin films (characteristic of polycrystalline/amorphous materials)

Electron diffraction pattern analysis

The electron diffraction pattern indicates that GO exhibits a hexagonal crystal lattice. Further information about the crystal structure is revealed from the width and the intensity of the spots.

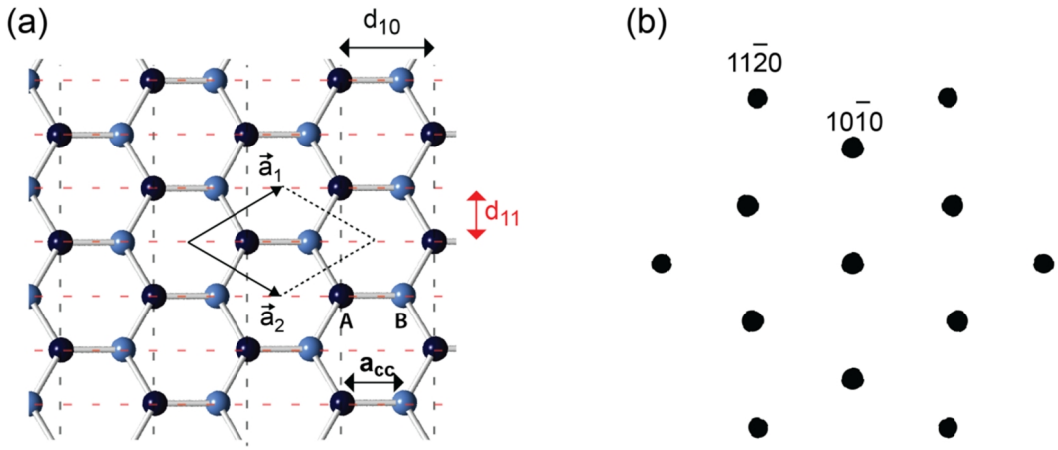

Figure 3.2 (a) Schematic of the structure of a graphene sheet with inequivalent carbon atoms shown in blue and black and the lattice planes corresponding to 10 and 11 lattice points are shown in black and red dashed lines. (b) Schematic of reciprocal lattice from a single sheet graphene.

In *Figure 3.2a*, the single layer graphene has 2 carbon atoms, 'A' (black) and 'B' (blue) per unit cell (a unit cell is shown in black). In the chosen lattice orientation, in *Figure 3.2a,* the lattice vectors of the graphene unit cell are defined as $\vec{a}_1 = \sqrt{3}a_{cc}(\sqrt{3}/2 , 1/2)$ and $\vec{a}_2 = \sqrt{3}a_{cc}\left(\sqrt{3}/2 , -1/2\right)$ where, $a_{cc} =$ 0.142 nm is the distance between nearest neighbour carbon atoms. The intensity of the beam diffracted by a graphene sheet at zero temperature is given by

$$I_{hk}^{0} = F_{hk} \times F_{hk} \qquad (3.1)$$

where, $$F_{hk} = f(\theta)\sum_{n} \exp(2\pi i(\boldsymbol{k}_d - \boldsymbol{k}_i)\boldsymbol{r}_n) \quad (3.2)$$

F_{hk} is the structure factor, $f(\theta)$ is the atomic scattering amplitude, $\boldsymbol{k}_d$ and $\boldsymbol{k}_i$ are the diffracted and incident beam wavevectors and $\boldsymbol{r}_n$ are the atom positions in the unit cell. To calculate the intensity values, I_{hk}, the structure factor is calculated using the scattering amplitude value for carbon atoms from Doyle and Turner[114] for the electron beam at 200 kV. Using the carbon atom positions $\boldsymbol{r}_n$ in the unit cell of AB stacked graphite and the number of layers 1,2,3,4… the intensity ratio I_{10}^0/I_{11}^0 at zero temperature is calculated to be 1.1, 0.28, 0.37, 0.28… respectively. The factor of 4 difference between the ratios of intensity for single and bilayer graphene makes this a useful signature of monolayer graphene.

The intensity ratio I_{10}/I_{11} for GO obtained from *Figure 3.1c* is significantly higher than the predicted values for a single layer of graphene at zero temperature. This inconsistency is accounted for by the Debye-Waller factor that describes the influence of lattice vibrations on the Bragg peak intensities. Since in TEM the interaction time of an electron in the electron beam with the graphene sheet is far shorter than the thermal oscillation periods (frozen phonon approximation), thermal oscillations and disorder induced atomic displacements are treated equally in the Debye-Waller analysis. The Debye-Waller factor modifies the structure factor by a term exponentially dependent upon the mean square displacement of atoms from their equilibrium positions.[115] Considering the Debye-Waller factor, the intensity of a diffracted beam at finite temperatures is given by

$$I_{10} = I_{10}^0 \exp(-16\pi^2 u^2 (\sin\theta / \lambda)^2) \quad (3.3)$$

where u is the root mean square displacement of the atom perpendicular to the Bragg plane and θ is the Bragg angle. Since

$$\left(\frac{2\sin\theta}{\lambda}\right)^2 = \frac{1}{d^2}$$

the intensity ratio can be written as

$$\frac{I_{10}}{I_{11}} = \frac{I_{10}^0}{I_{11}^0}\exp[4\pi^2 u^2(\frac{1}{d_{11}^2} - \frac{1}{d_{10}^2})] \qquad (3.4)$$

From the intensity ratio obtained in *Figure 3.1c* and using Equation (3.4), the mean square displacement (MSD) of the carbon atoms is 139 $\pm$ 5 pm^2 and hence the mean displacement from the equilibrium position is calculated to be 12 $\pm$ 2 pm which is just under 10% of the carbon-carbon bond length. The value of MSD found here is considerably higher than that found for mechanically exfoliated graphene (53 $\pm$ 3 pm^2) at a finite temperature[116] and that calculated for graphene at zero temperature (16 pm^2).[117] The substantial difference between the MSDs of graphene and GO clearly reveals that the lattice distortion here is also due to the functionalisation of the sheets and not just thermal oscillattions.

Another crucial piece of information about the crystal structure which that can be obtained from the diffraction patterns is a lower bound on the size of the crystalline regions. The full width at half maxima (FWHM) of the intensity distribution in the reciprocal space gives the size of the crystal plate.[103] However, the true size of the crystal is larger than the measured value as the diffraction amplitude is affected by factors such as inelastic scattering processes, instrumental errors, and Debye-Waller factor arising from the thermal oscillations; leading to a reduced amplitude and greater FWHM. Hence the measurement of crystallite size is limited to the spatial coherence length of the diffracted beam.

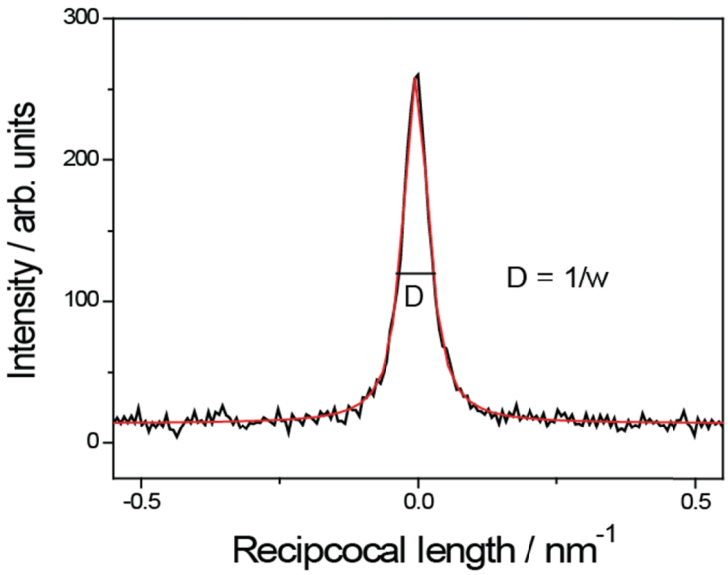

Figure 3.3 Intensity distribution in a diffraction peak with a Voigt fit shown in red. The FWHM of the peak, D, is inversely related to the length of the crystal plate.

Figure 3.3 shows the intensity distribution of a 10 peak and the inverse of the FWHM for this peak gives the coherence length, w = 18 nm. From 5 different sets of diffraction patterns of the same sample, the coherence length of the beam was measured to be 14 $\pm$ 2 nm. Thus the size of the graphene like crystalline region is at least 14 $\pm$ 2 nm for the GO synthesized by the standard modified Hummers method.[44] However, the observed width is almost certainly defined by the coherence of the electron beam rather than the size of the graphene like order.

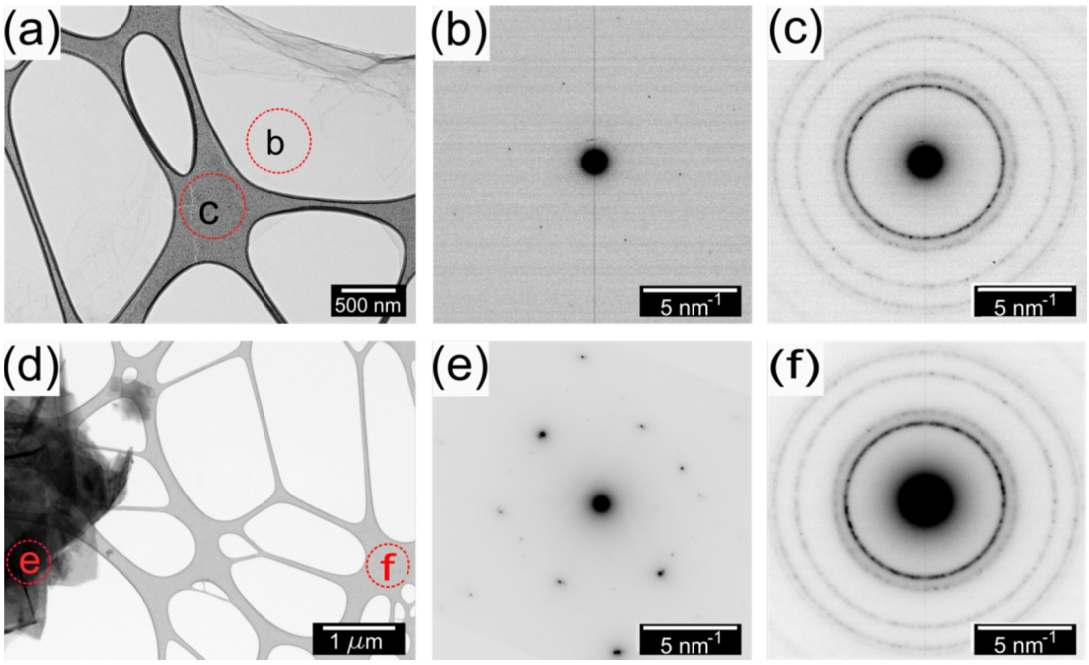

Figure 3.4 (a) TEM image of GO supported on a gold coated lacey carbon grid; (b & c) inverted SAED patterns from the regions marked as b and c respectively. (d) TEM image of a few layer graphite (FLG) film on the gold coated lacey carbon grid; (e & f) inverted SAED patterns from the regions marked as e and f respectively.

Electron diffraction patterns can be used to extract information about the lattice spacing and consequently the atom to atom bond lengths in the material. However, the measurements even from a calibrated microscope may not be reliable as a number of errors could be introduced because of variation in the sample height in the objective lens as well as projector lens distortions and astigmatism. Here, these distortions were minimised to a precision better than 0.5% by calibration in situ using Au coated lacey carbon grids. The SAED patterns were processed to minimise the astigmatism by fitting a circle to the Au 111 ring and stretching the pattern so that the ring is perfectly circular. *Figure 3.4a* shows the GO sheets as a nearly transparent background deposited on the Au coated lacey grid (visible as the dark feature in the image). The areas shown in red circles and marked with b and c correspond to the regions from where the SAED patterns in

Figure 3.4b and c were taken. The SAED pattern in *Figure 3.4b* shows the characteristic hexagonal set of spots and (c) shows the concentric circular pattern corresponding to the polycrystalline Au nanoparticles. The red arrow is pointing toward the Au 111 reflections.

A few layer graphite (FLG) suspension was also prepared by sonicating 2 mg of graphite flakes in 20 ml of 1-methyl-2-pyrrolidinone (NMP) and sonicating for 30 minutes before centrifuging at 500 rpm for 90 min to remove microscopic aggregates.[118] The suspension was drop-cast on a TEM lacey grid coated with Au. The lattice spacings were calibrated using the Au 111 reflections. *Figure 3.4d* shows the TEM image of FLG on a Au coated lacey grid and the SAED patterns of FLG and Au are shown in *Figure 3.4e and f.*

The Au 111 reflections corresponding to the lattice spacing of 0.235 nm were used to calibrate the GO diffraction pattern. From 10 different SAED patterns the lattice spacing corresponding to $1\,\bar{1}00$ reflections was found to be 0.2131 $\pm$ 0.0010 nm. This corresponds to an average in plane carbon – carbon bond length of 0.1421 $\pm$ 0.0007 nm. Using the same procedure the lattice spacing for FLG was measured to be 0.2133 $\pm$ 0.0010 nm. Hence, within the experimental error the lattice spacing of GO is identical to that of graphite and the average underlying structure in GO is planar with sp^2 hybridised carbon atoms similar to that of graphene.

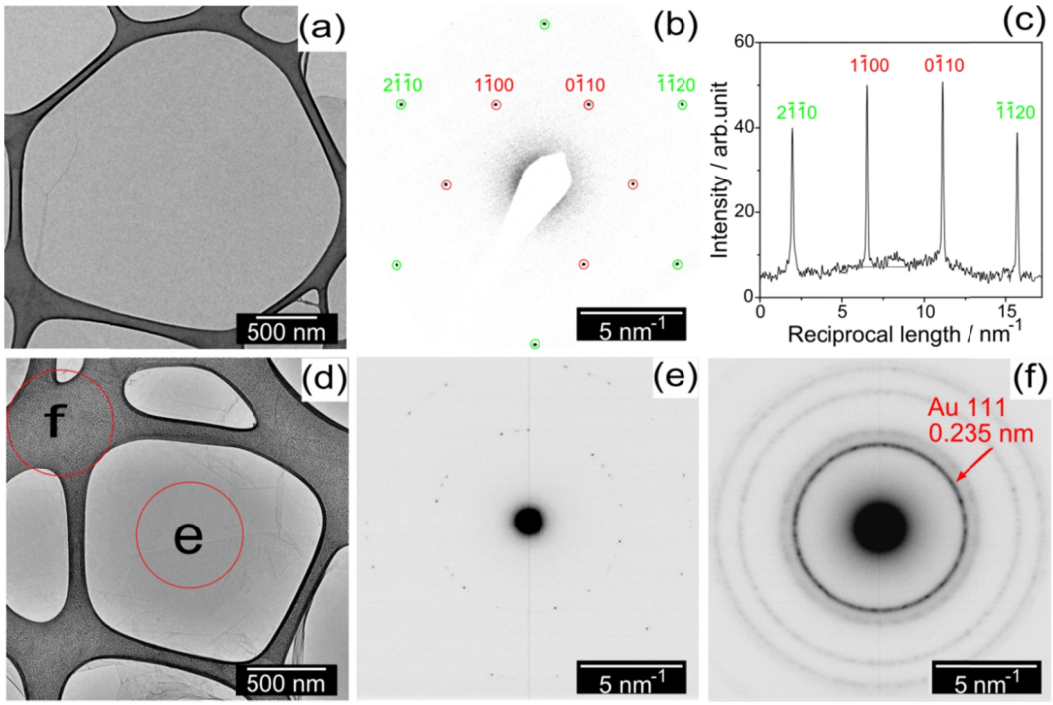

Figure 3.5 (a) TEM image of a single rGO sheet on a lacey carbon grid. (b) SAED from the centre of the region in (a). (c) Intensity profile across the diffraction spots labelled in (b). (d) TEM image of rGO sheets on Au coated lacey carbon grid; (e & f) inverted SAED patterns from the regions marked as e and f respectively.

The GO dispersion was converted to reduced graphene oxide (rGO) suspension by using hydrazine (see Chapter 2). For a TEM study the samples of rGO were made by drop casting rGO dispersion onto lacey carbon grids and letting them dry for 30 minutes in air. The study of the structure of rGO was performed in the same way as for GO. *Figure 3.5a* is the TEM image of the rGO suspended across the lacey carbon support grid. A thin wrinkle in the rGO is visible to the left of the image. The SAED pattern from the central region of the rGO (*Figure 3.5b*) displays a hexagonal set of reflections similar to GO. Again the reflections of $1\,\bar{1}00$ - type are marked with a red circle and $2\bar{1}\bar{1}0$ -type with green circles. The intensity profile across the indexed spots (Miller – Bravais notation) is shown in *Figure 3.5c* and the ratio of intensities of $1\,\bar{1}00$ to $2\bar{1}\bar{1}0$ types of reflection was found to be 1.5 $\pm$ 0.2 from 5 different single sheet SAED patterns. For the accurate measurements of the

lattice spacing in rGO, Au coated lacey grids were used and the rGO SAED patterns were calibrated accordingly. The central part of the TEM image of rGO on a gold coated lacey grid (*Figure 3.5d*) shows 3 sheets of rGO with overlaps and wrinkles. The corresponding Au and rGO SAED patterns from the encircled regions in the image are shown in *Figures 3.5e and f*. After calibrating the rGO SAED patterns the lattice spacing corresponding to the $1\,\bar{1}00$ type reflection in rGO was found to be 0.2127 $\pm$ 0.0003 nm and is identical to that of GO and FLG within the limits of experimental error.

Thus rGO, like GO, preserves the hexagonal lattice structure and the carbon to carbon bond length of graphite. The ratio of the intensity of $1\,\bar{1}00$ to $2\bar{1}\bar{1}0$ types of reflection is higher than that for graphene[113]. As explained in the earlier section the increase in the relative intensity of the $1\,\bar{1}00$ spot is attributed to the remnant functional groups resulting in the displacement of the carbon atoms from their equilibrium positions.

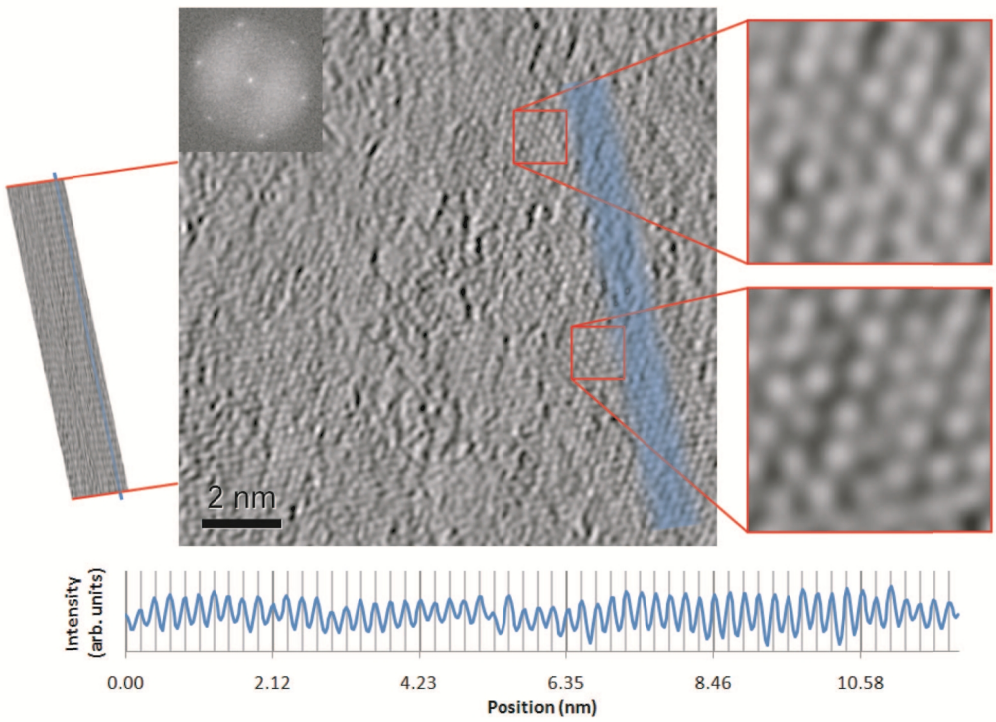

Figure 3.6 (Main panel) HR-TEM image of a single layer of GO (inset top left – FFT of the image); (right) magnifications of the regions as indicated, showing the GO crystalline lattice; (left) digitally compressed part of the image (to 10% of its width) along the direction marked by the red lines, the clearly visible parallel lines demonstrate the regular period of the lattice planes; (below) line plot of the average intensity along the blue line (indicated on both compressed and original images), the grey lines are guides to the eye. HR-TEM image –courtesy of Dr. Zheng Liu and Prof. Kazu Suenaga, Research Centre for Advanced Carbon Materials, Tsukuba, Japan.

While diffraction patterns provide information about the average underlying crystal structure of the material, high resolution TEM (HR-TEM) imaging shows the detailed local structure. However, in high resolution imaging damage can occur rapidly due to the high flux of electrons, which is not the case whilst acquiring diffraction patterns, since the electron beam is fully spread. The HR-TEM image of GO was obtained by Dr. Zheng Liu, Research Centre for Advanced Carbon Materials, Tsukuba, Japan. The images were obtained on a JEOL 2010F fitted with CEOS aberration corrector with the spherical

aberration coefficient set to +1 μm and operated at 80 kV to avoid knock on damage. *Figure 3.6* shows the HR-TEM image of a GO sheet. SAED pattern (not shown) and a fast Fourier transform (FFT) of the image (inset) indicate that the GO here consists of a single sheet. The hexagonal crystal lattice in GO is clearly visible in many regions as well as in the enlargements on the right. The image, on average, reveals a crystalline backbone with superimposed disorders and defects. Similar regions of amorphous adsorbates, recognised as adventitious carbon[119] by surface scientists, have been observed in the HR-TEM of graphene.[20, 111] On the right of the image the region shown in blue has been digitally compressed to 10 % of its width along the direction marked by the red lines; the clear parallel lines demonstrate the consistent ordering in the crystal. At the bottom, the line plot of the average intensity across the blue line in the digitally compressed image clearly shows periodic arrangement of atoms. The spacing between the vertical gray lines matches with the lattice spacing in GO (approx. 0.212 nm according to the microscope calibration) indicating the existence of crystalline order over the length scales greater than 10 nm.

From TEM analysis here, the structure of the as-produced GO and rGO can be summarised as follows:

(1) On average GO preserves the crystalline order with hexagonal symmetry of the parent graphite.

(2) The carbon to carbon bond length in GO is 0.1421 ± 0.0007 nm which is identical to that in graphene.

(3) The size of the graphene like crystalline regions in GO is greater than 10 nm which is observed from the coherence length of the electron beam as well as in the HR-TEM image. Additionally, the range of the orientational order is over the entire GO sheet as evident from the SAED patterns.

(4) The oxygen functionalities in GO do not show any regular arrangement.

(5) When deposited by drop casting, the adjacent layers in GO do not show any preferential angle of orientation.

(6) The electron diffraction of rGO shows hexagonal pattern similar to graphene and the intensity of $1\,\bar{1}00$ – type spots is higher than that of $2\bar{1}\bar{1}0$ – type.

3.1.2 Comparison with the structures proposed in the literature

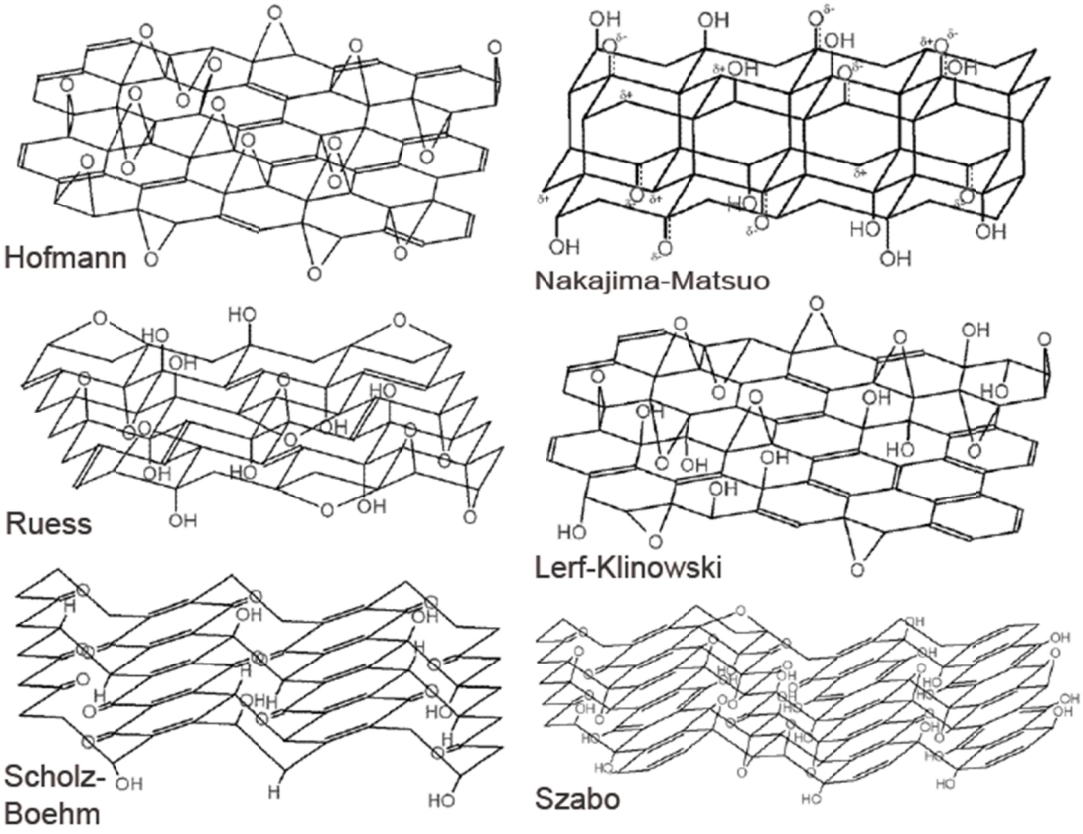

Figure 3.7 From top left to bottom right – proposed models of graphitic oxide by Hofmann, Nakajima – Matsuo, Ruess, Lerf-Klinowski, Scholz-Boehm and Szabo. Reproduced from Szabo et. al.[61]

Since GO is obtained from exfoliation of graphite oxide, the basal plane of GO can be compared to that of graphite oxide. In *Figure 3.7* the most prominent models that have been proposed for graphite oxide until recently are presented. The figure shows the

Hofmann model (1939)[63] showing random epoxy groups on the basal plane of graphene; the Ruess model (1946),[63] with epoxy and hydroxyl groups attached randomly to a wrinkled carbon structure; the Scholz-Boehm model (1957)[63] which is similar to the Ruess model but with carbonyl and hydroxyl groups; the Nakajima-Matsuo model (1988)[60] similar to the Scholz-Boehm model but with electron delocalization on the C=O groups; the Lerf-Klinowski (1998)[62] model which is similar to the Hofmann model but with random hydroxyl and epoxy groups and with the with $C-OH$ and $C-COOH$ group at the edges; and the model proposed by Szabo et. al.(2006)[61] showing random distribution of epoxy, hydroxyl and carbonyl groups on a wrinkled carbon structure.

Clearly, the models proposed by Nakajima-Matsuo, Ruess, Scholz-Boehm and Szabo do not suggest a uniformly hexagonal crystal structure. The amount of sp^3 carbon atoms in these models would reduce the lattice spacing or give extra diffraction peaks. As neither of these results is observed experimentally, we can deduce that these models are not applicable to graphene oxide here. The Hofmann model is not consistent with the XPS analysis which shows presence of hydroxyl, epoxy, carbonyl and carboxylic groups. Hence the most appropriate model is the Lerf Klinowski model which is consistent with the TEM analysis here as well as the complementary analysis techniques.

The electron diffraction studies of graphite oxide, a precursor to GO, have shown it to exhibit hexagonal order with oxygen groups attached in a disordered array.[64] From the observations here, GO has a graphene like basal plane with attached functional groups. Amongst the proposed models for graphite oxide the Lerf Klinowski model is the most appropriate for GO. TEM analysis of rGO performed here shows that the low magnification image and the SAED of rGO are indistinguishable from that of GO.

3.1.3 Conclusions on TEM study of GO

The Lerf-Klinowski models is now widely accepted to be a model close to the structure of GO and a consensus has been reached that GO consists of sp^2 carbon atoms randomly decorated by epoxy, hydroxyl, carbonyl and carboxyl groups.[56, 67] Yet, the size of the graphene like regions in GO is a matter of debate. Previously, studies based on STM and TEM have indicated that the graphitic regions in GO are of the size of up to 6 nm[67, 68]; however, in the STM and TEM images the effects of adsorbates and/ oxidative debris (as will be discussed in the next section) cannot be neglected. The electron diffraction results, here, have shown that the ordered regions are > 10 nm in size and the value is in agreement with the HR-TEM images; however, graphene like regions > 10 nm are incompatible with carbon to oxygen ratio of ~ 2:1 suggesting that the structure of GO must be re-examined. Hence in the next section the chemical and physical structure of the as produced GO are further investigated.

3.2 The role of oxidative debris

The composition of the as produced GO is significantly dependent upon the degree of oxidation which interdepends on the method of synthesis followed.[63, 65] Although GO forms a stable aqueous suspension, with the ratio of C:O roughly 2:1[63] when fully oxidised the composition of GO has been reported to change with increasing temperature.[63] A recent report showed that the chemistry of GO evolved at room temperature with a characteristic relaxation time of about one month.[120] All these reports point towards the indefinite composition and metastable nature of GO. Here, a detailed study on the chemical structure of the as produced GO was made and it was found that the as produced GO is composed of two components – one consisting of a graphene sheet randomly

decorated with oxygen groups and the other consisting of oxidised functional groups, here called oxidative debris.

Only in this section (3.2) of the chapter, the as produced GO is designated as aGO.

3.2.1 Evidence of oxidative debris – graphene oxide complex

A suspension of aGO in water was treated with different concentrations of NaOH and the effects are presented in the photograph, *Figure 3.8*. The top photograph was taken within 30 s of mixing NaOH with GO suspensions and the bottom photograph shows the same samples after 3 hr.

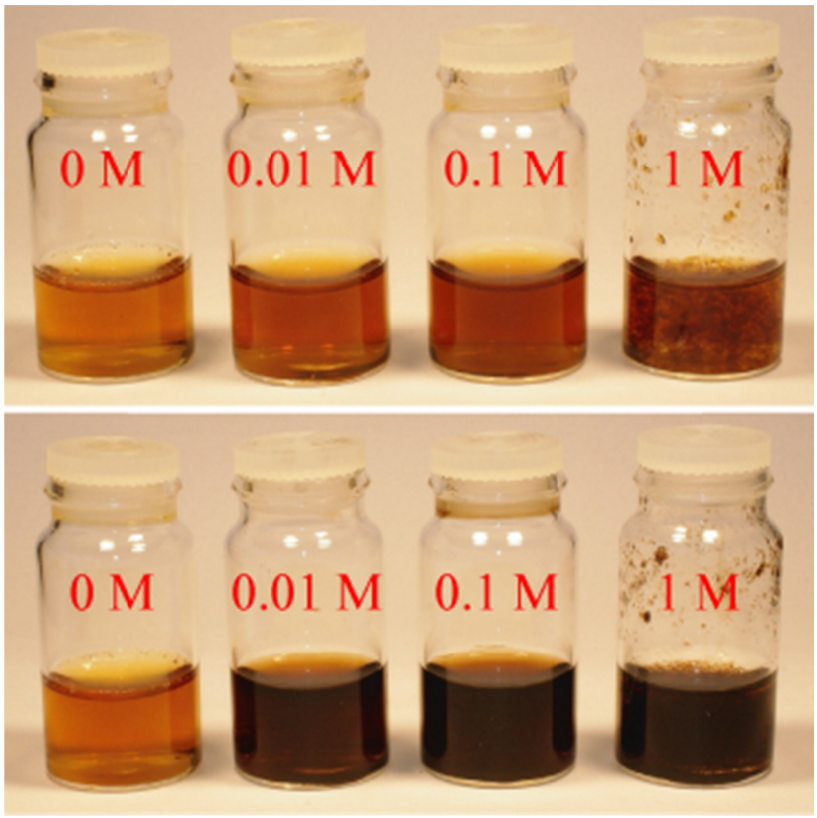

Figure 3.8 Top shows the photograph of the aGO mixture within 30 s of adding NaOH solution and the bottom after 3 hr. The concentration of NaOH from left to right is 0 M, 0.01 M, 0.1 M and 1 M as marked.

To 2.5 ml of 0.5 $mgml^{-1}$ aGO suspensions in water, equal amounts of NaOH solutions were added to get the final concentrations of NaOH in the mixtures as 0, 0.01, 0.1 and 1 M. As shown in the top photograph, the colour of the mixture with low concentrations of NaOH rapidly darkened while near instantaneous coagulation was observed with 1 M NaOH solution. After 3 hr (bottom photograph) the mixture with the highest concentration of NaOH (1 M) displayed two distinct phases – a black aggregate and a colourless supernatant. The mixtures with lower concentrations of NaOH also displayed darkening of the colour and eventually separated into a black aggregate and a colourless supernatant when heated at reflux for 1 hr (not shown here). The clear brownish colour of the aGO in the mixture without NaOH did not change with time.

In order to measure the mass of the black aggregate, a base washing procedure was followed. Dried aGO of known weight was sonicated in water to form a homogenous suspension and then refluxed with 0.1 M NaOH solution for 1 hr. The resulting black aggregate was separated from the colourless supernatant (1) by centrifugation at 11000 rpm for 30 min. The black aggregate was then reprotonated with 0.1 M HCl, followed by washing with distilled water and again separating the black aggregate from the colourless supernatant (2) by centrifugation as before. The black aggregate was then dried under vacuum and weighed. This resulted in a black powder that could not be resuspended in water by either stirring or sonication and was designated as base washed GO (bwGO). The two supernatants (1) and (2) were combined and reprotonated with HCl before being washed with distilled water and dried in vacuum. The resulting dried white powder was designated as oxidative debris (OD, it will be shown later that it contains oxidative debris) and mainly consisted of NaCl salt as a result of neutralisation of the NaOH used to wash the aGO. Knowing the mass of NaOH and HCl added in the process, the mass of NaCl

formed was calculated and it was found to be 97% of the OD. Table 3.1 presents the mass of OD extracted after subtracting the calculated mass of NaCl in each run.

Table 3.1 The yield of bwGO and OD against the mass of aGO in 4 individual tests. Tests 2,3 and 4 courtesy of Joseph J Moore, University of Warwick.

	Test 1	Test 2	Test 3	Test 4	Average
Mass of aGO	19.5 mg	0.1474 g	0.1545 g	0.1596 g	
Yield of bwGO	13.2 mg	0.0928 g	0.0991 g	0.0997 g	
Yield of OD	4.3 mg	0.0611 g	0.0281 g	0.0517 g	
% of bwGO	68 %	63 %	64 %	62 %	64 ± 2 %
% of OD	22 %	41 %	18 %	32 %	29 ± 9 %

Table 3.1 shows 4 different tests of base washing of aGO, out of these, test 2, 3, and 4 were done by Joseph J Moore as part of an undergraduate summer project, Department of Chemistry, University of Warwick. From 4 different occasions of base washing aGO (Table 3.1) the mass of bwGO was found to be 64 ± 2 % and, by separate independent measurement the mass of OD was found to be 29 ± 9 % of the mass of aGO.

Another set of control experiments were performed but with water instead of NaOH and the resulting supernatant and aggregate from the centrifugation were washed, dried and weighed in the same way as base washing of aGO. No measurable mass difference was observed between the aGO and dried aggregate while the yield of dried supernatant was too low to quantify.

Clearly, washing aGO with NaOH separates it into two components – bwGO and OD with the ratio of bwGO to OD ~2:1. The measurable mass of OD also indicates that small molecules like CO_2 and H_2O are not present as they would disappear in drying.

3.2.2 Characterisation of bwGO and OD

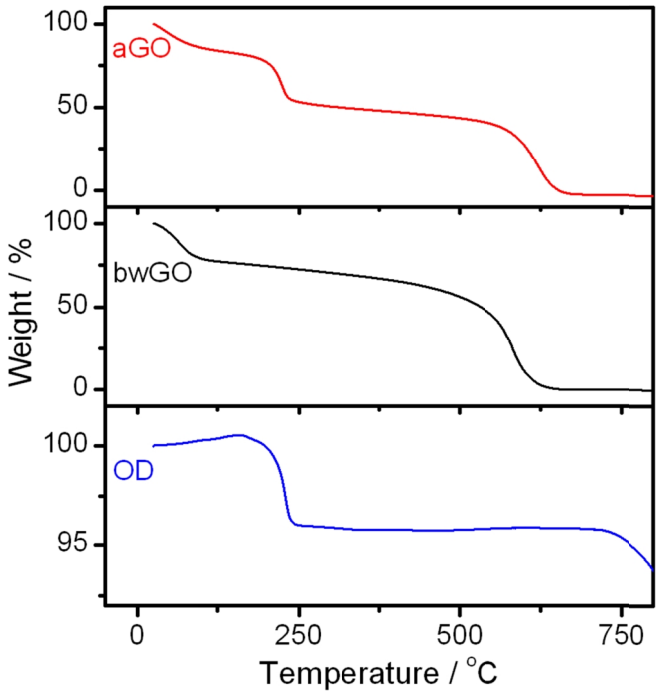

Figure 3.9 TGA of as produced GO (top), base washed GO (middle) and oxidative debris (bottom). TGA courtesy of Dave Hammond, department of Physics, University of Warwick.

For structural analysis, aGO, bwGO and OD powder samples were dried in vacuum. *Figure 3.9* shows TGA (Metler-Toledo TGA/DSC system) of aGO, bwGO, and OD. The analysis was done in air at a heating rate of 10 ℃/min in a Metler-Toledo TGA/DSC system. The initial mass loss in aGO is recognised as the adsorbed water. The mass loss in the aGO at around 200 ℃ has been attributed to the decomposition of functional groups and that at around 600 ℃ to the burning of graphitic carbon.[66] The ratio of mass loss at 200 ℃ to that at 600 ℃ in aGO is roughly 2:1. bwGO shows a significantly reduced mass loss at

around 200 ℃ and burns completely at around 600 ℃. On the other hand, OD shows a mass loss of about 4 % at around 200 ℃ and none at 600 ℃ indicating no graphitic regions in OD. The rest of the 96 % of the mass is attributed to the NaCl salt present in OD and is consistent with the mass balance within the experimental error.

Reports on the HR-TEM of GO have shown graphitic regions of a few nm interspersed in carbonaceous adsorbates indistinguishable from the attached functional groups[67, 69] while samples baked at 300 ℃ have shown larger areas of graphitic regions.[121] In agreement with the TGA results here, burning of the oxidative debris at about 250 ℃ could be the major reason for observing cleaner graphitic regions in baked GO samples in TEM.

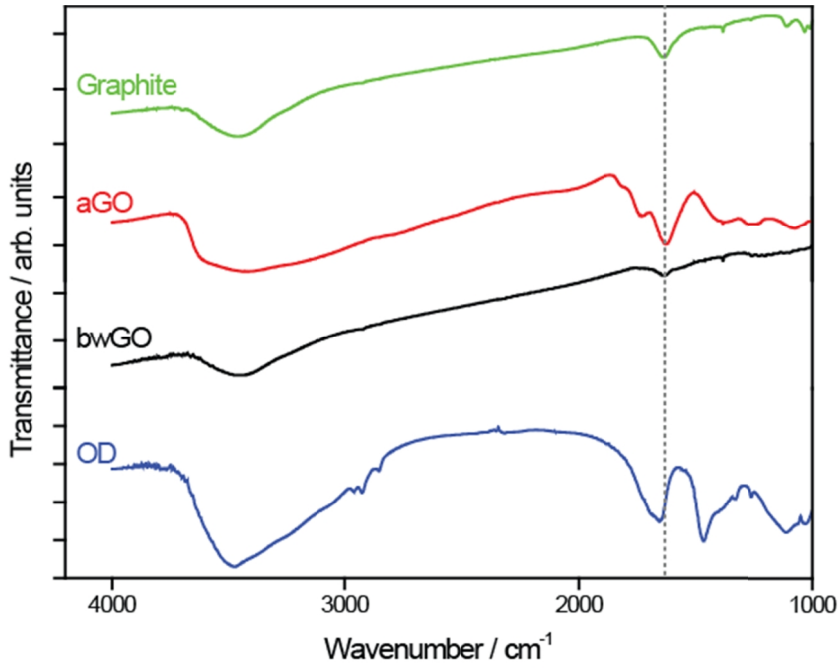

Figure 3.10 Fourier Transform Infra-Red (FTIR) spectra of graphite, aGO, bwGO and OD as marked on the graph. FTIR spectra courtesy of Dr. Jonathan Rourke, University of Warwick.

The Fourier Transform Infra-Red (FTIR) spectra of graphite, aGO, bwGO and OD powder shown in *Figure 3.10* were acquired on a Perkin-Elmer Spectrum One FTIR as KBr

discs. The spectra of aGO and OD are similar, while that of graphite and bwGO show fewer features. The broad band in the spectra of aGO at 3000 to 3800 cm^{-1} appears sharper in the OD spectra and significantly narrower in the spectra of bwGO and graphite. These regions have been associated with the vibration modes of C–OH, COOH and H_2O.[122-124] In the case of graphite it can be as a result of adsorbed water molecules. There are a number of sharp bands in aGO and OD below 2000 cm^{-1} which have been assigned to epoxy, carboxyl, carbonyl, hydroxyl groups and sp^2 hybridized C=C bonding.[122, 123] The peak at 1630 cm^{-1} in graphite, aGO and bwGO is assigned to sp^2 hybridized C=C bonding. It is not visible in OD. The FTIR spectra reveal that the degree of oxidation in OD is similar to aGO. A significant decrease in the covalent functionalization of bwGO is observed.

OD was readily soluble in water. A solution of OD in water was passed through a filter membrane of pore size 0.22 μm leaving no residue behind, suggesting that there are no large graphene like sheets in this component. The OD was also characterised by mass spectrometry performed by Dr. Lijiang Song, Department of Chemistry, University of Warwick. OD was found to comprise of oxidised carbon fragments such as $C_{19}H_{35}O_6$ and $C_{18}H_{33}O_9$.

Similar oxidised aromatic carbon fragments have been obtained after base washing of the oxidised CNTs and they have been referred to as oxidative debris or fulvic acids.[125] In a recent report on the alkaline treatment of graphene oxide, deoxygenation of GO with irreversible colour change was reported however, no mass loss after the treatment was stated and the supernatant was also not characterised.[126] Darkening of the colour upon base treatment had been previously observed for graphite oxide suspension and was attributed to disaggregation or exfoliation of graphite oxide lamellae.[127] However, this cannot be true for the already exfoliated sheets of aGO.

The mass balance, TGA, FTIR and mass spectrometry experiments, here, showed that heavily functionalised, low molecular weight aromatic carbon fragments are present in the aGO. These results indicate that OD is not the by-product of deoxygenation of GO as that would result in small molecules such as CO_2 and H_2O.

Since in the control experiments, on washing aGO with water, these fragments were absent, it is concluded that the basic medium detaches these carbon fragments/OD from the graphene like sheets in the aGO, and suggests that the OD is firmly bound to the graphene like sheets under acidic or neutral conditions. The strong bonding between the aromatic carbon fragments and graphene like sheet in the aGO could be due to $\pi - \pi$ interaction and hydrogen bonds.[125] In the presence of basic condition the interaction between the OD and oxidised graphene like sheet becomes repulsive due to the negative charge developed on the OD. After separation the bwGO and OD could not be recombined to produce the GO indicating that the original structure was metastable. The amount of OD in oxidized CNTs has been reported to be almost a quarter of the total mass[122] while in aGO here it is $\sim$1/3. The increased amount of OD in aGO could be attributed to the higher surface area of aGO. Thus, in analogy with oxidised CNTs the aGO consists of OD that is strongly adhered to the graphene like sheets in aGO.

Another important technique for characterising graphene like structures is Raman spectroscopy. The Raman spectra of aGO, bwGO and OD powder shown in *Figure 3.11* were acquired on a Reinshaw 1000 spectrometer with 633 nm laser excitation at low power to avoid sample damage.

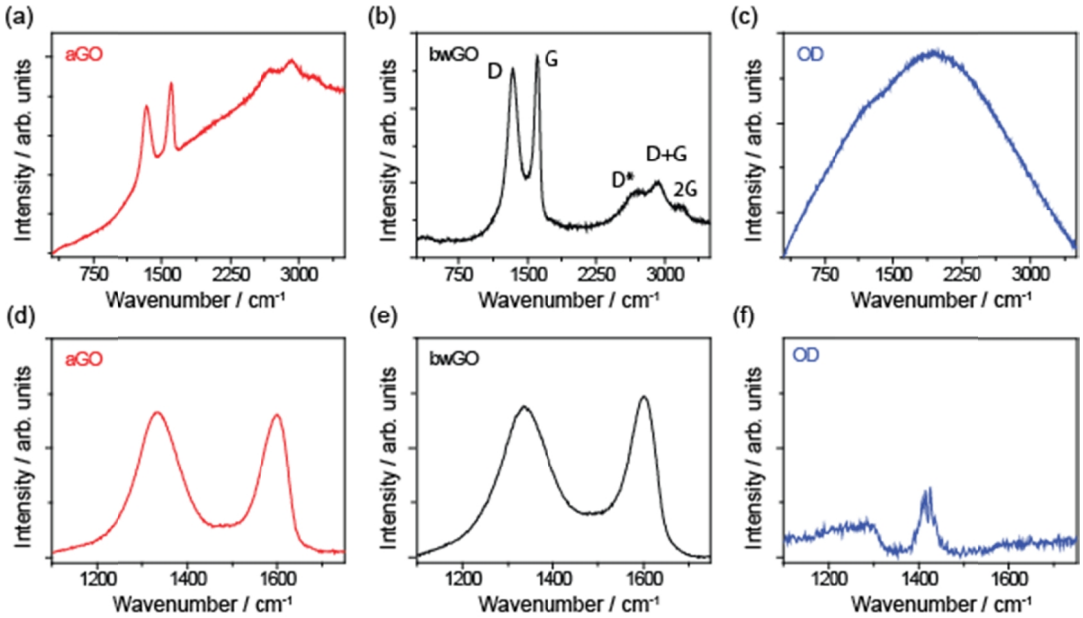

Figure 3.11 Raman spectrum of (a) aGO, (b) bwGO showing the usual D and G peaks and (c) OD showing no evidence of D and G peaks. (d), (e) and (f) are background subtracted Raman spectra from aGO, bwGO and OD in (a), (b) and (c) respectively. Raman spectra courtesy of Dr. Ian Kinloch, University of Manchester.

The Raman spectra of aGO and bwGO display G and D bands at around 1300 cm^{-1} and 1600 cm^{-1} respectively in the *Figures 3.11a and b* as well as in the background subtracted data in *Figures 3.11d and e*. The overtones in aGO and bwGO (D*, D+G and 2G) are also visible between 2500 cm^{-1} and 3300 cm^{-1}. The spectra of OD (*Figures 3.11c and f*) have no indication of G or D peaks. The ratio of integrated peak intensity of D/G peak in bwGO is 1.9:1 and identical to that obtained from the aGO spectra.

bwGO shows a strong evidence of a graphene like structure while the same structure features are absent in OD.

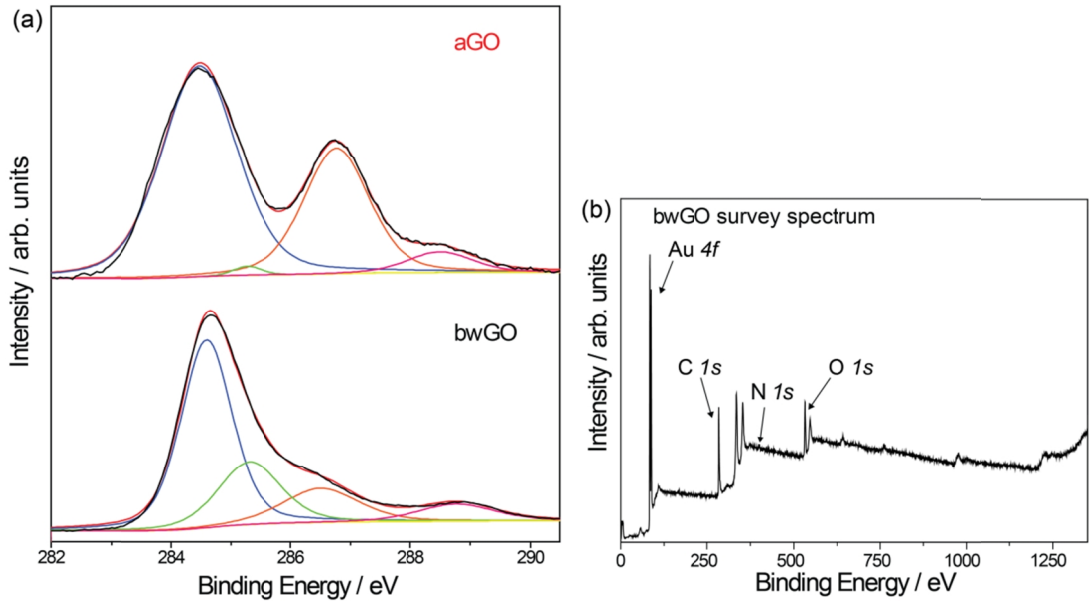

Figure 3.12 XPS spectra of (a) C 1s peak in aGO (top) and bwGO (bottom) and (b) survey spectra of bwGO. The coloured lines are fits to the spectra as described in the text. XPS spectra courtesy of Dr. Ajay Shukla, University of Warwick.

For XPS analysis an aGO, sample was prepared by spin coating a suspension of 1 mg ml^{-1} aGO onto a gold coated SiO_2/Si substrate; this resulted in a near monolayer coverage. bwGO sample was prepared by adding a drop of suspension of 1mg ml^{-1} bwGO in N-methyl-2-pyrrolidone (NMP) to a gold coated SiO_2/Si substrate and drying in vacuum; a thin, non-uniform, film was formed. XPS spectra were acquired using a monochromated X-ray source (Al Kα ($h\nu$ = 1486.7 eV) and electron energy analyzer EA125 from Omicron GmbH. For each sample Au *4f* spectra was acquired in order to calibrate the binding energy and the peak widths of the C *1s* peaks.

Figure 3.12a shows the fitted C *1s* peaks from aGO (top) and bwGO (bottom). The aGO peak is fit with Voigt peak profiles at 284.5 eV corresponding to C-C sp^2 bonding (blue), 285.2 eV to C-C sp^3 bonding (green)[107], 286.8 eV to epoxy and hydroxyl groups (orange), 288.6 eV to carboxyl (pink) and 290.0 eV (yellow) to carbon shake-up satellite.[45, 105, 108] The background is fit using a Shirley + linear background (not shown). Similarly, the

bwGO spectrum is fitted with Voigt peak profiles at 284.6 eV corresponding to C-C sp^2 bonding (blue), 285.3 eV to C-C sp^3 bonding (green), 286.6 eV to epoxy and hydroxyl groups (orange), 288.8 eV to carboxyl (pink) and 290.0 eV to carbon shake up (yellow). The survey spectra for bwGO in *Figure 3.12b* shows sharp peaks for Au, C, O and a small N *1s* peak at 399 eV. Nitrogen is expected from NMP but is insignificant and of the same level as the noise. No peak from sodium was observed.

The peaks other than C-C sp^2 and sp^3 correspond to the oxygen groups in the aGO. Taking the ratio of areas of C-C to C-O peaks we get C:O ratio for aGO as 2:1 which is consistent with previous reports.[45, 105] In the same way the ratio of C:O from bwGO spectra was found to be 4:1. Certainly, the C:O ratio in bwGO is lower than that in reduced and annealed GO. The slight difference in the binding energy of C–C peak of aGO and bwGO could be attributed to the charge transfer due to OD in aGO.[128]

However, these XPS measurements do not reflect the true stoichiometry of GO because: (1) the adsorbed amorphous carbon and carbons attached to hydrogen are accounted for in the carbon sp^3 peak and (2) in the epoxy-hydroxyl peak for every carbon atom, an oxygen atom is assumed although an epoxy group has 2 carbon atoms attached to 1 oxygen atom (separation of hydroxyl and epoxy groups in XPS difficult). Further, comparison of the C *1s* to the O *1s* peak does not give the true picture either, since O *1s* core level accounts for oxygen atoms attached to the graphene lattice as well as those from adsorbed H_2O and CO_2 molecules. As a result caution must be used in quantitative extraction of stoichiometries from XPS.

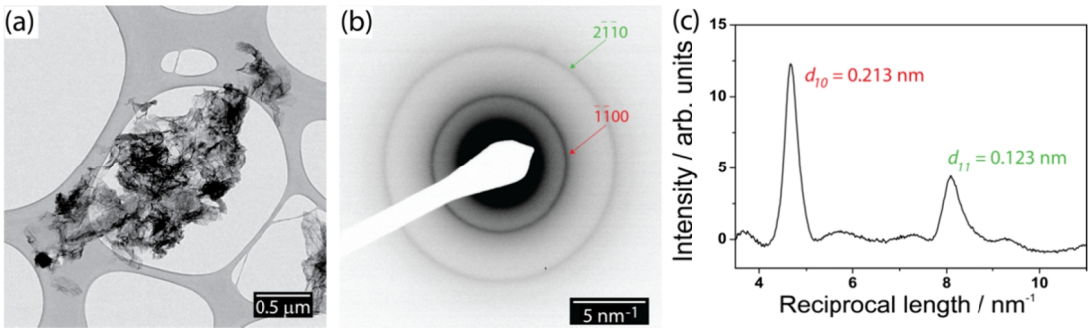

Figure 3.13 (a) TEM image of bwGO on lacey grid, (b) inverted SAED pattern from the centre of the image and (c) radially averaged and background subtracted intensity plot from the SAED pattern.

Similar to the preparation of aGO TEM samples, bwGO powder was sonicated in water, dropcast on a lacey grid and left to dry in air for 30 min. The TEM image in *Figure 3.13a* shows wrinkled sheets of bwGO across a hole in the lacey grid. Since the sheets are wrinkled the SAED pattern (*Figure 3.13b)* displays rings. The value of the lattice spacings from the inner and the outer rings are 0.213 and 0.123 nm respectively. The radially averaged intensity plot from the SAED pattern is shown in *Figure 3.13c* and the ratio of intensity of the inner to outer ring is 1.3.

These values of the lattice spacings are identical to the values measured from $1\,\bar{1}\,0\,0$ and $2\,\bar{1}\,\bar{1}\,0$ type of spots in aGO patterns in Section 3.1. This is consistent with a hexagonal crystal structure in bwGO. The inner ring is brighter than the outer ring indicating the presence of single sheets. As evident from the TEM image, single sheets of bwGO could not be deposited from a suspension in water, however, partial suspension was achieved upon sonication in NMP.

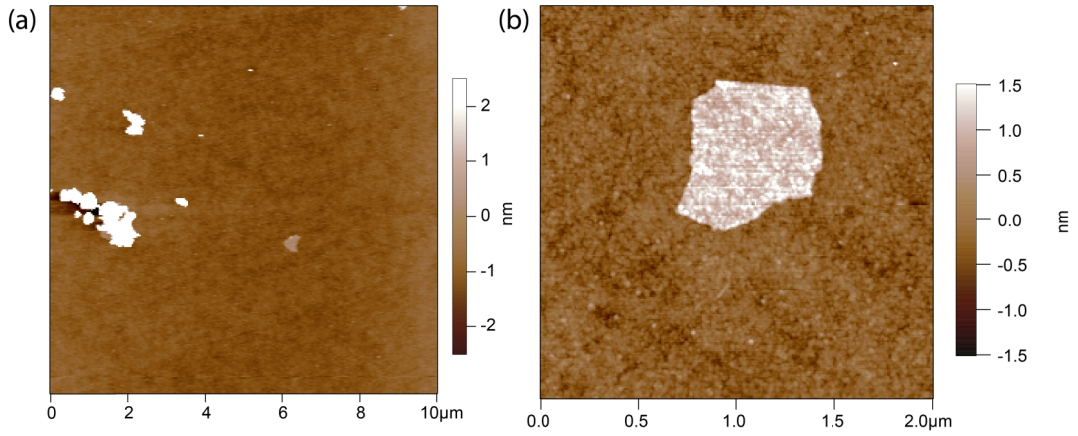

Figure 3.14 AFM topography of bwGO on silicon dioxide deposited by (a) drop casting from a suspension in NMP and (b) spin coating from NaOH suspension and then neutralising with HCl on the substrate.

Figure 3.14a shows AFM topography of bwGO deposited by drop-casting from a 0.5 mg ml^{-1} suspension in NMP. Near to the centre of the image a single sheet of thickness 1.1 nm is seen. *Figure 3.14b* shows the AFM topography of bwGO directly deposited by spin coating from a suspension in NaOH which was prepared by adding 1 ml of (0.15 mg ml^{-1}) aGO suspension in water to 1 ml of 0.01 M NaOH. It should be noted that this NaOH suspension still consists of OD. The suspension was spin coated on a silicon dioxide substrate then washed with water, neutralised with HCl and again washed with water. The thickness of this sheet was found to 1.2 nm.

In *Figure 3.14b* the sample was washed in water after spin coating from the NaOH suspension, it still shows single sheets as bwGO is hydrophobic, unlike aGO, which would be washed off in water. The thicknesses obtained in each case are consistent with the single sheet thickness of aGO.

Electrical characterisation

Because of the difficulties in re-suspending bwGO in water or NMP, bwGO thin films were utilized for electrical measurements. Thin films of bwGO were fabricated by

filtering a suspension of bwGO in NMP (1 mg ml^{-1}) through a 0.02 µm pore size alumina membrane giving a black shiny film. An equal amount of 1 mg ml^{-1} GO suspension in water, upon vacuum filtration, gave a deep brown dull film.

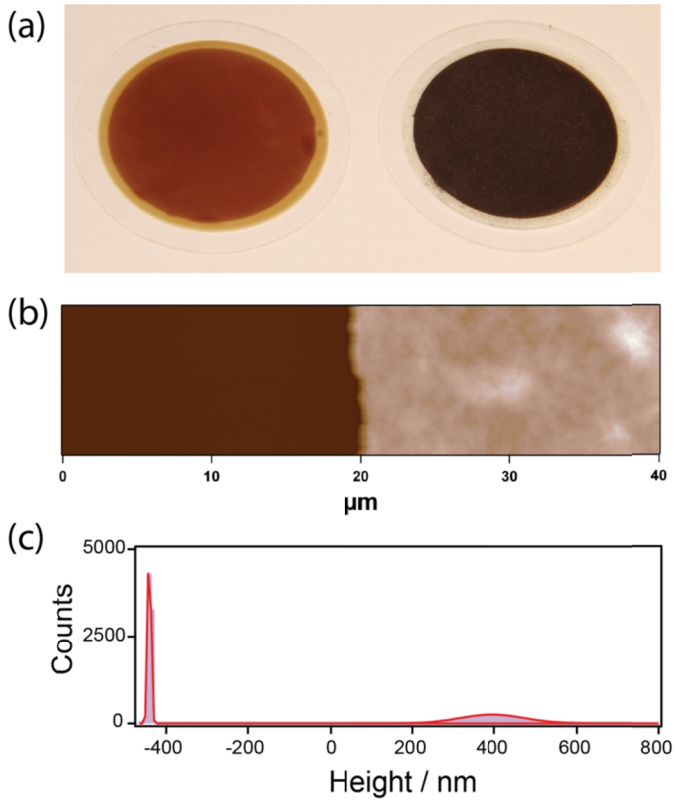

Figure 3.15 (a) Photographs of aGO (left) and bwGO (right) films on the alumina membrane. (b) AFM height image of the edge of bwGO film transferred on silicon dioxide substrate. (c) Histogram plot of the height image showing a sharp peak (left) from the substrate and a small broad peak (right) from the bwGO film. Gaussian peak fits are shown in red curve.

Figure 3.15a is a photograph of aGO (left) and bwGO (right) films on the alumina filter membrane. An AFM height image of the edge of the bwGO film transferred onto a silicon dioxide substrate is shown in *Figure 3.15b*. A Histogram plot of the height image (*Figure 3.15c*) showing two peaks fitted with Gaussian peak fits (red curves) gives the thickness of the film, 0.9 ± 0.2 µm.

For conductivity measurement gold contacts were sputter coated on the thin film on the alumina membrane using a shadow mask and the resistance of the film was measured. From the AFM height images the thickness of the film was found at 3 different places. The conductivity of bwGO from the measurements of 3 such films was 0.023 ± 0.006 S/cm. This is a two terminal conductivity and so does not account for the contact resistances; as a result it gives a lower bound on the actual conductivity. Thus, conductivity in bwGO is 5 orders of magnitude higher than that in aGO and just an order of magnitude lower than GO reduced by hydrazine or thermal annealing.[63, 129]

Since a homogenous suspension of bwGO was not yet obtained, a limited electrical characterisation was performed. Similar to reduction of aGO on the substrate, attempts to base wash GO film on the surface did not materialise as HCl corroded the substrate and resulted in contamination of the film. Improvements in the stabilisation of bwGO in solvents are needed for full structural and electrical characterisation as well as for application purposes.

The Raman, XPS and TEM results show that the bwGO is composed of oxidised graphene like sheets indicating that the base washing does not significantly change the structure. In addition, vacuum filtration of the bwGO suspension in NMP resulted in a dark shiny paper that is electrically conducting. Thus, the strong interaction between the strongly bound OD and the graphene-like sheets in aGO alters the electronic structure of aGO making it insulating.

3.2.3 Conclusions on the base treatment of aGO

We have demonstrated that base washing of the as produced GO decomposes it into two components – oxidised graphene like material (bwGO) and oxidative debris (OD). It was found that bwGO in the as produced GO is actually shiny, black, hydrophobic and an

electrically conducting material. It forms 2/3 of the total mass of the as produced GO. XPS investigations reveal that the amount of oxygen in bwGO is significantly less than aGO but is still higher than rGO reduced by hydrazine and annealing. The carbon to oxygen ratio in bwGO is 4:1 while aGO shows the ratio of 2:1. The lattice parameters obtained from the SAED patterns of bwGO are identical to that in aGO/graphene. TEM and Raman results confirm that the structure of bwGO is similar to the average underlying structure of the aGO or rGO.

OD was found to constitute 1/3 of the total mass of the aGO and was water soluble. From TGA and FTIR results it is found that OD consists of oxygen containing functional groups and mass spectrometry suggests that OD consists of oxidised polycyclic carbon fragments. Filtration of OD suspension in water through a 0.22 μm filter membrane indicated the absence of graphene like sheets. Raman spectrum further confirmed the absence of graphene like ordered material in OD.

These results indicate that due to the OD the as produced GO is hydrophilic and insulating. To summarise, we have found that the aGO is composed of functionalised graphene like sheets that are strongly adhered with low molecular weight, functionalised, carbon fragments referred to as oxidative debris. Thus the structure of aGO proposed in the literature needs revisiting.

3.3 Conclusions on the structure of aGO

Our results show that the structure of GO mainly consists of a carbon backbone with patches of graphitic regions at least 10 nm in size. The orientational order in GO is over the entire GO sheet and the oxygen containing functional groups in GO do not exhibit any long range ordering as evident in the SAED patterns. Further, there was no preferential orientation between the overlapping sheets. The study on base washing reveals that the as

produced GO consists of an oxidised graphene like sheet to which is bound the oxidative debris which acts as a surfactant and makes the aGO hydrophilic. Since the non-covalently bonded oxidative debris was found to be an integral part of the as produced GO the average structure of graphene oxide is re-examined here.

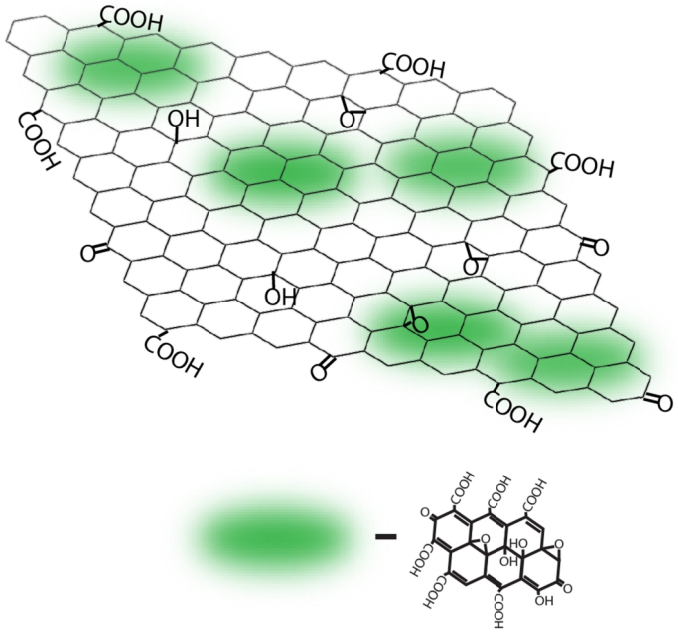

Figure 3.16 Schematic of the as produced GO: the oxidised graphene like material is bwGO and the green patches are ODs.

Based on the results obtained here, I propose a model of the as produced GO as shown in the *Figure 3.16.* The oxidised graphene like skeleton is the bwGO sheet and the OD groups are shown as green patches. The epoxy, hydroxyl and carbonyl groups are shown to be randomly attached to the carbon structure.

Finally, GO was also found to be transparent and stable under the electron beam. The stability, crystallinity and near transparent structure in TEM along with the hydrophilicity make GO an excellent candidate for a support film in TEM to study biomolecules and nanoparticles. In fact, recently there have been a number of reports on

the investigation of structure and properties of nanoparticles and biomolecules using GO or graphene as a support in TEM.[121, 130] In the next Chapter we use GO/rGO as a support to investigate the growth of metal nanoparticles and understand the structure of a technologically important molecular semiconductor – fluorinated copper phthalocyanine.

Chapter 4. **CMG Hybrid structures**

4.1 CMG hybrids

Graphene on its own is the ultimate flexible electronic material; combining graphene or CMG with other materials such as metals and organic molecules provides an opportunity to tune the functional properties for applications such as organic photovoltaic cells,[97, 131] sensitive and selective chemical[57, 132, 133] and biological[134, 135] sensors, and for catalytic applications.[76, 136] Understanding the interaction between metal atoms or organic molecules and graphene/CMG is important to develop these applications as well as to understand some fundamental processes involved in the formation of these hybrid systems.

Here, the interactions between different metals and CMG were investigated using TEM. The metals were deposited on GO and rGO by physical vapour deposition (PVD) and the growth morphology was studied. The GO-grids provided a near transparent

background and well defined diffraction pattern for calibration in TEM. As a result, accurate, reliable and reproducible results were obtained from images and diffraction patterns of CMG hybrid structures. Analysis of TEM images revealed that the final morphology of metals on CMG is governed by the interaction between graphene and the metal. In addition, an organic hybrid structure consisting of CMG and organic thin films of planar fluorinated copper phthalocyanine ($F_{16}CuPc$) molecules, an air stable n-type organic semiconductor, was also studied. The thin films were deposited on CMG by evaporation in vacuum and the crystal structure and molecular orientation in the organic film were examined. The molecules were lying perpendicular to the CMG substrate and the films showed a fibre texture.

4.1.1 Metal-CMG hybrids

With the rise in research of graphene-electronics the importance of understanding of the graphene-metal interaction cannot be disregarded. Graphene-on-metal has been studied for more than 40 years;[6, 33, 34] and the interactions between graphene and the metal have been found to depend on the metal.[6] However, due to the doping, the properties of graphene-on-metal are different from those of pristine graphene.[137] Although there are a number of reports on the growth of metal-on-graphite (mainly HOPG)[138-140] and CNT[141], using electron microscopy, growth of metal-on-graphene needs more intensive study.

Computational studies[86-88] have been made to understand the charge transfer between different metals and graphene and the type of binding between the metal adatom and graphene have been predicted. Experimental studies[80, 89] using electron microscopy have frequently concentrated on the growth of gold on graphene by PVD, but their interaction still needs further investigations. A few more studies have focussed on

the morphology of PVD gold nanoparticles on different number of graphene layers[80, 90, 92] and the difference in the morphology depending on the number of layers has been attributed to either quantum size effects[80] or electrostatic interactions.[90] Various other experimental studies have focussed instead on fabrication of metal-graphene system using solution phase deposition.[136, 142] However, in these cases the size and distribution of metal nanoparticles is dependent on the chemical approach rather than the interaction with graphene.

In this study different metals were deposited on CMG by PVD and their interaction with CMG was investigated by studying their growth morphologies. Metal-CMG hybrid structures were prepared for examination by different techniques, in particular TEM.

For TEM, GO and rGO suspensions were drop-casted on lacey grids and left to dry in air for 30 min. For AFM, SEM and XPS study the GO suspension was spin coated on Si/SiO_2 substrates as described in Chapter 2. rGO samples were prepared by reduction on the substrate as described in Chapter 2. Two different sputter coaters were used for metal deposition 1) a custom built DC magnetron sputterer at Leeds University (through collaboration with Prof. Brian Hickey) with a base pressure of 10^{-8} mTorr and argon pressure of 2.5 mTorr during sample growth and 2) a desktop sputter coater (Quorum Technologies SC7640) with a base pressure of 10^{-2} Torr at the University of Warwick.

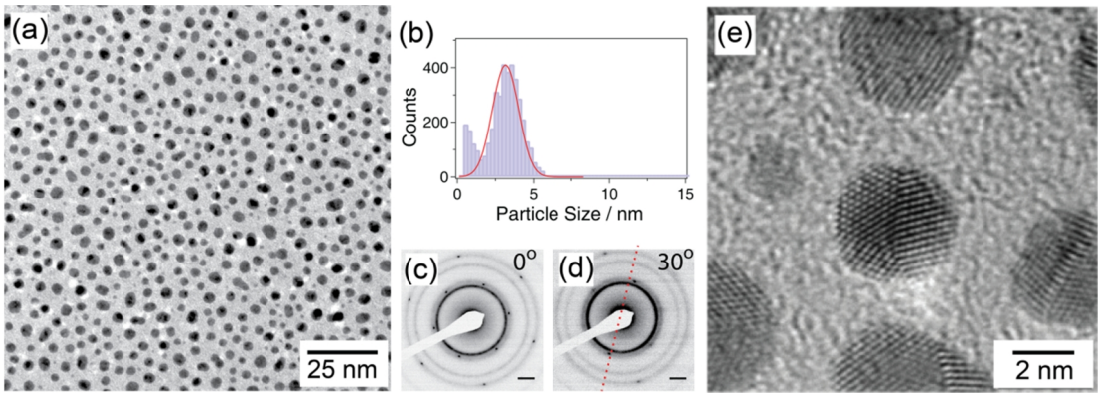

Figure 4.1(a) Bright field TEM image of Au of nominal thickness $\theta = 0.75$ nm[*] on GO. (b) Histogram plot of Au particle size from TEM image (a). (c) SAED pattern from the region of the image in (a) showing that the GO is single layer. (d) SAED pattern after tilting the sample by 30°, tilt axis is shown in dotted line. Scale bars on both SAEDs is 2 nm^{-1} (e) HRTEM image of Au on GO ($\theta \sim 1$ nm). HRTEM image courtesy of Dr. Ana Sanchez from Department of Physics, University of Warwick.

Figure 4.1a shows a bright field TEM image of Au deposition with nominal film thickness θ = 0.75 nm on a GO sheet. This Au deposition was done at Leeds using the low base pressure DC magnetron sputterer. Noticeably, the Au forms discrete islands rather than a thin film. The Au nanoparticles range in sizes but are typically a few nanometres in diameter. The change in contrast amongst the particles here is a result of diffraction contrast. The clear background of GO in low magnification TEM images made the analysis of the particle size distribution fast and reliable. From a TEM bright field image (part of which is shown in *Figure 4.1a*) the particle size was extracted using ImageJ,[143] a histogram of particle size[†] is shown in *Figure 4.1b*. The histogram clearly displays a bimodal island

[*]Here nominal thickness θ is the thickness the film would have if it were spread uniformly over the substrate.

[†]From software analysis the area of the nanoparticles was extracted and the particle size was estimated as the diameter of a circle of equivalent area.

size distribution (ISD) with a well-defined peak at around 3 nm and an increasing number of particles below 1 nm. The main peak at around 3 nm was fitted with a Gaussian distribution. The position of the main peak (i.e. the mean particle size) in the distribution from the histogram of *Figure 4.1b* is d_{peak} = 3.6 nm and the FWHM of the fit is σ_{peak} = 2.1 nm. Averaging over a number of such single sheet images the mean particle size was extracted to be d_{peak} = 3.60 $\pm$ 0.02 nm and the width of the Gaussian fit was found to be σ_{peak} = 2.19 $\pm$ 0.09 nm. Due to the uncertainties in the thresholding procedure the particles below 1 nm in diameter were disregarded and the island number density *n* was found to be 25500 $\pm$ 500 μm^{-2}.

The SAED pattern from the region of image in *Figure 4.1a* is shown in *Figure 4.1c*. A single hexagonal set of sharp spots from the GO and a series of concentric rings from the Au nanoparticles are clearly seen. In the GO pattern, the single set of spots with the inner spots brighter than the outer ones, indicate that it is a single sheet of GO (as explained in Chapter 3). To acquire SAED patterns an aperture of diameter size 0.6 μm was used so that approximately 7000 nanoparticles contributed to the Au diffraction pattern shown here. The ring pattern from Au indicates that the particles are not oriented in a particular crystallographic direction in the plane of GO. The SAED pattern shown in *Figure 4.1d* is obtained after tilting the sample by 30° relative to the electron beam, along the tilt axis shown in the red dotted line. As expected, the GO diffraction spots away from the tilt axis disappear.[25] The concentric rings do not change in shape or intensity indicating that the nanoparticles are crystallographically randomly oriented relative to the GO.

Figure 4.1e shows the HR-TEM image of the Au nanoparticles on GO deposited for $\theta \sim$ 1 nm using the desktop sputter coater at Warwick. Lattice planes are clearly visible with domains oriented in random directions. Also faceting is visible suggesting that the atoms can diffuse and rearrange on the surface of the nanoparticle. Both sputter coaters

gave samples that showed bimodal ISD and random crystal orientations, suggesting that the growth of Au particles is not significantly affected by the base pressure of the sputter coater.

Au was simultaneously deposited on GO coated on Si/SiO_2 and investigated by AFM and SEM. The deposition showed similar morphology (images shown in Section 4.1.4) but due to tip convolution effects and the lower resolution of SEM compared to TEM, particle size analysis was not possible on these samples.

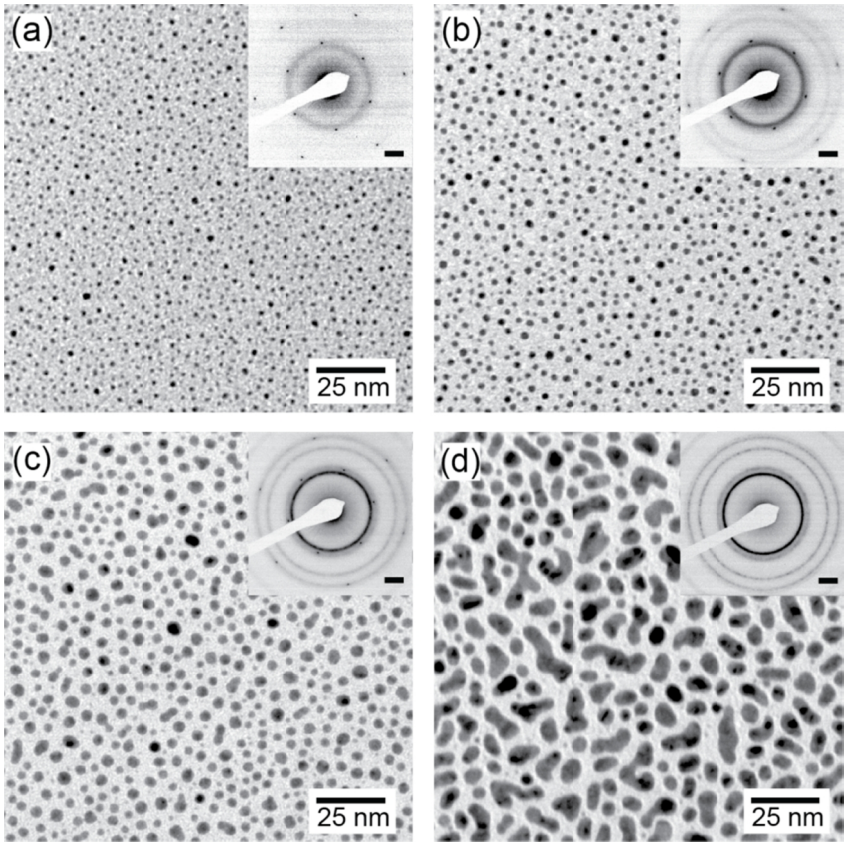

Figure 4.2 Bright field TEM images of Au nanoparticles on GO with nominal deposition thicknesses of (a) 0.15 (b) 0.3 (c) 0.75 and (d) 1.5 nm. Insets of the figures show the respective SAED patterns and the scale bars on the patterns are 2 nm^{-1}.

To investigate the growth kinetics involved in the growth of Au nanoparticles on GO, Au was evaporated with successively increasing nominal thickness, θ, at the growth

rate of 0.07 nm per second using the DC magnetron sputterer at Leeds. *Figure 4.2a, b, c and d* show bright field TEM images of Au evaporated on GO corresponding to nominal thicknesses of 0.15, 0.3, 0.75, and 1.5 nm respectively. The corresponding SAED patterns from the regions of images are shown in the respective insets. The inset diffraction patterns in *Figure 4.2a, b, and c* show single sets of hexagonal patterns from GO with concentric rings from Au. These patterns clearly indicate the presence of a single sheet of GO in these images. In the SAED pattern, *Figure 4.2d,* the GO spots are obscured by the strong diffraction from the Au nanoparticles.

With increasing θ the particle size increases and the number density decreases. A detailed analysis of the particles was performed by averaging over several images for each nominal thickness θ. The statistics on the particle distributions are shown in *Figure 4.3.*

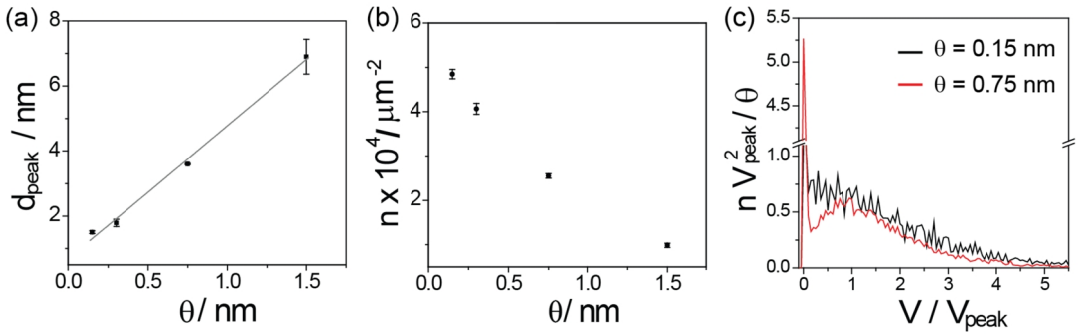

Figure 4.3 (a) Particle size d_{peak} as a function of nominal thickness θ with linear fit shown in grey, (b) particle number density n as a function of θ for particles larger than 1 nm in diameter and (c) comparison of scaled volume ISDs for θ = 0.15 and 0.75 nm showing scale invariance of ISDs.

Using the definitions of island number density *n* and mean particle size d_{peak}, the statistical analysis in *Figure 4.3* was performed. Representative images are shown in *Figure 4.2*. The variation of mean particle size d_{peak} as a function of nominal thickness θ is shown in *Figure 4.3a*. Similarly, the variation of particle density with θ (for particles larger than 1 nm) is shown in *Figure 4.3b*. As can be seen, the particle size d_{peak} increases linearly and the

density n decreases with nominal thickness θ. This suggests that as the deposition time increases the probability of arriving atoms being captured by existing clusters increases as does the probability of existing clusters coalescing.

Figure 4.3c is the comparison of the scaled volume* of ISDs for θ = 0.15 and 0.75 nm. Interestingly some of the ISDs show scale invariance i.e. when the island size and the number density are appropriately normalized† to the mean island size and effective coverage then all the coverages fall onto a universal curve.[144] In other words, scale invariance suggests that the microscopic processes are identical across a coverage range. In *Figure 4.3c* the scaled volume ISDs appear similar for the two different values of θ for the value $V/V_{peak} \geq 1$ nm; indicating that the growth processes for large clusters are similar across this coverage range. For the value of $V/V_{peak} \leq 0.5$ nm the ISDs do not scale. The scaled volume ISD has no clear dip for θ = 0.15 nm; and for θ = 0.75 nm the peak at lower values of V/V_{peak} is more pronounced. This suggests that different diffusion and coalescence rates are dominant at different stages of growth. The existence of bimodal ISDs suggests that there are two length scales on the surface at which the clusters interact: possibly two diffusion lengths associated with migration of clusters and adatoms respectively. This scale invariance was not observed in the ISD for $\theta = 1.5$ nm indicating that it does not apply to the post coalescence regime. Note that these results are not consistent with stationary clusters which is the standard assumption made in the classical studies of film growth.

---

* The average nanoparticle volume, <V>, was calculated as the mean of (island area)$^{3/2}$.
† Here, the volume distribution of the islands is rescaled by V_{peak} (calculated from d_{peak}).

4.1.2 Determining the roles of diffusion and metal-graphene bonding

To understand the interaction with different metals, Ti, Fe, Pt, Pd, Au and Ag were deposited on GO. *Figure 4.4* shows the bright field TEM images of Ti, Fe, Pt, Pd, Au and Ag on GO. Ti and Fe were deposited in the DC magnetron sputterer with θ = 1.5 nm and the rest of the metals were deposited in the desktop sputter coater with θ = 1 nm. The corresponding SAED patterns are shown in the respective insets.

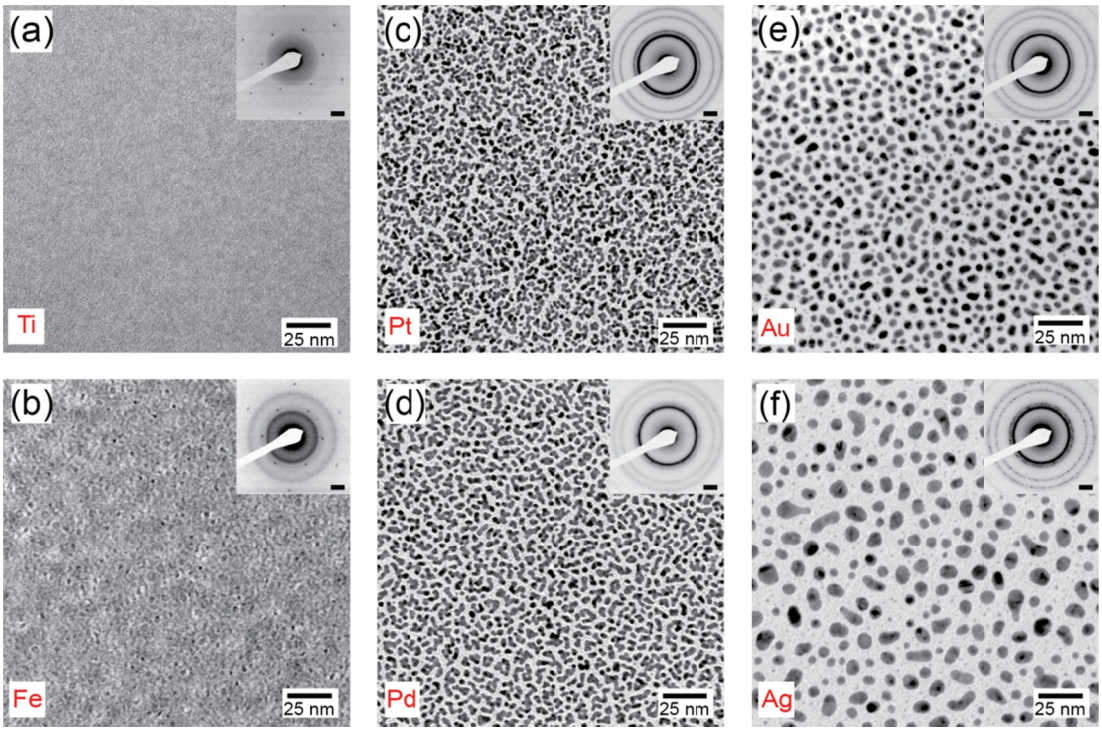

Figure 4.4 Bright field TEM images of (a) Ti, (b) Fe, (c) Pt, (d) Pd, (e) Au and (f) Ag on GO, the insets are the corresponding SAED patterns. The scale bars on the SAED patterns are 2 nm^{-1}. For Ti and Fe θ is 1.5 nm and for Pt, Pd, Au and Ag θ is ~ 1 nm.

The growth morphologies change significantly from Ti to Ag. Evidently Ti and Fe form thin films on the GO while the rest of the metals show island type morphology. As visible in the inset of *Figure 4.4a* Ti produces a broad diffuse ring in the diffraction pattern

indicating an amorphous structure of Ti. The observed morphology is that of a continuous film. Fe also forms a thin film on GO but the morphology is rather grainy and the SAED pattern shows broad yet well-defined concentric rings indicating better ordering and hence more clustering than for Ti on GO. Although Ti and Fe would have oxidized upon exposure to air before imaging in TEM, it should not change their coarse morphology on GO.

Pt and Pd both show branched island like growth. This type of morphology is a characteristic of coalescence of clusters without subsequent rearrangement. As a consequence the nanoparticles of these metals are not circular here. Pd has shown similar growth morphology on amorphous carbon however the particle density was much higher at particle sizes similar Pd on rGO here.[145]

Both Ag and Au show droplet like morphology; Ag shows larger particles and lower density compared to Au although both metals were deposited for the same thickness θ. The particles in Ag and Au appear quite circular and again the SAED patterns did not change in intensity or position upon tilting the sample, indicating non-epitaxial growth on GO.

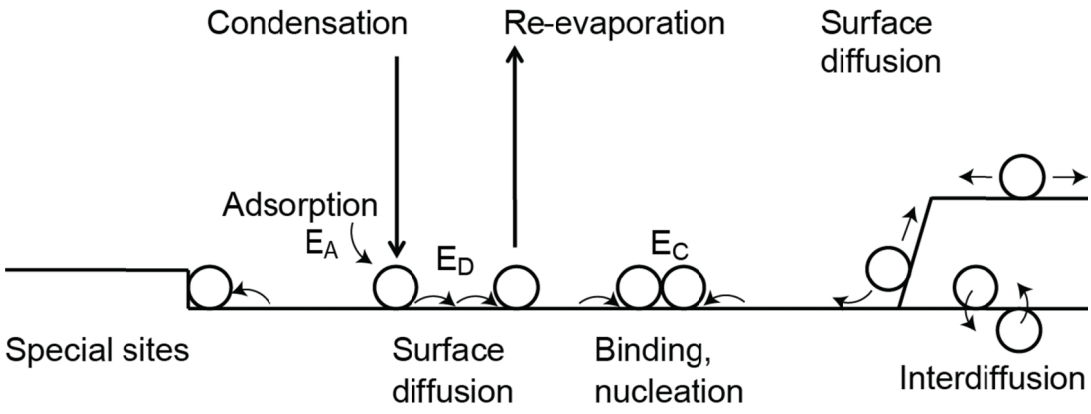

Figure 4.5 Schematic diagram showing the fundamental processes and energies involved in the nucleation and growth on surfaces (Adapted from Venables et al.[146]).

As shown in *Figure 4.5*, a number of fundamental microscopic growth processes are involved that govern the final morphology of the system. These processes involve adatom adsorption, diffusion of adatoms, binding of adatoms to adatoms or to existing clusters, dissolution into the substrate and capture at special or defect sites.[146] Since graphene has been found to be impermeable to gases including He,[147] the possibility of dissolution or interdiffusion of atoms is not valid for graphene as a substrate. Note that this standard model does not include cluster diffusion. Above all the final morphology is determined by the binding energies and energy barriers i.e. if the bulk cohesive energy E_C of the material is higher than its adsorption energy on the substrate E_A the resulting morphology is island like (droplets, clusters) while higher E_A means a film like morphology. Furthermore the diffusion energy barriers[146] that hinder the growth of an existing cluster, by slowing down diffusion of the adatoms to clusters, can be approximated by the difference in the strongest binding energy site E_A and binding energy of the lowest energy site E_W. Hence the diffusion rate for a single atom can be approximated as

$$D \propto \exp\left(-(E_W - E_A)/k_B T\right)$$

where k_B is Boltzmann's constant and T is temperature and E_W - $E_A \gg k_B T$. Diffusion processes occur at several stages of growth and include movement of single atoms to form clusters, coalescence of clusters and subsequent rearrangement of coalescing particles to give the final morphology. The ratio of the diffusion rate D to incident flux F of atoms decides the island growth kinetics and hence the final distribution of ISDs.

Close inspection of the images in *Figure 4.4* clearly indicates the involvement of different energetics depending on the metal. The circularity of these metals was measured by using the formula $C = perimeter / \sqrt{4\pi \times area}$; hence a circular particle will give C = 1. Using the definitions of d_{peak}, σ_{peak} and n from above, a detailed analysis of the growth of

Pt, Pd, Au and Ag on GO was extracted from the TEM images. The extracted information on the growth morphology is summarised in *Table 4.1*.

Recently there have been a number of theoretical reports on metal adsorption on graphene.[86, 88, 148, 149] We have re-examined the energetics of adsorption represented by E_A/E_C and $E_W - E_A$ (from Chan et. al.[88] and Hu et. al[86]) and compared them with the growth morphologies of metals here.

Table 4.1 The peak position d_{peak} (particle size) and width σ_{peak} along with density n and circularity C for Ag, Au, Pt and Pd are given in the table. The theoretically predicted values of E_A/E_C and $E_A - E_W^*$ for Au, Pd, Fe and Ti are taken from Chan et al[88] and those for Ag and Pt are taken from Hu et. al.[86]

metal	d_{peak} /nm	σ_{peak} /nm	n $\times 10^4$ /μm^{-2}	C	E_A/E_C	$E_W - E_A$ / eV
Ag	6.9 ± 0.2	4.9 ± 0.2	0.61 ± 0.04	0.84 ± 0.02	0.008	0.001
Au	5.1 ± 0.7	2.9 ± 0.6	1.5 ± 0.3	0.78 ± 0.04	0.025	0.007
Pd	5 ± 1	4 ± 1	1.3 ± 0.3	0.57 ± 0.05	0.278	0.038
Pt	7 ± 2	7 ± 3	1.2 ± 0.4	0.51 ± 0.02	0.268	0.173
Fe	–	–	–	–	0.175	0.517
Ti	–	–	–	–	0.385	0.568

The theoretically predicted values for ratios of adsorption to bulk cohesive energy E_A/E_C and approximate diffusion barriers $E_W - E_A$ for Au, Pd, Fe and Ti shown in the table are

* In Chan et. al. as well as in Hu et. al. E_A is designated as ΔE and E_W as E_a^{max}.

extracted from Chan et. al[88] and those for Ag and Pt are taken from Hu et. al.[150] For most of the metals above, the two reports are consistent with each other. As seen from the *Figure 4.5,* a higher ratio of E_A/E_C would mean the metal is relatively strongly bound to GO. If this dominates the growth the final morphology would be connected islands or film like; and a low value of the diffusion barrier E_W - E_A would mean higher diffusion rate i.e. increased mobility of adatoms to form 3D clusters.

From *Table 4.1*, depending upon their energetics, the metals are divided into 3 groups–

1) Drop like – this morphology is observed for the metals with fast diffusion and weak adsorption to graphene. It can be seen that the values of E_A/E_C and E_W - E_A are the lowest for Ag, compared with the other metals studied here. This clearly indicates that Ag poorly binds to GO and has a fast diffusion rate on the GO surface. As a result cluster morphology is seen for Ag. Au shows similar energetics to Ag hence the cluster morphology. However, Au shows a higher number density and lower circularity than Ag, correlating well with the slightly higher E_A/E_C ratio.

2) Branched growth - this morphology is dominated by a stronger adsorption of metal to graphene. The values of E_A/E_C and E_W - E_A for Pt and Pd are comparatively higher than those of Ag and Au. Accordingly, these metals show stronger binding to the GO surface and higher diffusion barrier resulting in the branched like cluster morphology. Further, the Pd particles are smaller compared to Pt due to the comparatively smaller diffusion barrier.

3) Film – this morphology is dominated by slow diffusion of metals on graphene. The E_A/E_C value of Fe is lower than that of Pd and Pt but the diffusion barrier is significantly higher and hence the grainy film like morphology is observed for Fe in the TEM images.

Finally, Ti shows the highest values of E_A/E_C and $E_W - E_A$ amongst the metals here, hence the film morphology.

Thus the relative values of energy barrier and ratio of E_A/E_C are in agreement with the growth morphologies observed here. We suggest that these parameters can be used to predict and control the growth morphology of metals on graphene.

4.1.3 Structural analysis of metals on GO

Electron diffraction analysis

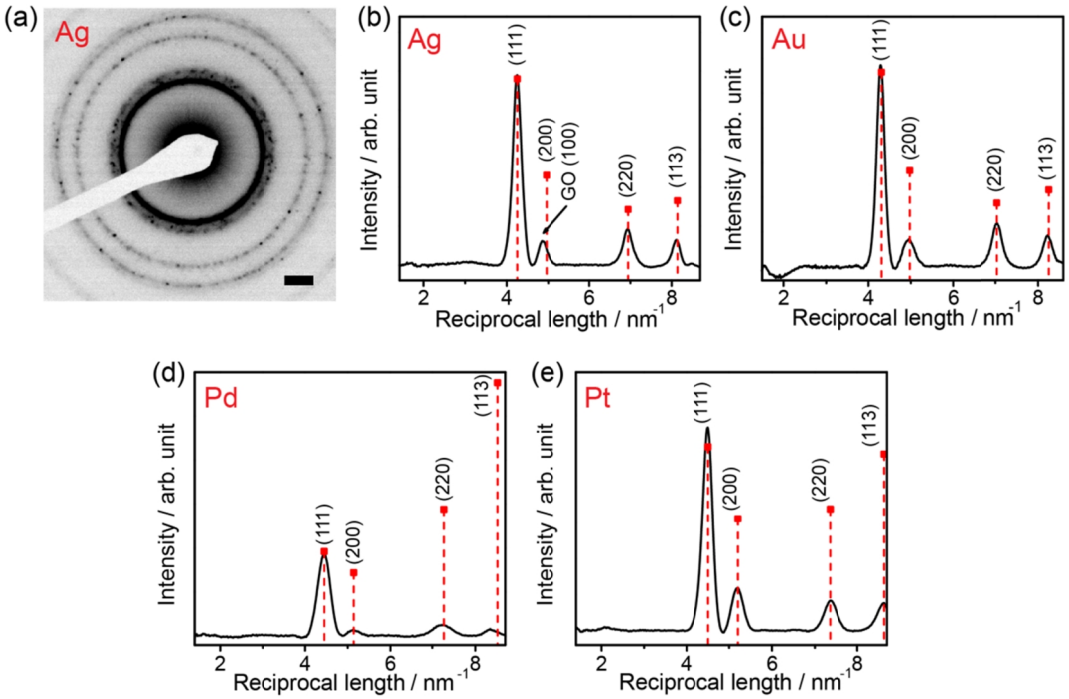

Figure 4.6(a) Inverted SAED pattern from Ag on GO (scale bar 3 nm^{-1}). Rotational average of the SAED patterns after background subtraction for (b) Ag, (c) Au, (d) Pd, and (e) Pt on GO. The vertical dashed line in each case is the powder diffraction calculated from CIF files mentioned in the text.

Figure 4.6a shows an inverted SAED pattern of Ag-GO sample. The SAED patterns obtained from different metal-GO samples were analysed by taking the rotational average

over the patterns and subtracting the background by fitting a spline. For calibration of the SAED patterns the GO (100) peak was used. The rotational averages from the SAED patterns are shown in *Figures 4.6 b, c, d, and e* for θ ~ 1 nm of Ag, Au, Pd and Pt on GO respectively. The vertical dashed lines in the figure are powder diffraction patterns calculated from the CIF files for Ag[151], Au[151], Pd[152], and Pt[152] using CrystalMaker®. The match of the positions of the observed and predicted peaks shows that the crystal structures are as expected for the bulk material. However, the calculated intensities do not match with the experimental values because of dynamical scattering.

Core level study of metals on GO

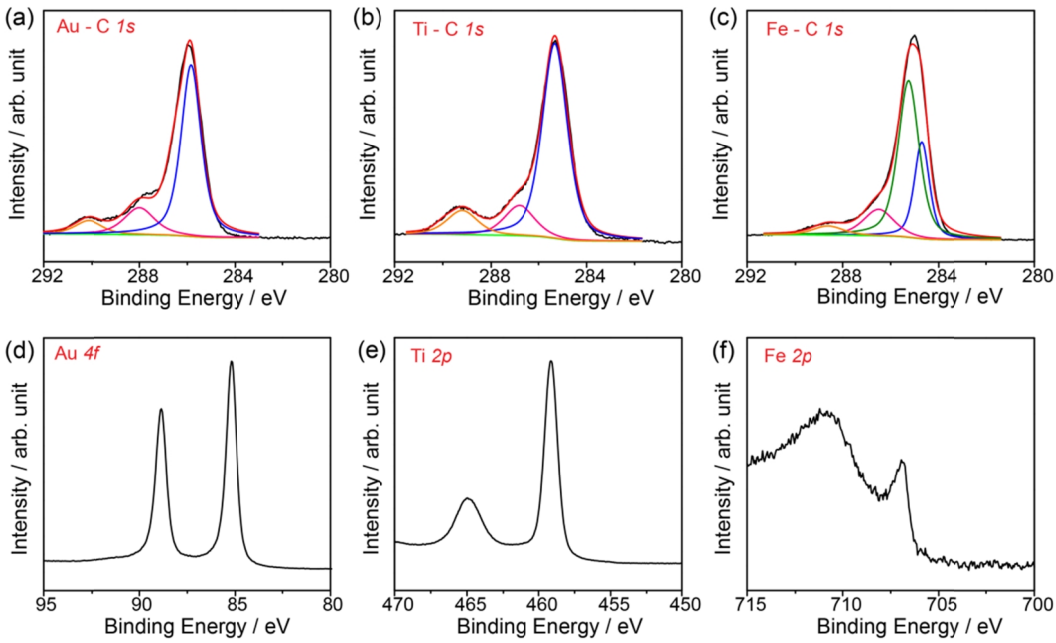

Figure 4.7 XPS analysis of C 1s core level spectra obtained for GO evaporated with (a) Au, (b) Ti and (c) Fe. XPS core level spectra for the corresponding metals are (d) Au 4f (e) Ti 2p and (f) Fe 2p. Raw data is shown in black and the coloured fits are as described in the text

XPS was also performed on the metal evaporated GO to further understand the metal-CMG interaction. The spectra were obtained using a Scienta ESCA300 spectrometer

at the National Centre for Spectroscopy and Surface analysis, Daresbury Laboratory, UK. Samples for XPS were prepared by spin coating a 1 mg ml^{-1} aqueous suspension of GO on Si/SiO_2 substrates. The C 1s peaks corresponding to the samples of Au, Ti, and Fe with a nominal thickness of 1.5 nm on GO are shown in *Figures 4.7a, b and c* respectively. The corresponding metal spectra are shown in *Figures 4.7d, e and f*. The C 1s spectrum, expected at 284.6 ± 0.2 eV, appears to have shifted to a higher B.E.; to 285.8, 285.3 and 285.4 in Au, Ti, and Fe coated GO respectively. The core level Au 4f spectrum in Au deposited GO occurs at 85.2 eV (doublet splitting 3.67 eV) which is higher than the expected position in bulk (84.0 eV).[153] Ti 2p core level shows the spectrum at 459.2 eV (doublet splitting of 5.7 eV) with a broad $2p_{1/2}$ peak characteristic of oxidized titanium.[154] XPS spectrum from the Fe evaporated sample shows a well-defined peak at binding energy of 706.9 eV for Fe $2p_{3/2}$ core level as expected for metallic iron. However another broad peak at 710 eV gives the evidence of presence of oxidized iron.[155]

Previously, the shift in the B.E. of the C 1s has been found to be due to charge transfer from metals to GO.[156] The work function of GO (4.9 eV)[102] is higher than that of Fe and Ti (4.3 and 4.5 eV respectively)[157] and lower than that of Au (5.1 eV)[157] hence the positive shift in the C 1s B.E. for of Fe and Ti coated samples is expected, but not for the Au coated sample. In addition, the amount of positive shift in the B.E. of C 1s is around ~ 1 eV indicating that it could also be due to charging while scanning as GO is insulating and it was deposited on Si/SiO_2 substrates. Hence, these positive shifts in the B.E. of the C 1s could be attributed to either the charging of the samples while scanning or charge transfer due to the deposited metals.

4.1.4 The layer effect

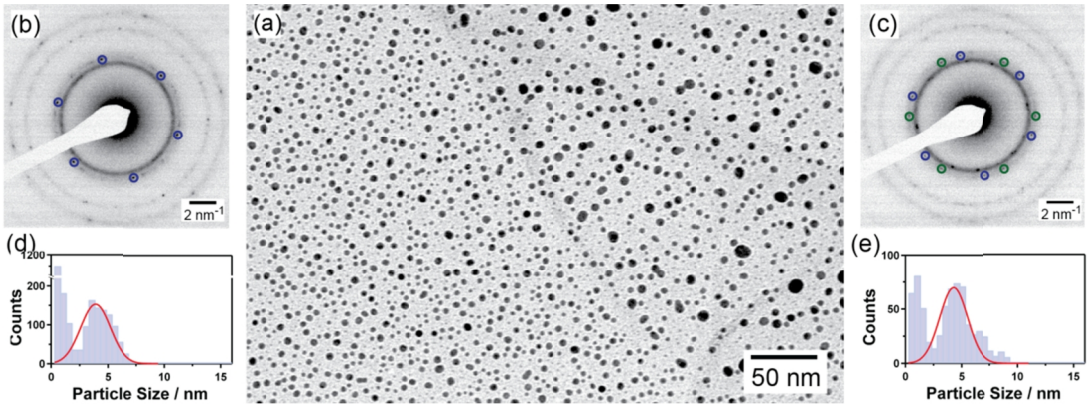

Figure 4.8(a) Bright Field TEM image of Ag on GO for $\theta \sim 1$ nm. SAED patterns from the regions of the image on the left (b) showing single hexagonal set of spots marked in blue circles indicating single layer GO and right (c) showing two hexagonal sets marked in blue and green circles indicating two layers of GO. The calculated histogram plots for the Ag particle size from the regions of single and double layer GO are on the left (d) and right (e) respectively.

Figure 4.8a shows a bright field TEM image of Ag deposited* on GO for $\theta < 1$ nm. The SAED patterns from the two regions, left and right, are shown in *Figure 4.8b and c* respectively. Both of the patterns show a series of concentric rings from Ag. A single hexagonal set of spots from the left region indicates it is single layer GO whilst the double set from the right indicates that it is two rotationally misaligned layers (see Chapter 3). The calculated histogram plots from the single and double layer GO are shown in *Figure 4.8d and e* respectively. The well-defined peaks in the plots are fitted with the Gaussian distributions shown in red.

* Ag was deposited on GO using desktop sputter coater.

The left region of the image shows Ag nanoparticles with higher density and smaller size compared to the right of the image. From the histogram plots the particle size was obtained to be d_{peak} = 3.9 ± 0.1 nm and d_{peak} = 4.3 ± 0.1 nm for single and double layer graphene respectively. The respective particle density was found to be $n = 1.3 \times 10^4$ μm^{-2} and $n = 0.7 \times 10^4$ μm^{-2} for the particles sizes above 1 nm. Clearly the number of layers of GO significantly affect the morphology of the adsorbed metals.

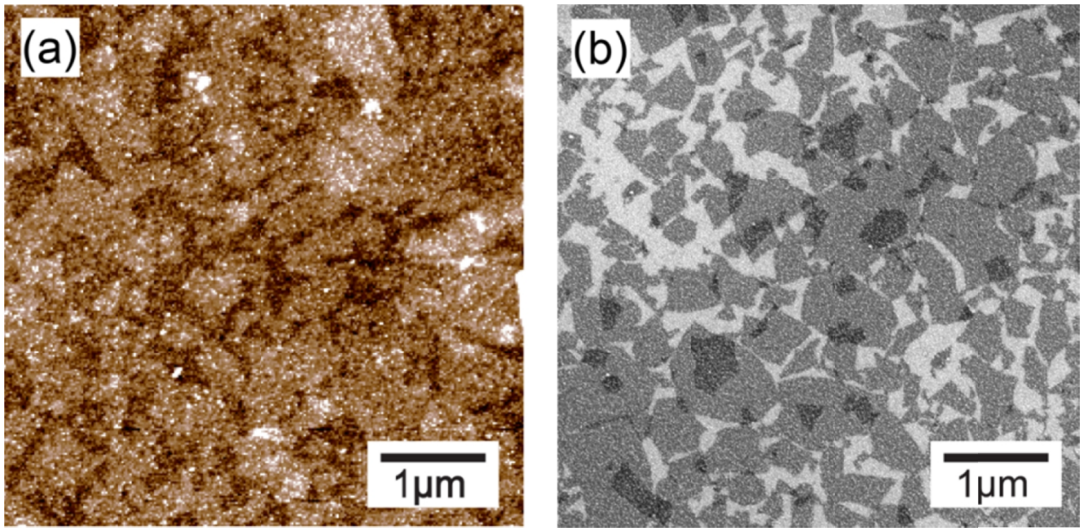

Figure 4.9(a) 5 μm square AFM topography (height colour scale is 4 nm full scale) and (b) SEM image of 0.3 nm Au evaporated on GO on Si/SiO$_2$ substrate.

This layer dependent morphology was previously observed for Au evaporated on graphene and associated to the A-B stacking.[80, 90] However, GO layers are not stacked but randomly mis-oriented. The AFM and SEM images in *Figure 4.9* also show layer dependent morphology even on substrate supported GO, suggesting that thermal gradient or surface topography is not the cause of this morphology. In another report the morphology was attributed to long range electrostatic interactions arising from charge transfer between the graphene and nanoparticle and the increase in electrostatic screening between single and multilayer graphene. Although GO is electrically insulating it preserves nanometer scale

conducting regions[56] and that could explain a similar layer dependent morphology observed here.

4.1.5 Probing the effect of functionalization on metal-graphene interactions

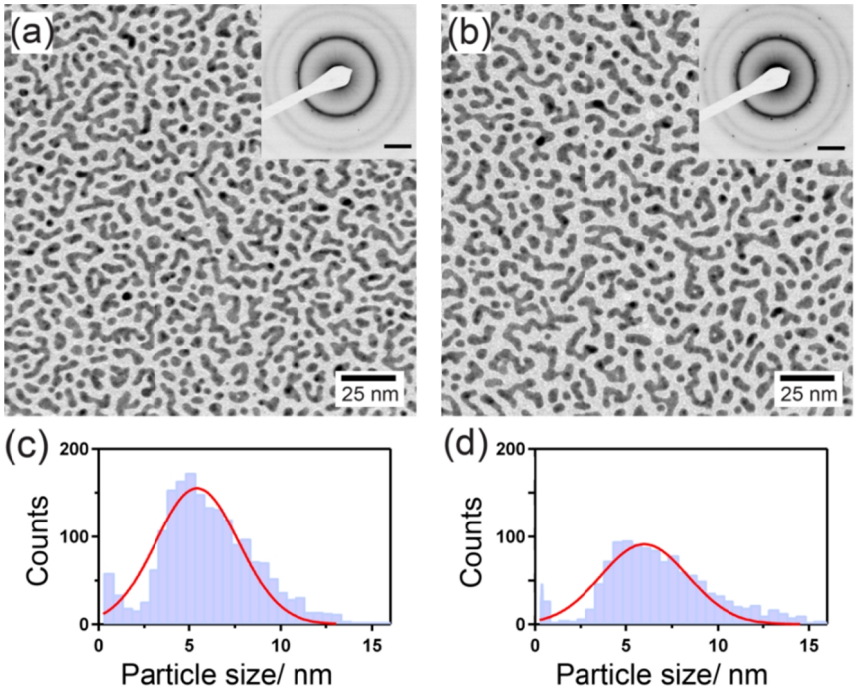

Figure 4.10 ~1 nm Pd deposition on (a) GO and (b) rGO with corresponding SAED shown in the respective insets. Calculated histograms plots in (c) and (d) are from the regions of images shown in (a) and (b) respectively. Scale bars on SAED is 3 nm^{-1}

Pd (nominal thickness 1 nm) was simultaneously deposited on GO and rGO (reduced on the lacy grid in hydrazine vapour and heated for 1 hr at 100 °C) using the desktop sputter coater. *Figure 4.10a and b* show the bright field TEM images of Pd deposited on GO and rGO with SAED patterns in the respective insets. Particle analysis was performed for both samples and the histogram plots show bimodal ISDs as shown in *Figure 4.10c and d*.

The morphology in both images appears to be similar. The particle size, density, and circularity were d_{peak} = 5.6 ± 0.5 nm, n = 8000 ± 1000 and C = 0.56 ± 0.04 for Pd on rGO and d_{peak} = 5 ± 1 nm, n = 13000 ± 3000 and C = 0.57 ± 0.05 for Pd on GO. These values are similar within the uncertainties due to variations in the flux of Pd during the deposition.

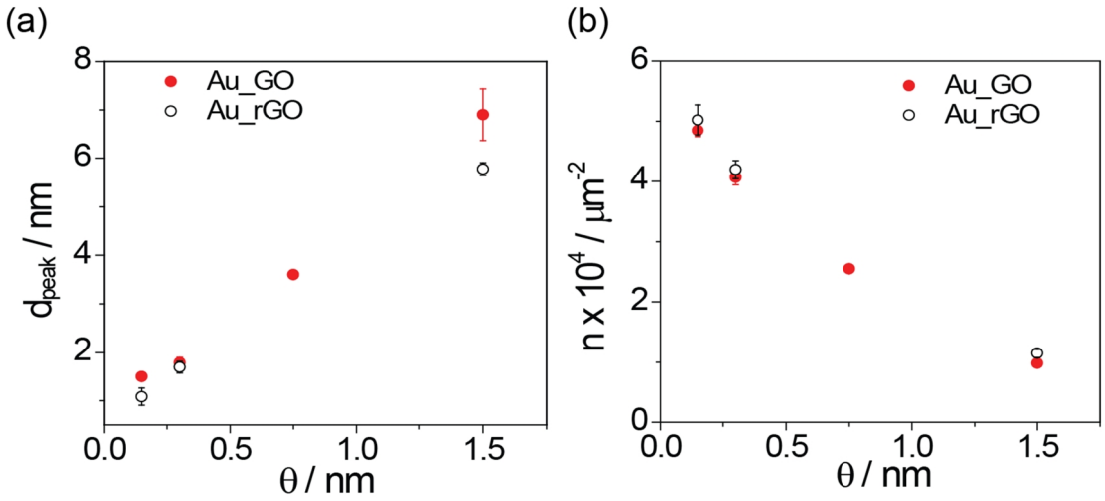

Figure 4.11(a) Particle size d_{peak} and (b) particle density n as function of nominal thickness θ for Au on GO shown in red solid circles and rGO shown in black open circles.

Figure 4.11 shows the statistics on variation of Au particle size and number density on GO and rGO as a function of the nominal thickness θ. It should be noted that these depositions were carried out in the DC magnetron sputterer and the GO and rGO samples were not deposited at the same time. Yet, the particle size d_{peak} as well as the particle density n are similar in both cases. Thus the morphology of metal is not significantly affected by the reduction of GO to rGO.

4.1.6 Conclusions on metal-graphene interactions

PVD was used to deposit different metals on substrate supported as well as on suspended CMG sheets. The final morphology of the deposited metal was governed by relative binding energies and migration barriers. For instance, Ti and Fe formed thin films

on GO indicating strong binding to graphene and slow diffusion; Pt and Pd showed branched islands indicating strong binding and diffusion; and Au and Ag formed droplet morphologies indicating weak binding and fast diffusion. When compared to amorphous carbon[145] the nucleation densities here are lower, but they are significantly higher than on HOPG[138, 139] and graphene[89] due to the presence of functional groups and/or adsorbates. In a recent report, metal atoms were shown to preferentially adsorb to hydrocarbons on graphene.[158] However, here the nucleation density and particle sizes are governed by the metal graphene interaction, as is evident from the dependence of the morphology on the number of graphene layers and the type of metal deposited. rGO showed similar metal growth morphology indicating similar microscopic processes involved in the nucleation and growth. The remarkable statistics and high resolution analysis that is readily possible with these systems make them very appealing for studying non classical nucleation and growth.

Understanding the microscopic growth processes as a consequence of graphene metal interactions is important for understanding charge transport, manipulation of graphene band structure and to design graphene based devices. More recently integration of graphene with organic molecules was widely investigated for opto-electronic applications.[97, 131] Theoretically, it was also suggested that the graphene-organic molecule interaction could be enhanced by constructing molecule/metal/graphene sandwich structures for graphene based sensing and switching devices.[159] Hence study of the interaction of organic molecules with graphene is vital for a wider scope of application and in the next section we investigate the interaction of a widely studied organic semiconductor, $F_{16}CuPc$, with CMG.

4.2 Organic thin films on CMG

Since graphene is a flexible, transparent electronic material, there has been a growing interest in integrating graphene with organic molecules to construct organic opto-electronic devices[58, 97, 131, 160] and organic thin film transistors.[100, 161] Recently, there have been a few reports on integrating graphene or CMG with organic molecules for opto-electronic devices[100, 102, 160] For example, GO was used as a hole transport layer in organic photovoltaic cells.[102] Additionally, graphene was used as a template for the growth of small molecule organic semiconductors (SMOS) to enhance the energy and charge transport properties.[162] Hence understanding the interaction of these molecules with graphene is important for successful fabrication of the devices.

As a benefit over inorganic semiconductors, SMOS provide the ease of forming thin films, cylinders, and clusters. In addition, SMOS provide low cost and flexible electronics; as a result, they are used in photovoltaics, LEDs and organic field effect transistors.[163, 164] Most molecular semiconductors are p-type. To convert them to n-type semiconductors requires modifications of the highest occupied molecular orbital, which makes them susceptible to oxidation and hence they are unstable in air. F_{16}CuPc was the first air stable, n-type, small molecule organic semiconductor to be discovered.[165] The charge transport properties of these molecules are highly dependent on the orientation of the molecules relative to the substrates[166, 167] and on the crystallography of the molecular material. Hence, determining the nanostructure and crystalline ordering of the molecule is important to better understand and utilise the charge transport properties.

To date, a number of studies on the structure of F_{16}CuPc have been done but no consensus has been reached on the lattice parameters or the type of crystal structure.[168-170] Although thin films have been used in the organic devices, most techniques for studying

crystallography require bulk films.[168] Moreover, the crystal structure of F_{16}CuPc thin films has been reported to change with thickness[170] and the film morphology also depends on the substrate.[171] Hence, it is important to understand the thickness dependence of the structure of F_{16}CuPc molecules to understand the charge transport properties. In this study the film thickness dependence of the structure of F_{16}CuPc on CMG was analysed using electron diffraction. The crystal structure, of bulk F_{16}CuPc[172] was determined by Dr. Dean Keeble and Dr. Richard Beanland (Department of Physics, University of Warwick) This structure was used to understand the structure and orientation of F_{16}CuPc on CMG. It was found that the molecules of F_{16}CuPc were nearly perpendicular to the surface of the CMG in the form of textured films. At low thicknesses the film showed some change in texture, however, no evidence for changes in the crystal structure with film thickness were observed.

4.2.1 Fabrication of F_{16}CuPc thin films on CMG.

All the growth of F_{16}CuPc was carried out by Luke Rochford from the Department of Chemistry, University of Warwick. For thin film growth of F_{16}CuPc a custom built multi chamber UHV system with base pressure better than 10^{-9} mbar was used. TEM substrates were prepared by drop-casting a GO suspension (0.2 $mgml^{-1}$) on carbon grids. For SEM and AFM, a GO suspension (1 $mgml^{-1}$) was spin coated on Si/SiO_2. Thin films of F_{16}CuPc (obtained from Sigma Aldrich and further purified before use) were simultaneously deposited on suspended and supported GO substrates on a specially designed substrate holder. Thin films of thicknesses ranging from 1 to 80 nm were deposited at a growth rate of 0.03 $Å s^{-1}$ at ambient temperature. The growth rate and final thickness were controlled by a quartz crystal microbalance (QCM) that was pre-calibrated ex-situ by AFM.

4.2.2 Structure of a single crystal $F_{16}CuPc$

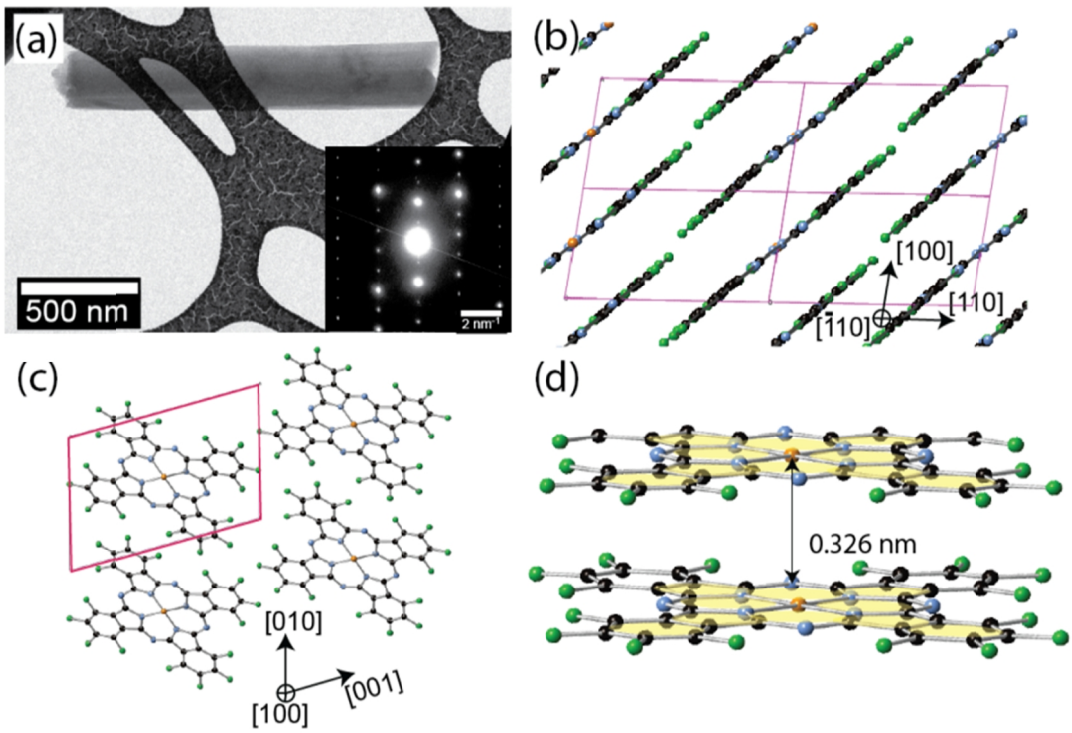

Figure 4.12 (a) A bright field TEM image showing a ribbon of $F_{16}CuPc$ on Au coated lacey grid. Inset $[0\bar{1}1]$ selected area diffraction pattern. Courtesy of Dr. Richard Beanland, Department of Physics, University of Warwick. (b) A $[0\bar{1}1]$ projection showing the molecule edges with the molecules lying in the plane $(\bar{1}22)$. (c) A $[100]$ projection showing the molecule in relation to the unit cell. Unit cells in (b) and (c) are shown in magenta. (d) Molecules laying in such a way that Cu atom in one molecule is aligned to the N atom in the other molecule. Colour code – C = black, N = blue, F = green and Cu = orange.

The bulk structure of $F_{16}CuPc$ was obtained by Dr. Dean Keeble (University of Warwick) by synchrotron XRD analysis of ribbon like crystals. $F_{16}CuPc$ was found to exhibit a triclinic crystal structure with one molecule per unit cell and the molecules stacked parallel to one another, unlike other copper phthalocyanines that exhibit a herringbone structure in the fibre. The observed triclinic structure with space group $P\bar{1}$, had the lattice

parameters a = 0.489(2) nm, b = 1.029(4) nm, c = 1.491(7), α = 74.24(12) °, β = 87.22(10) ° and γ = 80.80(13) °.[172]

Figure 4.12a shows an F_{16}CuPc ribbon similar to those used to obtain the synchrotron XRD data to solve the structure. The F_{16}CuPc fibre was placed on a gold coated lacey grid. The SAED pattern is shown in the inset. These fibres grow in the $[0\bar{1}1]$ direction; a schematic of the molecules in the crystal viewed from $[0\bar{1}1]$ projection is shown in *Figure 4.12b*. The plane of the molecule is $(\bar{1}22)$. *Figure 4.12c* shows the orientation of the molecule with respect to the unit cell. *Figure 4.12d* shows the packing of these molecules is such that the central copper atom in the molecule is in line with the adjoining molecule's nitrogen atom and the intermolecular distance is between the copper (of the first molecule) and the nitrogen (of the second molecule) is 0.326 nm.

4.2.3 Analysis of the thin film structure of F_{16}CuPc

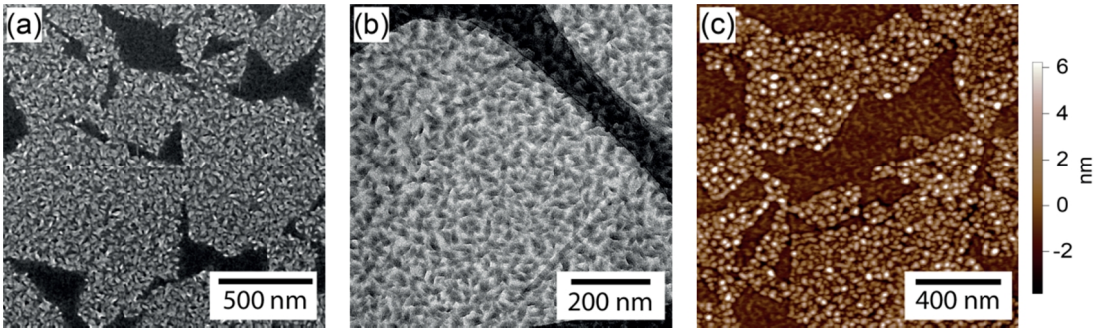

Figure 4.13 F_{16}CuPc of θ = 10 nm deposited on GO as viewed in (a) SEM and (b) TEM. (c) AFM image of F_{16}CuPc on GO of θ = 5 nm. In the AFM and SEM images GO is supported on Si/SiO_2 which is visible as a dark background while for TEM GO is suspended on the lacey grid. AFM image courtesy of Luke Rochford, Department of Chemistry, University of Warwick.

Figures 4.13a and b show SEM and TEM images of F_{16}CuPc film deposited on GO for θ = 10 nm and *Figure 4.13c* shows an AFM image of F_{16}CuPc film deposited on GO for θ

= 5 nm. In the SEM and AFM images the lighter areas are the GO covered with F_{16}CuPc film. In TEM the brighter grainy structure is F_{16}CuPc film on GO.

F_{16}CuPc forms a three-dimensional island structure on GO. The width of these islands as measured from SEM images was between 10 and 20 nm. Using the AFM images for θ = 5 nm the heights of the islands was measured to be ~ 9 nm. The TEM image also shows the granular structure of a F_{16}CuPc film deposited on GO. The diffraction contrast from individual grains indicates that these form crystalline domains. The width of the grains in the TEM image was consistent with the AFM and SEM measurements. However, the diffraction contrast disappears after a longer exposure as F_{16}CuPc is sensitive to the electron beam. As a result HR-TEM could not be used to determine the structure.

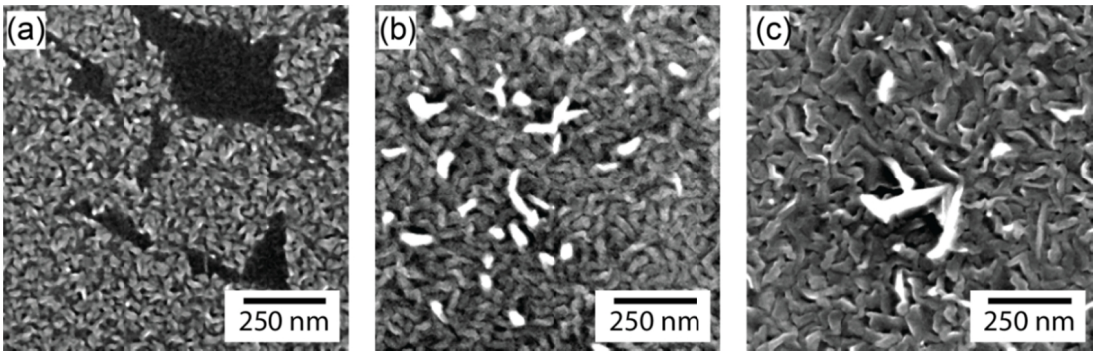

Figure 4.14 SEM images of F_{16}CuPc on GO for nominal thickness θ as (a) 10, (b) 30 and (c) 80 nm.

The SEM images in *Figure 4.14a, b and c* show F16CuPc films on GO with θ = 10, 30 and 80 nm. As the thickness of the film was increased the film morphology changed. As shown here the islands grew into nanowires and fibres with increasing film thickness. Similar changes in morphology have been reported for F_{16}CuPc growth on indium tin oxide.[173]

Since F_{16}CuPc molecules are sensitive to beam damage, electron diffraction was used for detailed analysis of the film morphology on GO rather than HR-TEM. *Figure 4.15a* is the inverted SAED pattern of F_{16}CuPc film (θ = 5 nm) on GO.

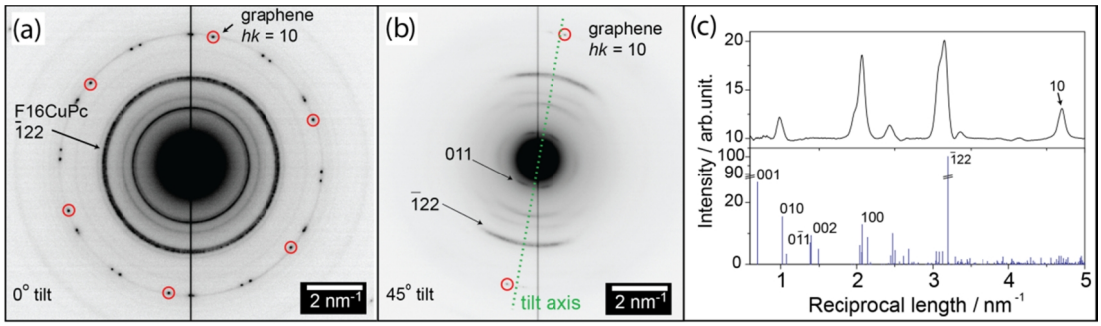

Figure 4.15 Inverted SAED pattern from θ=5 nm F_{16}CuPc deposited on GO coated lacey grid with (a) sample tilted by 0° and (b) sample tilted by 45°. (c) Top is rotationally averaged intensity plot of the SAED pattern in (a) and bottom is the predicted intensity plot for randomly oriented polycrystalline F_{16}CuPc.

The GO sheet here consists of 4 layers as identified by 4 hexagonal set of spots, one set of spots is marked in red circles. The concentric rings are from F_{16}CuPc indicating the polycrystalline nature and random orientations in the direction perpendicular to the direction of electron beam. *Figure 4.15b* shows the pattern obtained by tilting the sample by 45° about the tilt axis (shown in dotted green line). As expected the GO diffraction spots away from the tilt axis disappear, the remaining spots close to the tilt axis are marked in red. Strikingly, the rings from F_{16}CuPc have turned into discontinuous arcs. *Figure 4.15c* shows intensity plot of the rotational average of the pattern in *Figure 4.15a* calibrated using GO 10 (top) and, using the bulk F_{16}CuPc lattice structure, a predicted intensity plot for randomly oriented F_{16}CuPc crystallites (bottom).

Comparing the diffraction peaks in the rotationally averaged plot (*Figure 4.15c*, top) with the predicted peaks for randomly oriented crystals (*Figure 4.15c*, bottom) we find that the peak positions are in good agreement; but, some of the intensities in the averaged plot are higher than that in the predicted plot while some other intensities are quite low or completely absent. The most intense peak in both of the plots corresponds to $\bar{1}22$ i.e., the intermolecular spacing. In herringbone structures the intermolecular spacing

does not necessarily correspond to a lattice plane in the crystal; although a lattice plane close to the molecular plane would produce a higher intensity due to the increased structure factor, the lattice plane corresponding to the intermolecular spacing will always produce the strongest intensity. Since all of the deposited samples showed SAED's with $\bar{1}22$ as the most intense peak, this is consistent with the bulk structure analysis that the planar F_{16}CuPc molecules exhibit parallel stacking in the crystal.

The SAED pattern obtained after tilting the sample by 45° shows discontinuous arcs and other diffraction arcs appear perpendicular to the tilt axis. This indicates that the crystallites are not randomly oriented on the substrate but there exists a fibre texture i.e., a preferential orientation perpendicular to the substrate plane but random orientations in the plane. As visible in the pattern in *Figure 4.15b,* the diffractions $\bar{1}22$ and 011 split into a pair of arcs equidistant from the tilt axis, indicating that the axis of the texture is along the direction of intersection of these planes which is $[01\bar{1}]$. This is perpendicular to $(\bar{1}22)$ intermolecular plane, indicating the molecules are lying perpendicular to the GO sheet.

4.2.4 Thickness dependent morphology of thin-film $F_{16}CuPc$

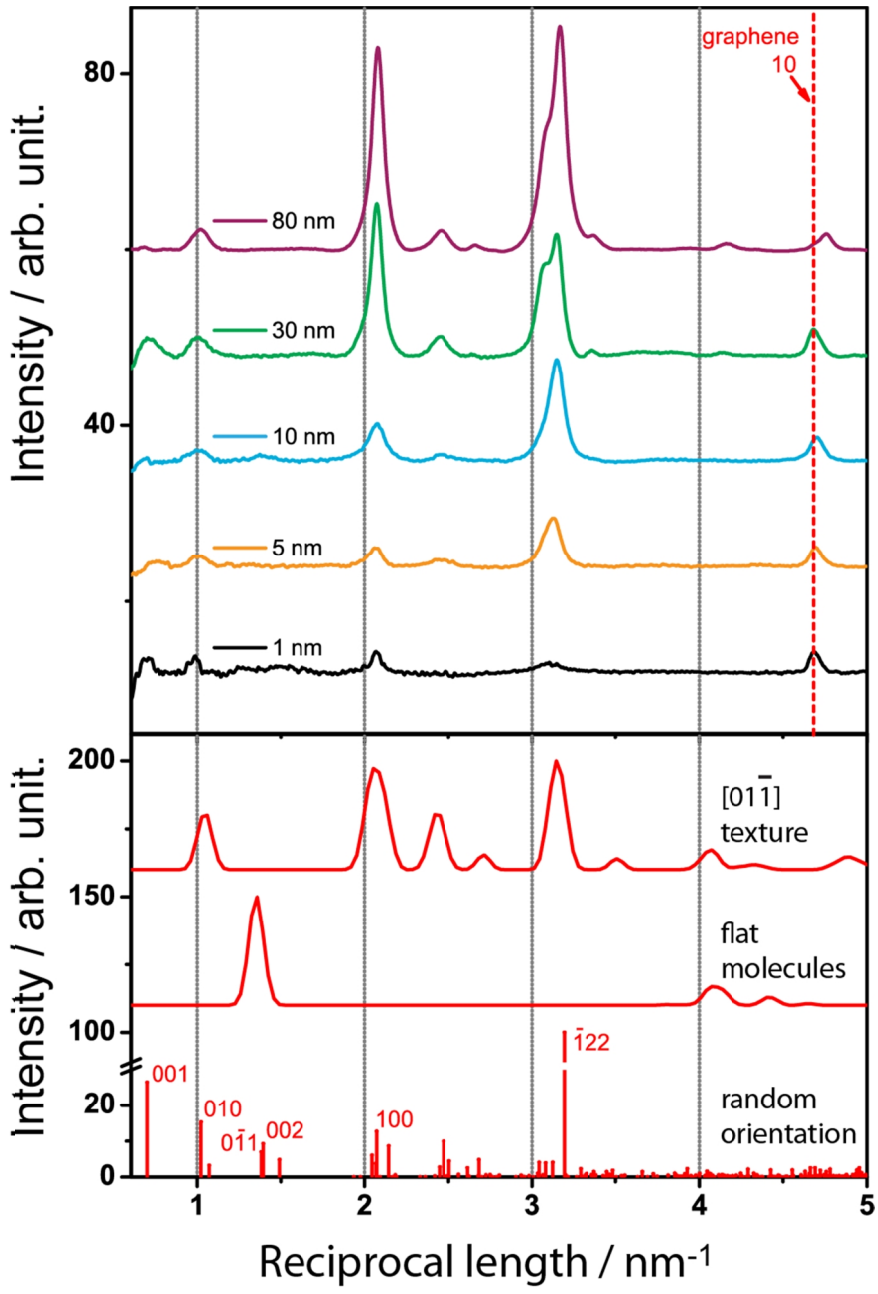

Figure 4.16 Top – Rotationally averaged intensity plot from the SAED patterns of $F_{16}CuPc$ deposited on GO for θ between 1 to 80 nm. Bottom – Kinematical simulations for thin film of $F_{16}CuPc$ with $[01\bar{1}]$ fibre texture, flat molecules and randomly oriented molecules.

Using SAED patterns the structure of $F_{16}CuPc$ was analysed with changing film thicknesses. *Figure 4.16* shows the rotational average of the SAED patterns of $F_{16}CuPc$ films

on GO with nominal thicknesses θ from 1 to 80 nm. The kinematically simulated intensity plots for randomly oriented molecules, molecules lying flat on the GO surface and with fibre texture along $[01\bar{1}]$ are shown at the bottom in the red curves.

Although the relative intensities change, it is clearly visible that for all the film thicknesses, including 1 nm, the major peaks do stay in roughly the same positions, implying that at all the thicknesses neither the intermolecular distances nor the crystal structure in the film changes significantly. The observed peak positions closely match the kinematically simulated plot (assuming single electron scattering) for the textured film. However, in most of the films additional peaks at 001 and $01\bar{1}$ (or 002) are visible, suggesting that these films are a mixture of random orientation and $[01\bar{1}]$ fibre texture. The intensity of the $\bar{1}22$ peak in the film with θ = 1 nm is relatively low suggesting a greater amount of crystallites with molecules not lying perpendicular to GO. The model with flat molecules on GO does not fit to any of the data. The mixture in the thinnest film consists of a greater amount of random orientation along with the $[01\bar{1}]$ fibre texture. Thus an evolution of the texture is seen from random to oriented crystallites with increasing film thickness. Additionally, a small change in the relative orientation of the F_{16}CuPc significantly changes the diffraction pattern. As a result, accurately determining the changes in crystal structure with a single diffraction pattern is not possible. From the diffraction patterns obtained by tilting the sample by different angles relative to the electron beam more information about the structure can be obtained.

In a recent report on growth of F_{16}CuPc on epitaxial graphene, molecules were found to lie flat on graphene in ordered stripes and it was credited to the π–stacking between the planar F_{16}CuPc molecules and delocalised π electrons in graphene.[162] However, the sheet of GO is randomly functionalised with oxygen groups along with

inherent adsorbates like oxidative debris. Hence, the interaction between hydrogen from hydroxyl groups on GO and fluorine from $F_{16}CuPc$ is more likely than the $\pi - \pi$ interaction, driving the perpendicular orientation of the molecules on GO. Additionally, since the oxygen functionalities in GO are random the orientation of the molecule is perpendicular yet random. This is consistent with the observation of the change in orientation of pentacene molecules from perpendicular to flat on clean graphene and graphene with residual polymer.[75]

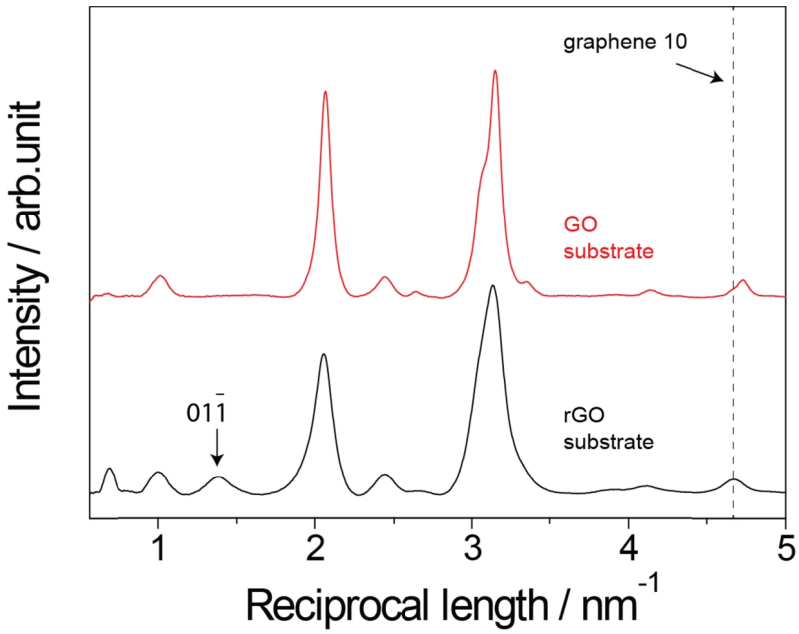

Figure 4.17 Rotationally averaged intensity plot from SAED of $F_{16}CuPc$ deposited on GO (red) and rGO (black) for θ = 80 nm.

$F_{16}CuPc$ was deposited on rGO coated lacy grid and the SAED patterns of $F_{16}CuPc$ on rGO were analysed and plotted as shown in *Figure 4.17*. The $01\bar{1}$ peak is well-defined in the case of $F_{16}CuPc$ on rGO and the intensity is comparable to the other peaks. While the morphology has not changed significantly, changing the functionality of GO has stimulated some molecules to lie flat on the rGO.

4.2.5 Conclusion on the study of F_{16}CuPc thin films on graphene

While F_{16}CuPc molecules can form a variety of structures such as thin films, fibres, etc. the molecular orientation is important for determining charge transport properties. The growth morphology and orientation of F_{16}CuPc thin films on CMG was investigated using a combination of microscopy techniques. CMG provided a low background and well defined diffraction pattern for in situ calibration of F_{16}CuPc diffraction patterns and the calibrated diffraction patterns were analysed using the bulk crystal structure obtained from the synchrotron X-ray analysis.[172] The bulk structure of the crystal was retained even in nm thin films. Analysis of the diffraction patterns of the sample tilted at different angles to the incident electron beam enabled investigation of the orientation of the crystallites. A fibre texture with the axis of texture along $[01\bar{1}]$ and molecules lying perpendicular to the CMG sheet was found. Thin films ranging from a monolayer to 80 nm were deposited on GO and no evidence of changes in the crystal structure with film thickness were found. Although the texture direction was identical in all the films there was evidence of a mixture of random orientations and fibre texture in the lowest thickness film. These results show that it is possible to extract the crystallography of molecular thin films down to nominally monolayer coverages, and suggest that it is also possible to adjust the orientation by changing the functionalization of graphene.

4.3 Conclusions

For wider device applications of CMG sheets, their combination with metal and organic material is essential, and, being an excellent TEM support, CMG sheets offer in situ characterisation of these combined structures in TEM. CMG sheets have shown low background and proved to be a highly transparent substrate for the study of nanoparticles

and small molecules in TEM. In addition, TEM with an appropriate support film allows acquisition of quantitative data required for statistical analysis. The interaction of metals and organic thin films with CMG sheets was investigated using a combination of microscopic techniques, mainly TEM.

The investigations of $F_{16}CuPc$ thin films of various thicknesses on GO have revealed fibre texture growth with molecules lying perpendicular to the sheet of GO. The thinnest film showed a mixture of random and textured growth, but the crystal structure of the films remained the same across the range of thicknesses studied here. In the case of metal-CMG, the role of the diffusion barrier and relative bulk cohesive to adsorption energy in the formation of final morphology was investigated. It was found that the final morphology of a metal on CMG in terms of particle size and density was governed by the metal-CMG interaction and also depended on the number of CMG layers. The study on the growth of metal-on-GO suggests that a fine control over the morphology of metal particles on CMG can be obtained. This enables simple and structured fabrication of a variety of devices for e.g., sensors. In the next chapter the fabrication and working of Pd-rGO/graphene hydrogen gas sensors is presented.

Chapter 5. **Hydrogen sensor**

5.1. Introduction

Graphene, an all surface material with excellent conductivity and low electrical noise, has shown to be an outstanding material for sensors.[174] However, mechanically exfoliated graphene is not a practical source for large scale production; a low cost alternative material is rGO. Effective chemical sensors made by directly spin coating rGO from hydrazine dispersions have been shown to be able to detect chemical agents such as nitrogen dioxide, ammonia and dinitrotoluene in parts per billion, with noise levels significantly lower than carbon nanotube based sensors.[133] The basic mechanism behind sensing is detection of the change in conductivity of graphene due to the change in carrier concentration induced by molecular adsorption and desorption. However, many different molecular species can adsorb onto graphene, inducing a varying degree and type of doping; as a result graphene on its own does not give a selective response and hence is not

likely to find practical applications.[175] Instead graphene can be coated with thin films or nanoparticles that could show selective adsorption, with the electrical readout coming from the induced change in the conductivity of the underlying graphene. In this work, Pd coated rGO and graphene devices are shown to be highly selective and sensitive hydrogen gas sensors.

Demand for clean energy source is ever increasing and hydrogen, as an energy carrier, is one of the potential solutions for cutting down the carbon emission. However, safe usage is crucial as hydrogen is an odourless and flammable gas. The lower explosive limit for hydrogen gas is 4 %.[176] Pd can dissolve large amounts of hydrogen atoms resulting in changes in its work function; hence hydrogen gas sensors incorporating the Pd gate devices (Pd metal-insulator-semiconductor, MIS devices) have been studied since the mid-1970s.[177-179] Currently, the commercially available hydrogen sensors either have limitations such as cross sensitivity with CO, instability above 50 °C* or they are expensive.† Hence there is need for a low cost, selective sensor that can be manufactured at a large scale. More recently, there have been a few reports on Pt-rGO /graphene hydrogen sensors[14, 82, 180, 181] but, these require either a high temperature[181] or high concentration of hydrogen (4% or 4000 parts per million).[82] In a recent report room temperature response to H_2 was only observed on electrochemically deposited Pt on holey rGO and not on rGO devices.[14] In a comparative study of Pd and Pt as a gate metal in metal-oxide-semiconductor (MOS) capacitor sensors Armgarth et al. have shown that Pd gated devices are superior in terms of hydrogen detection at low concentrations in air.[182] Accordingly, Pd functionalised

* https://www.citytech.com/PDF-Datasheets/3hye.pdf
http://www.figaro.co.jp/en/pdf/FCM6812ProductInfo1006.pdf

† https://www.fuelcellmaterials.com/site/index.php?option=com_virtuemart&Itemid=28

multilayer graphene nanoribbon networks have been shown to exhibit a detection limit of 40 parts per million (ppm) for H_2 at room temperature.[183] Although there have been a few reports on hydrogen gas sensors incorporating Pd as catalysts on graphene,[150, 183, 184] there exists no comprehensive picture of the mechanism of charge conduction and response kinetics of the device.

In this chapter the fabrication and working of Pd–rGO based hydrogen gas sensors is studied. The devices were tested for varying H_2 concentration, temperature, humidity and cross sensitivity, in addition to device fabrication parameters such as rGO and Pd thicknesses. Significant increase in the sensitivity was observed with increasing hydrogen concentration, temperature and humidity. The devices without coatings (bare rGO) or with Au coating showed no response to hydrogen. Addtionally, Pd-doped rGO devices did not respond to carbon monoxide, ethanol, or toluene. For a comparative study, Pd-doped graphene devices were also tested and showed similar response to hydrogen.

5.2. Device fabrication and testing

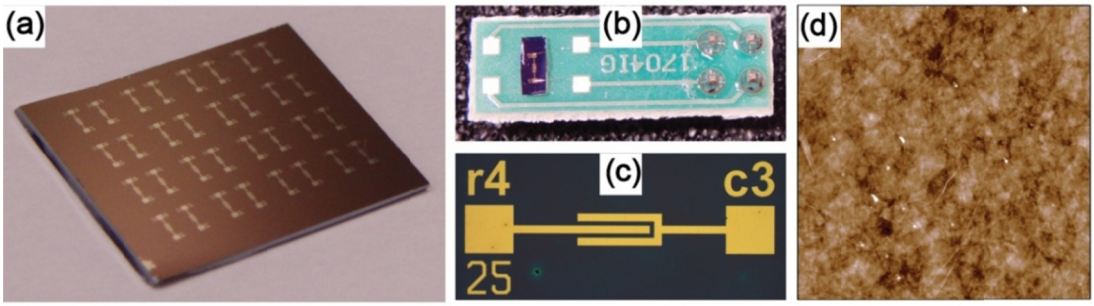

Figure 5.1 Photograph of a (a) sensor substrate showing an array of devices, and (b) single device mounted on a printed circuit board. (c) Optical image of a device. (d) 5 µm square AFM image of the Pd-rGO film (full height scale is 8 nm). Sensor substrates fabricated by Dr. Neil Wilson, Department of Physics, University of Warwick.

A homogenous suspension of GO was spin coated on Si/SiO_2 substrates with a predefined array of gold interdigitated electrodes, as shown in *Figure 5.1a.* Since the as-produced GO is an insulator, GO-on-substrate was reduced to rGO by exposing to hydrazine vapour followed by a low temperature annealing for 1 h at 300 °C as described in Chapter 2. The sample substrates were then cleaved to separate individual devices, followed by sputter coating with Pd and wire bonding onto a printed circuit board (PCB) (*Figure 5.1b*). This produced 32 similarly prepared devices from each initial chip to enable comparative studies. *Figure 5.1c* shows an optical microscope image of one such device with channel length 1 mm and width 25 μm. The AFM image (*Figure 5.1d*) is from a sample made with GO suspension of concentration 5 mg ml^{-1}. The image shows that these films are continuous and homogeneous. Analysis of several such thin films by AFM showed a roughness of 0.5 ± 0.2 nm, and thickness of 2.9 ± 0.5 nm equivalents to roughly 5 layers of rGO. Fine control over the thickness of rGO films was readily achieved by spin coating various concentrations of GO on the substrate as discussed in Chapter 2. The morphology of the Pd-on-rGO was discontinuous and branched island-like, as shown in Chapter 4.

Hydrogen gas sensors incorporating CVD grown graphene were fabricated in a similar fashion, except the deposition of graphene on the substrate. As the transfer of a continuous layer of graphene from copper to substrate was not yet fully optimised, a double transfer of graphene was utilised to obtain a continuous layer. In a double transfer method another layer of graphene was transferred onto a substrate pre-coated with graphene through the procedure described in Chapter 2. The samples were then cleaved into individual devices and sputter coated with Pd before being mounted on the PCBs.

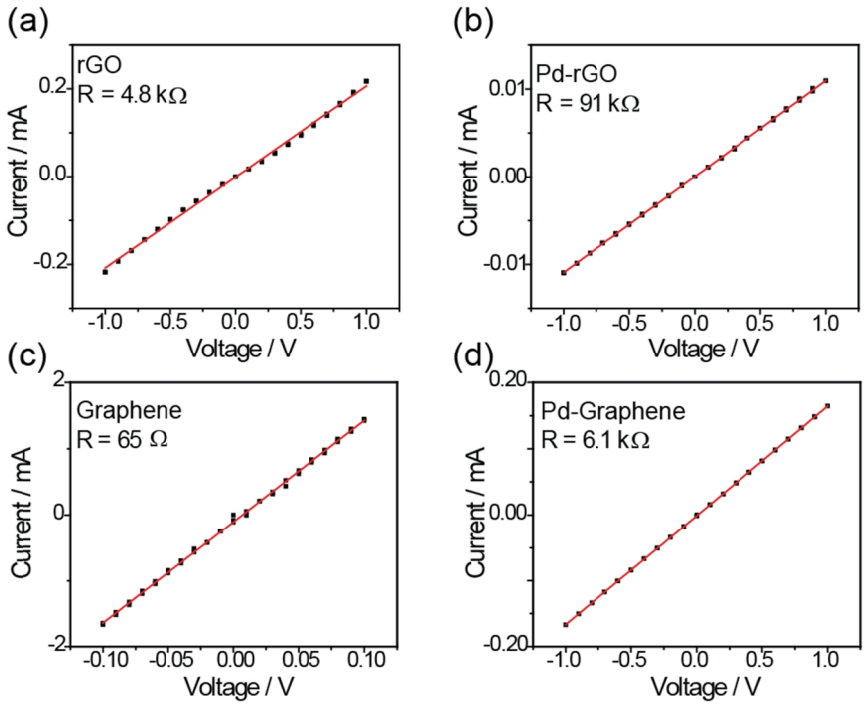

Figure 5.2 Current versus voltage for (a) rGO, (b) Pd-rGO, (c) graphene and (d) Pd-graphene devices.

A basic electrical characterisation was performed on these devices. *Figures 5.2a and b* show representative I-V measurements performed at room temperature on bare rGO and Pd-rGO devices. The Ohmic response with resistances 4.8 kΩ and 91 kΩ (corresponding to sheet resistances of 192 and 3640 kΩ/sq.) for bare rGO and Pd-rGO suggests that the charge conduction is still through rGO and not Pd. This is also true for graphene and Pd coated graphene devices with sheet resistances of 2.6 and 244 kΩ/sq. respectively (*Figures 5.2c and d*).

Here, when rGO or graphene were sputter coated with Pd nanoparticles their resistance increased; since the work function of Pd (5.3 eV)[185] is higher than that of rGO (4.2 eV)[156] the resistivity is expected to decrease, as rGO devices are p-type.[68] Hence this significant increase in resistivity is attributed to the random scattering centres introduced by plasma assisted Pd coating, as was previously observed for graphene with DC plasma coated Ag.[93]

Sensor testing station

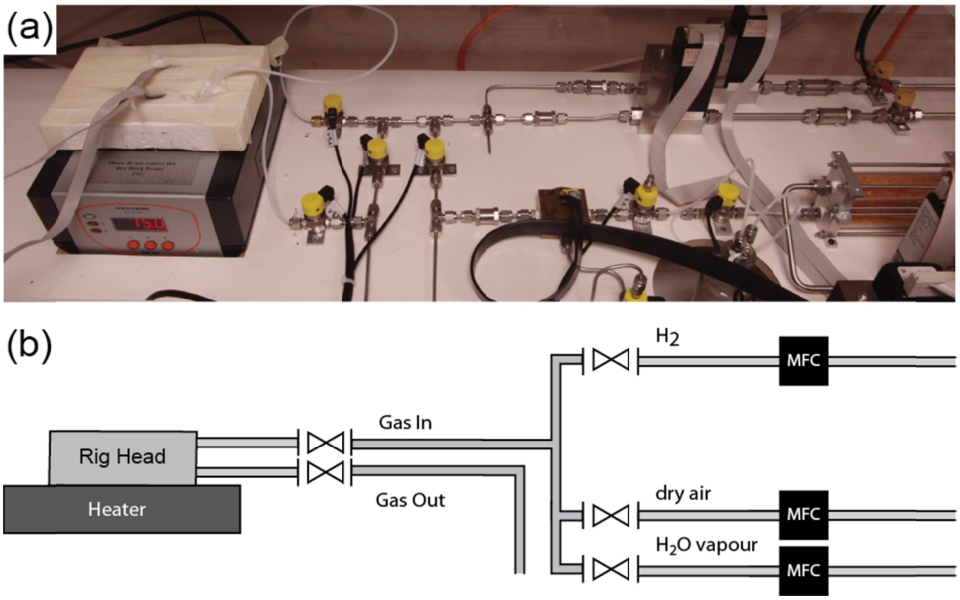

Figure 5.3 (a) Photograph and (b) schematic of the sensor testing station showing the valves and the mass flow controllers (MFC) enabling controlled testing of analytes.

Figure 5.3a and b show a photograph, and schematic respectively, of the sensor testing station. The sensor testing station was developed by Dr. Covington from the School of Engineering, University of Warwick and full details can be found in Covington et al.[186] In brief, the testing station involved an automated flow system with a custom made sensor chamber and a gas rig controlled by National Instruments™ LabVIEW software. The gas rig, consisting of the valves and mass flow controllers (MFCs) allowed mixing of an analyte with two air lines, one saturated with water vapour and the other with dry air. This facilitated the evaluation of exact concentrations of an analyte at a specified humidity, over 16 sensors at the same time.

The sensor devices were placed in the sensor chamber which was placed onto a DRI-BLOCK™ heater and left at the required temperature for a period of 2 to 5 h to equilibrate. The devices were then operated at a constant current of 0.1, 1, 10, or 100 µA depending upon their initial resistances, and the voltage dropped across each device was

measured. For the hydrogen gas testing 6 different concentrations 200, 360, 600, 1100, 1900, 3300 ppm were evaluated in dry/humid air at temperatures of 30, 50, and 75 °C (± 0.1 °C). During operation the devices were exposed to pulses of hydrogen at the predefined concentration for 1200 s (designated as exposure time). In between the pulses, dry or humid, air was flown for 1800 s (designated as relaxation time).

5.3. Sensitivity to hydrogen

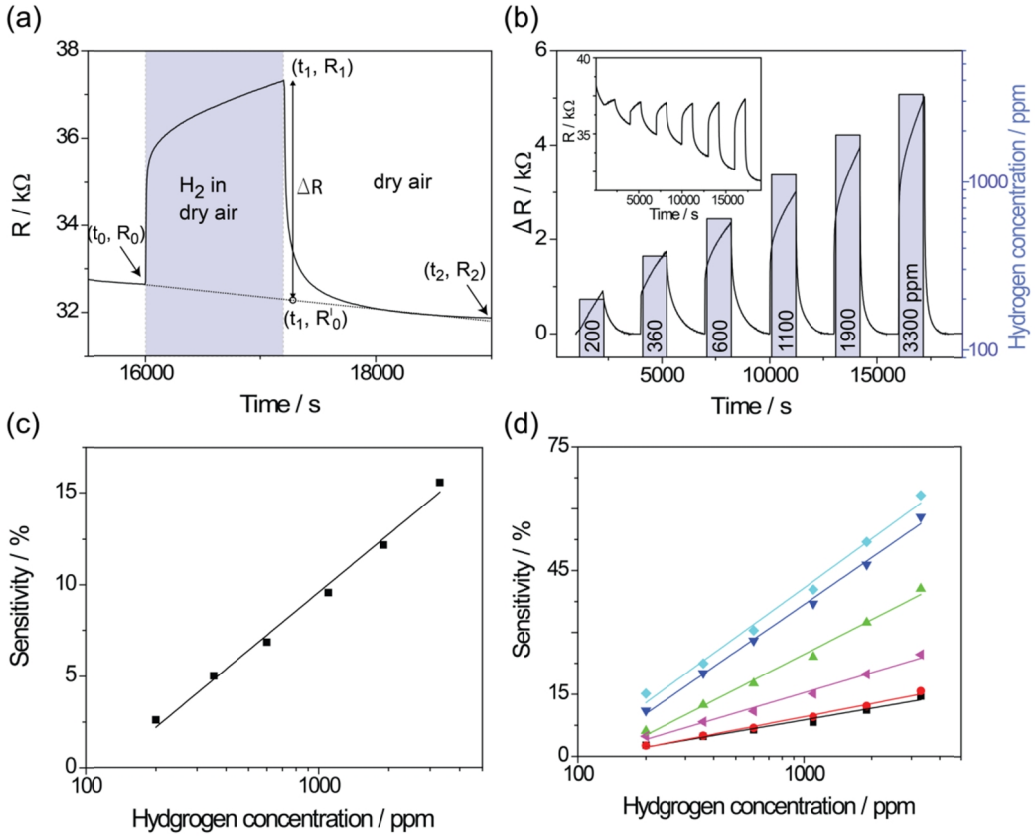

Figure 5.4 Resistance response of Pd-rGO device to (a) 3300 ppm hydrogen gas in dry air at 75 °C, (shaded column represents the time of flow of H_2 in dry air) (b) different concentrations of hydrogen gas with flow of H_2 (inset shows raw data for H_2 response). (c) Sensitivity as a function of hydrogen concentration with a logarithmic fit (solid line) for the data in (b). (d) Sensitivity as a function of hydrogen concentration with fits (coloured solid lines) for 6 similarly prepared devices.

Figure 5.4 shows data obtained from a device consisting of 2 nm rGO, i.e. roughly 4 layers of rGO (GO suspension concentration 4 mg ml^{-1}), coated with ~1 nm Pd and measured at 75 °C with dry air as the carrier gas. When the device was exposed to a flow of 3300 ppm of hydrogen gas, a prompt increase in the resistance is observed, followed by a slower response (*Figure 5.4a*). After the flow was stopped the resistance decreased towards a baseline value, R_2. For the flow of H_2, shown in the shaded column, the exposure time between t_0 and t_1 is 1200 s and the relaxation time between t_1 and t_3 is 1800 s. The background of each response pulse was subtracted by fitting a straight line between times (R_0, t_0) and (R_3, t_3) and then the change in resistance ΔR for each response was obtained as $\Delta R = R_1 - R_0'$. The sensitivity of a sensor is then defined by:

$$\text{Sensitivity} = \frac{\Delta R}{R_2}\% \qquad (5.1)$$

Figure 5.4b shows the background subtracted response of the same device to different hydrogen concentrations [H_2] (200, 300, 600, 1100, 1900, 3300 ppm) in dry air; raw data is shown in the inset. Evidently, with increasing hydrogen concentration the resistance of the device increases monotonically. The plot of the sensitivity as a function of hydrogen concentration on a logarithmic scale, *Figure 5.4c*, shows a linear trend. This isotherm plot is well fitted by an equation of the form:

$$\text{Sensitivity} = a\ln[H_2] + b \qquad (5.2)$$

where a is slope and b is a constant. *Figure 5.4d* shows the sensitivity as a function of H_2 concentration for 6 similarly prepared devices operated at the same time. Using *Equation (5.2)* for the set of data in *Figure 5.4d,* the values of H_2 concentration at which the sensitivities are zero are between 90 and 130 ppm. These values are far less than the lower explosive limit of H_2 gas in air, which is 4000 ppm. We see that although all the devices show a logarithmic dependence of sensitivity on H_2 concentration the fit parameters vary

significantly; the sensitivities for 3300 ppm H_2 in 6 similarly prepared Pd-rGO devices ranged from 15 to 65 %.

The hydrogen sensing mechanism in Pd coated devices is due to the change in the work function of Pd upon hydrogen exposure.[177, 187, 188] The H_2 molecules get adsorbed on the Pd surface and dissociate to form atomic hydrogen lowering the Pd work function. For these rGO sensors some of the dissociated hydrogen atoms move to the interface between Pd and rGO to form a dipole layer, resulting in an effective electron transfer from Pd to rGO. This charge transfer changes the carrier concentration in the rGO and hence its resistance. The change in work function is detected as a change in the voltage dropped across the device when operated at constant current.

For desorption it is also well known that in the presence of oxygen, dissociated hydrogen atoms combine with oxygen to form H_2O molecules and desorb.[189] The reactions that take place during the adsorption and desorption of hydrogen can be written as follows:[179]

Adsorption $$H_2 \underset{d1}{\overset{c1}{\rightleftharpoons}} 2[H] \quad (5.3)$$

Desorption $$O_2 + 2[H] \underset{d2}{\overset{c2}{\rightleftharpoons}} 2[OH] \quad (5.4)$$

$$[OH] + [H] \underset{d3}{\overset{c3}{\rightleftharpoons}} H_2O \quad (5.5)$$

where *c1, c2, c3* and *d1, d2, d3* are the respective forward and reverse reaction rate constants. Thus, the hydrogen adsorption on these devices is a dissociative chemisorption process.

From the plot of sensitivity it is clear that the change in device resistance is logarithmically dependent on H_2 concentration. A logarithmic dependence of Pd work

function on hydrogen concentration has been observed for hydrogen adsorbed at Pd-SiO_2 interfaces.[187, 190] It has been found that the change in Pd work function depends logarithmically on hydrogen pressure indicating that the hydrogen heat of adsorption at the interface varies linearly with H_2 concentration resulting in a Temkin type isotherm; this behaviour has been suggested to be due to an increasing electrostatic interaction between the dipoles at the interface with increasing H_2 concentration.[187, 189] The Temkin isotherm is valid when the number of active sites at the interface is not the limiting factor for adsorption of the molecules. In the range of H_2 concentration studied here the isotherm plots, *Figure 5.4c* and *d,* are consistent with the Temkin isotherm indicating that the interface coverage is between low to intermediate.

The change in Pd work function changes the graphene carrier concentration and hence the resistance of the device. In graphene the conductivity away from the Dirac point varies roughly linearly with gate voltage[37, 44] and the conductivity σ is related to mobility μ and carrier concentration *n* in the following way

$$\sigma = ne\mu \tag{5.6}$$

where *e* is the electron charge. Thus, away from the Dirac point the device conductivity will change linearly with the Pd work function, assuming that the change in carrier concentration is linearly dependent on the change in work function (i.e. it acts like a gate electrode).

The individual devices of the same type show a wide range of sensitivity values, which could be due to a number of factors, such as the adsorbed species, film thickness, size of rGO platelets, and defects introduced in rGO film during sputter coating of Pd. These factors result in difference in the carrier concentration and mobility and hence the conductivity in individual devices.

5.3.1. Desorption time in Pd-rGO devices

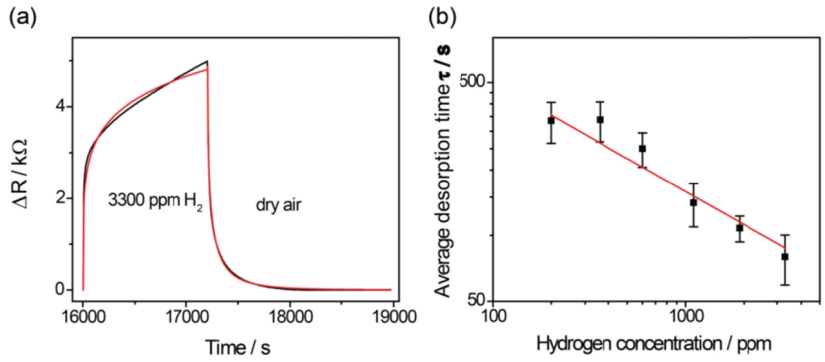

Figure 5.5 (a) Stretched exponential fit (red) to 3300 ppm hydrogen response pulse (black) and (b) average desorption time as a function of hydrogen concentration.

The change in resistance with time after the flow of H_2 pulse, i.e. during desorption, is not fitted by a simple exponential function. Instead, to extract the average desorption time a stretched exponential was fit to each part of the response pulse (adsorption and desorption) separately. The stretched exponential fit is given by

$$\Delta R = R_2 e^{-(t/\tau_k)^{\beta}} \tag{5.7}$$

where β varies between 0 and 1 and τ_k is the time constant and R_2 is baseline value. The average time constant is given by

$$\langle \tau \rangle = \int_0^{\infty} dt e^{-(t/\tau_k)^{\beta}} = \frac{\tau_k}{\beta} \Gamma\left(\frac{1}{\beta}\right) \tag{5.8}$$

where Γ is the gamma function. For β = 1, $\langle \tau \rangle = \tau_k$ i.e. an exponential decay. Thus a stretched exponential is a generalisation of the exponential function and is a slower function of time than exp-(t/τ_k). The physical origin of a stretched exponential for desorption/relaxation of a system is attributed to the broad distribution of active sites[191] consistent with the Temkin isotherm.

Figure 5.5a shows a stretched exponential fit (red) to a 3300 ppm hydrogen pulse response (same devices and operating conditions as for *Figure 5*.4). *Figure 5.5b* shows a plot of the average time constant for desorption as a function of hydrogen concentration averaged over 4 different devices operated at 75 °C. The fit equation used is

$$\ln(\tau) = m\ln[H_2] + c \qquad (5.9)$$

where c is a constant. The slope m was set to -0.5 and it fits reasonably well. With increasing H_2 concentration the desorption time decreases from 340 ± 70 s for 200 ppm of H_2 to 80 ± 20 s for 3300 ppm of H_2. At higher concentrations of hydrogen the energy barrier for desorption is smaller hence a faster desorption. The adsorption curve could not be fitted well, as is apparent in *Figure 5.5a* and hence the time constant was not extracted for the adsorption part of the response pulse.

5.3.2. Temkin isotherm or simple second order reaction mechanism

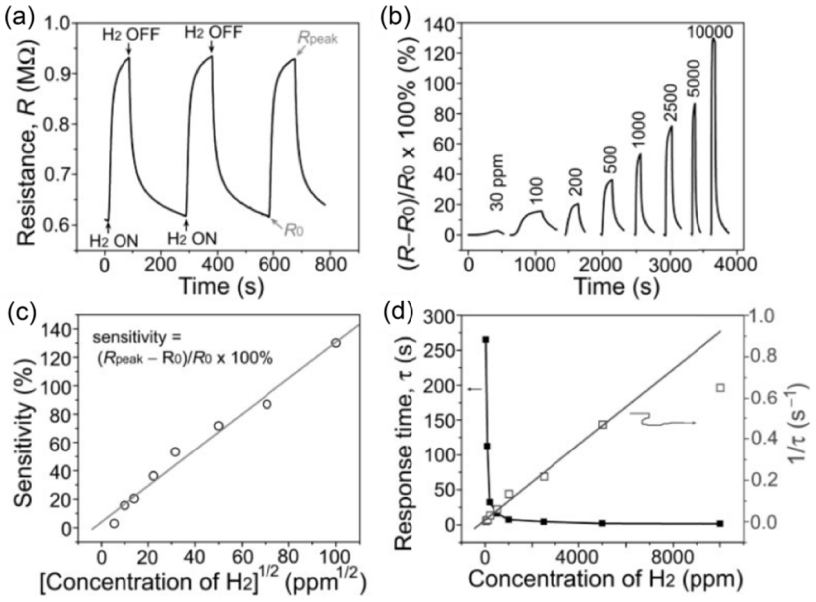

Figure 5.6 Hydrogen sensing response of a Pd coated carbon nanotube sensor (a) Resistance change upon flow of hydrogen in air. (b) Response to different concentrations of hydrogen gas. (c) Sensitivity as a function of square root of hydrogen concentration. (d) Response time as a function of hydrogen concentration. Reproduced from ref.[192]

Hydrogen dissociation by Pd has been considered as a second order reaction in a few reports. *Figure 5.6* is reproduced from a report by Sun et. al.[192] *Figure 5.6a and b* show the response of a Pd-CNT sensor to the flow of hydrogen gas in air. *Figure 5.6c* is the sensitivity dependence of the device plotted against the square root of hydrogen concentration. A linear relationship has been considered in this case. *Figure 5.6d* is the relation between response time and hydrogen concentration.

The linear relationship between sensitivity and square root of hydrogen has been attributed to the Langmuir isotherm theory for dissociative adsorption of gases. Sun et al. have suggested that hydrogen adsorption changes the Pd work function which might be proportional to the fractional coverage of hydrogen (ϕ) on the surface and linearly affects the effective charge concentration in the nanotube film. Hence the resistance change, $\Delta R/R_0$, is proportional to ϕ. The suggested reaction for hydrogen dissociation on the Pd surface is –

$$H_2 + 2S_{Pd} \rightarrow 2HS_{Pd}$$

where S_{Pd} are available Pd surface sites and are suggested to be proportional to 1 - ϕ. According to Langmuir isotherm,[192] at equilibrium the desorption rate equals adsorption rate such that,

$$\kappa_1 p(1-\phi)^2 = \kappa_{-1}\phi^2$$

or

$$\phi/(1-\phi) = (\kappa_1/\kappa_{-1})^{1/2}\, p^{1/2} \qquad (5.10)$$

where κ and κ_{-1} are the adsorption and desorption constants and p is the hydrogen partial pressure. Using equation 5.10, at low coverage of hydrogen ($\phi << 1$), the resistance change is given by

$$\Delta R / R_0 \propto \phi \approx (\kappa_1/\kappa_{-1})^{1/2}\, p^{1/2} \qquad (5.11)$$

where ϕ is hydrogen coverage, ΔR is the change in resistance upon hydrogen adsorption and R_0 is the base resistance. Using the Langmuir isotherm, the rate of hydrogen adsorption is $r = \kappa_1 p(1-\phi)^2$ and for low hydrogen coverages ($\phi << 1$), $r = \kappa_1 p$. Thus, a linear relationship between the response rate ($1/\tau$) and H_2 partial pressure is suggested in that paper.

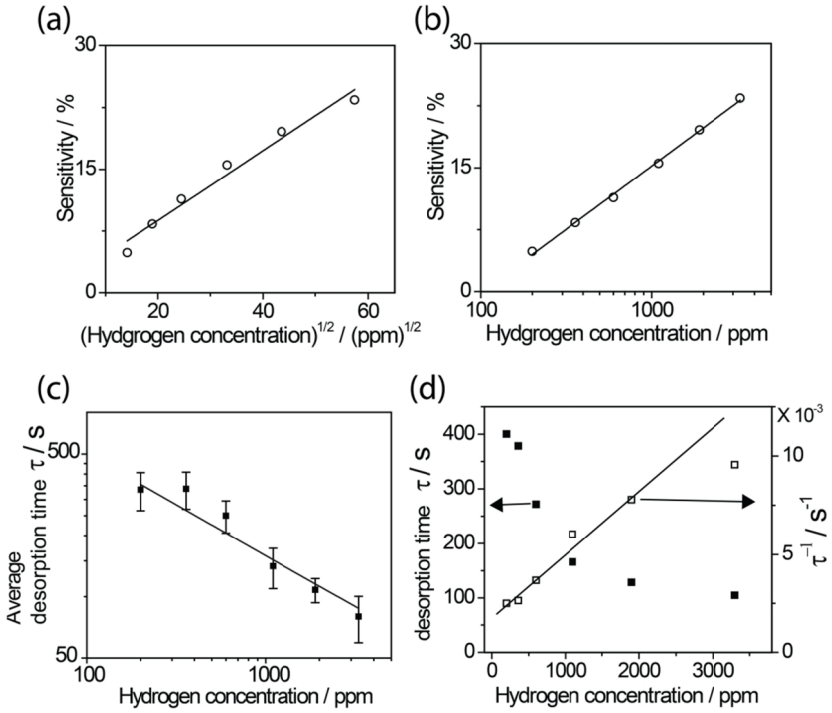

Figure 5.7 Hydrogen sensing performance of a Pd-rGO device: (a) sensitivity as a function of square root of hydrogen concentration, (b)Sensitivity as a function of hydrogen concentration on the log scale, (c) average desorption time as a function of hydrogen concentration on logarithmic scale and (d) desorption time as a function of hydrogen concentration. Data plotted for comparison with Figure 5.6 (c) and (d).

For comparison with the response of a Pd-CNT device, sensitivity of one of the Pd-rGO device (one of the devices shown in *Figure 5.4d*) is plotted as a function of square root of H_2 concentration in *Figure 5.7a*. The same data plotted as a function of H_2 concentration on a logarithmic scale is shown in *Figure 5.7b*. *Figure 5.7c* is shows the logarithmic

relationship between desorption time and hydrogen concentration averaged for 4 individual devices. *Figure 5.7d* is the relationship between desorption time and hydrogen concentration for the same device as in *Figures 5.7 a and b.*

Our data clearly shows that Temkin isotherm, i.e. logarithmic fit, best describes the relationship between sensitivity and hydrogen concentration in our devices. This suggests that desorption of hydrogen is not a simple second order reaction. However, the reasons for the dependence of desorption time on square of hydrogen concentration, as observed in our data, is unclear.

5.3.3. Temperature dependence in Pd-rGO devices

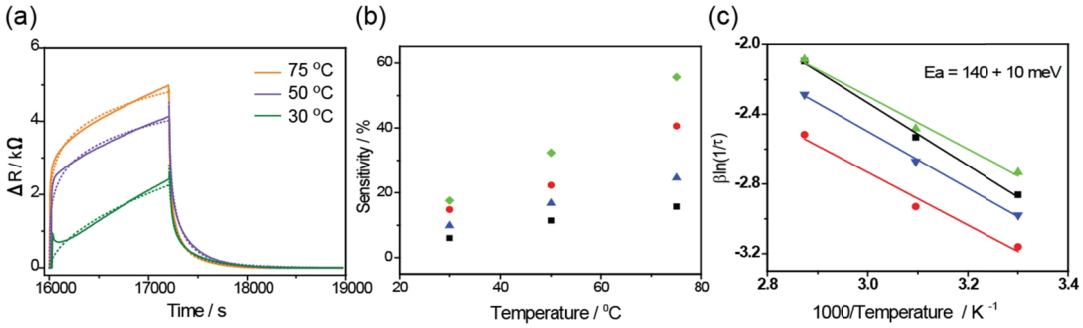

Figure 5.8 (a) Resistance response of a Pd-rGO device to 3300 ppm hydrogen at 30, 50 and 75 °C; the stretched exponential fits are the respective coloured dotted lines. (b) Sensitivity as a function of temperature for 4 individual devices (a). (c) Average desorption rate as a function of 1/temperature for the devices as in (b). Solid lines are the linear fits to the respective datasets.

Hydrogen sensitivity of Pd-rGO devices was compared at 3 different temperatures. *Figure 5.8a* shows the response pulses of a device to 3300 ppm of H_2 at temperatures 30, 50, and 75 °C. *Figure 5.8b* shows the dependence of sensitivity on temperature for 4 individual devices at of 3300 ppm of H_2. With increasing temperature, the sensitivity increased and the response time decreased. At higher temperatures the increase in sensitivity is attributed to the increased catalytic dissociation of hydrogen molecules.

Assuming that the dependence of desorption rate on temperature here follows the Arrhenius equation:

$$k = Ae^{\left(-E_a / k_B T\right)} \tag{5.12}$$

and

$$k = \frac{d}{dt}\left(\frac{\Delta R}{R_2}\right)_{t=0} \tag{5.13}$$

Using Equations (5.7, 5.12 and 5.13) we get

$$\ln(k) = \ln(A) - \frac{E_a}{k_B T} = \beta \ln(1/\tau) \tag{5.14}$$

where *k* is the desorption rate, *A* is a constant, E_a the activation energy and k_B the Boltzmann constant. Here, τ is the average time constant for desorption and its value is extracted using *Equation (5.8).* The Arrhenius plot in *Figure 5.8c* is derived from 3300 ppm hydrogen response pulses of 4 individual devices (same devices as in *Figure 5.8b*) The straight line fits yield a desorption activation energy of 140 $\pm$ 10 meV; significantly lower than a recent report.[183] Recently a theoretical report has predicted much higher binding energies (~1 eV) for dissociation of H_2 on Pd coated graphene.[193] It is important to note that this interpretation must be considered with caution. The stretched exponential implies that there is not one single response time, consistent with the Temkin isotherm not having one single energy behaviour, so that the energy inferred above can only be considered as an average or representative value. In addition the response of the sensor rig (i.e., mixing time, turbulence, etc.) has not been carefully characterised. Nonetheless, this activation energy can be used as an indicative guide for comparison with other literature values.

5.3.4. Complex response at ambient temperature

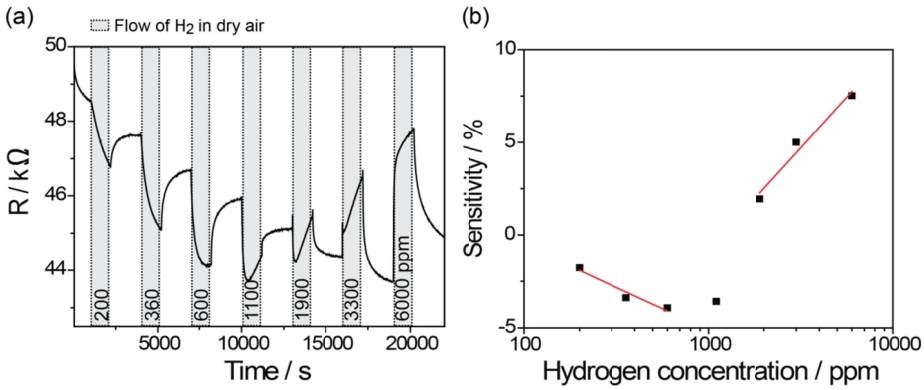

Figure 5.9 (a) Resistance response of Pd-rGO devices to hydrogen flow at 30 °C and (b) Sensitivity as a function of hydrogen concentration showing separate logarithmic fits (solid lines) for the positive and negative resistance responses of the data in (a).

Most of the Pd-rGO devices when exposed to hydrogen at 30°C initially showed a decrease in the resistance with increasing hydrogen concentration as shown in *Figure 5*.9a. As the concentration of hydrogen was increased further, the resistance response changed from negative to positive; whilst the magnitude of the response kept on increasing with increasing H_2 concentration. *Figure 5.9b* shows the isotherm plot of the data in *Figure 5.9a* with separate logarithmic fits to positive and negative responses.

A similar type of complex response has been observed for Pd-MIS devices operated in UHV and at 423 K.[188] In these devices the work function change was initially negative (corresponding to positive change in resistance) and switched to positive at higher concentrations of hydrogen. It was suggested that the Pd surface was pre-adsorbed with carbon and consisted of two types of hydrogen adsorption states. However, here, the devices were operated in dry air but at low temperatures hence the role of pre-adsorbed water molecules in minor quantities cannot be neglected. For carbon nanotubes (CNT), containing oxygen defects, it has been observed that water vapour is preferentially absorbed on the polar oxygen defects and reduces the p-type doping of the CNT.[194] It has

also been reported that water molecules attach to rGO in the case of Pd decorated rGO.[195] When such a device is exposed to H_2 the dissociated hydrogen, reaching the Pd-rGO interface, could combine with adsorbed OH species resulting in an increase in p-type carriers in rGO and hence a decrease in the resistance. Upon further adsorption of H_2 the numbers of states containing OH species reduces and the usual positive resistance response is recovered. Accordingly, at higher temperatures only positive response was observed. Furthermore when the coverage of Pd was increased, resulting in an increased hydrogen capture and dissociation, only positive resistance response was observed.

5.3.5. Effect of humidity

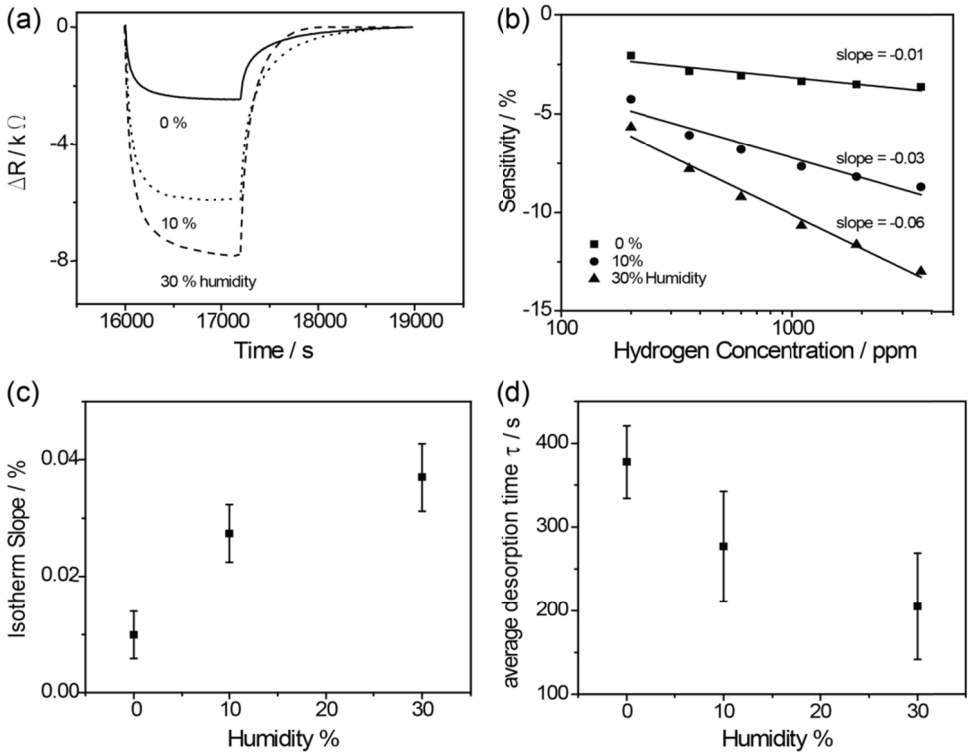

Figure 5.10 (a) Resistance response of a Pd-rGO device when exposed to 3300 ppm hydrogen at 50 °C. in 0 % (dry air), 10 % and 30 % humidity (b) Sensitivity as a function of hydrogen concentration for the same device as in (a). (c) Absolute values of the isotherm slope as a function of humidity averaged for 5 individual devices of the same type. (d) average desorption time versus humidity averaged over 5 individual devices for 3300 ppm of hydrogen.

To understand the effect of humidity on the response of Pd-rGO devices, air with 0, 10 and 30 % humidity was used as a carrier gas. The data in *Figure 5.10* is from devices consisting of ~ 3 nm rGO (GO concentration 5 mg/ml) and ~1 nm Pd operated at 50 °C. *Figure 5.10a* shows the negative resistance responses of a device to a 3300 ppm pulse of H_2 as the humidity is varied from 0 to 30 %. A significant increase in the response is seen as the humidity increases and this is observed for the whole range of the hydrogen concentrations studied, as evident from the isotherm plot in *Figure 5.10b* for the same device. *Figure 5.10c* shows a plot of the absolute isotherm slope values against humidity averaged over 5 individual devices. The absolute isotherm slope values also increase with increasing humidity; the presence of moisture in the air not only increases the overall response but also shortens the recovery time as seen in the plot of desorption time for 3300 ppm of H_2 versus humidity (*Figure 5.10d*).

As discussed in Section 5.3, water molecules readily attach to the remnant oxygen defects on rGO resulting in a decrease in the device resistance upon exposure to H_2. With increase in humidity, the amount of water molecules attached to the surface increases and hence a higher sensitivity. At higher concentrations of adsorbed hydrogen on the surface the energy barrier for desorption is smaller hence a faster desorption.

5.4. Effect of Pd and rGO thickness on sensitivity

In order to understand the effect of device parameters such as Pd and rGO thickness on sensitivity we made two different types of devices. One set maintained a consistent thickness of rGO while varying the Pd thickness, and the other maintained constant thickness of Pd while varying the rGO thickness.

5.4.1. Effect of Pd thickness

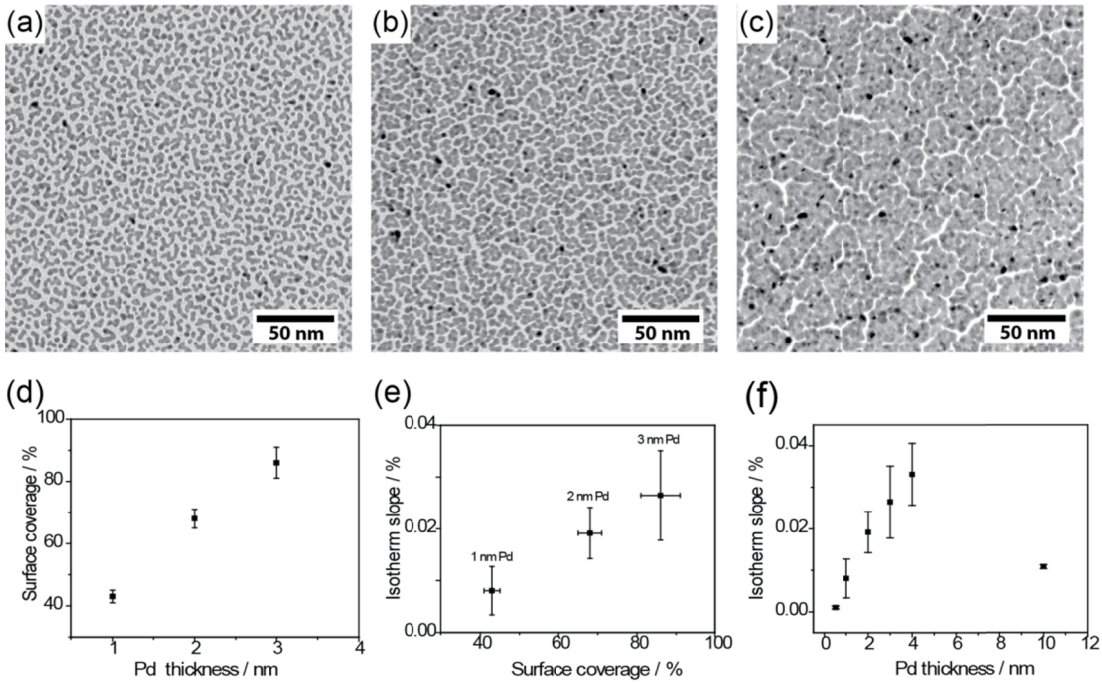

Figure 5.11 Low magnification TEM images of rGO sheets with Pd of nominal thicknesses (a) 1 nm (b) 2 nm and (c) 3 nm Pd. (d) Surface coverage versus nominal thickness of Pd on rGO from the TEM images. (e) Isotherm slope of hydrogen sensitivity versus Pd surface coverage on rGO. (f) Isotherm slope of hydrogen sensitivity versus nominal thickness of Pd on rGO.

For the investigation of the effect of Pd thickness, sensor devices with rGO of nominal thickness 3 nm (GO suspension concentration 5 mg/ml) were coated with 6 different thicknesses of Pd (0.5, 1, 2, 3, 4, and 10 nm) and the tests were run at 50 °C in dry air. *Figures 5.11a, b and c* are low magnification TEM images of rGO with Pd of nominal thicknesses 1, 2, and 3 nm respectively. Since at thicknesses of Pd higher than 3 nm the suspended films of rGO showed holes due to heat transfer, TEM images of only up to 3 nm Pd thicknesses were studied. At ~1 nm thickness, Pd clearly shows a discontinuous, island type morphology on rGO forming nanoparticles with a range of sizes. From the TEM images the surface coverage of Pd nanoparticles on the rGO were extracted. A plot of

surface coverage against Pd thickness, *Figure 5.11d,* shows that the surface coverage increases with Pd nominal thickness.

Figures 5.11e and f show the relationship between the isotherm slope values and Pd surface coverage and thickness on rGO. A range of sensitivity and slope values were obtained even if the devices were prepared in the same way and operated simultaneously. The slope values, which average the sensitivity over hydrogen pressure, were considered to obtain a relationship between sensitivity and Pd thickness. *Figure 5.11e and f* show that the slope values increase with the surface coverage monotonically and follow a similar trend with the Pd thickness, the exception is 10 nm Pd.

Table 5.1 Thickness of Pd on rGO devices and the corresponding resistance values averaged over several devices of the same thickness.

Pd thickness / nm	Average Resistance / kΩ
Bare rGO	3 ± 2
0.5	3 ± 2
1	4 ± 2
2	20 ± 3
3	30 ± 20
4	1.0 ± 0.6
10	0.20 ± 0.09

Table 5.1 gives the values of resistances averaged over several devices of each Pd thickness. As discussed in Section 5.2, with the increasing Pd thickness on rGO the resistivity of the devices increased, as long as the Pd coverage was below the percolation threshold. For 4 and 10 nm Pd devices the resistance values drop, suggesting that a

percolating Pd layer has formed and that the charge conduction is through Pd. All the devices showed response to hydrogen, but the sensitivity dropped for 10 nm Pd coated devices. This indicates that below the percolation threshold of Pd, the sensitivity is largely dependent on the interface area, in contrast to the case of Pd decorated carbon nanotube hydrogen gas sensors where the effect of the number of particles was more pronounced.[196] The dependence of the sensitivity on interface area, observed here, is expected as the device response is dependent on the number of hydrogen dipoles formed at the interface.

5.4.2. Effect of rGO thickness

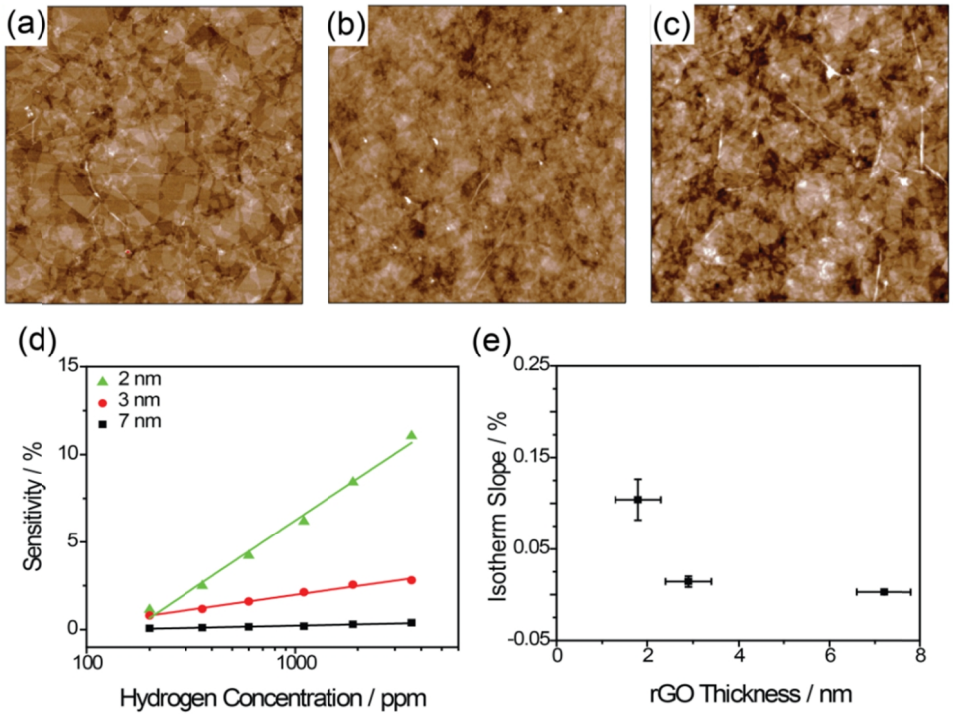

Figure 5.12 5 µm square AFM images of (a) 2 nm, (b) 3 nm and (c) 7 nm rGO devices (full height scale 8 nm for (c) and (d) and 12 nm for (e)); each with Pd of nominal thickness 1 nm. (d) Sensitivity as a function of hydrogen gas concentration for 3 different thicknesses of rGO and (e) isotherm slope as a function of rGO thickness.

The thickness of the rGO film was controlled by varying the concentration of the GO suspension. To investigate the effect of rGO thickness on the sensing mechanism, devices were fabricated with thicknesses of 1.8 ± 0.5, 2.9 ± 0.5, and 7.2 ± 0.6 nm. Each of these devices were coated with Pd of nominal thickness 1 nm and operated at 50 °C in dry air. AFM images in *Figure 5.12a, b and c* show continuous and homogeneous thin films of rGO in all three cases. *Figure 5.12d* shows representative data for sensitivity versus H_2 concentration for three different rGO thicknesses. The slope values of the fits to the isotherms are plotted as a function of rGO thickness in *Figure 5.12e*.

Since, the sensitivity is determined by the interaction between the target gas and the surface of a sensor, the greater the surface area greater the sensitivity. Suppose the rGO film consists of a surface and bulk layers with resistances R_s and R_b respectively. As the thickness of the rGO film increases, the thickness of the bulk increases and hence R_b decreases. As a result more current passes through the bulk than the surface layer. In addition, successive graphene layers will electrostatically screen the dipole formed at the Pd-rGO interface, decreasing the sensitivity even further. Thus, with increase in thickness of the rGO film, the charge screening effect and the decreased resistance of the bulk decrease the sensitivity of the surface layer.

Here the lowest possible thickness of rGO achieved was ~2 nm since the devices with thicknesses of rGO less than 1 nm did not conduct (the rGO did not form a continuous layer as shown in Chapter 2). Considering the effects of Pd and rGO thicknesses it is found that the devices having thinner films of rGO and higher coverages of Pd (below the percolation threshold) provide the highest sensitivity values.

5.5. Sensitivity and selectivity of metal-rGO devices

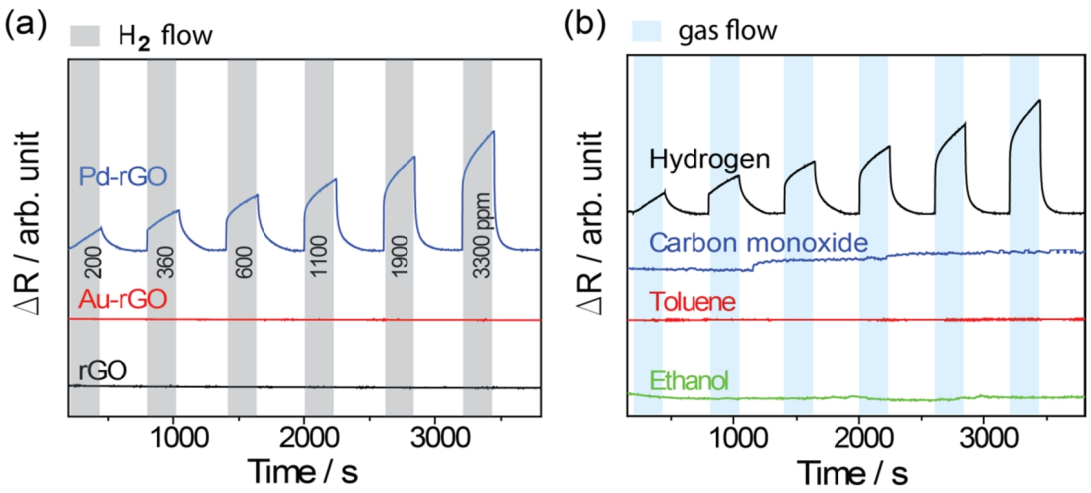

Figure 5.13 (a) Response of uncoated (black), Au (red) and Pd coated rGO (blue) to the flow of hydrogen gas in air (shown in gray shaded columns). (b) Response of Pd coated rGO device to ethanol (green), toluene (red), carbon monoxide (blue) and hydrogen (black) flow (gas flow shown in blue shaded columns). Data courtesy of Dr. James Covington, School of Engineering, University of Warwick.

The responses of bare rGO, Au-rGO and Pd-rGO to hydrogen gas are shown in *Figure 5.13a.* Only the Pd-rGO device responded upon exposure to hydrogen. Additionally, Pd-rGO devices were tested for gases such as ethanol, toluene, and carbon monoxide. The responses to these gases and hydrogen are plotted in *Figure 5.13b;* Pd-rGO devices responded only to hydrogen and not to the other gases tested here.

rGO on its own has been found to be sensitive to several analytes such as nitrogen dioxide, ammonia, water, and acetone. However, sensitivity to other analytes can be induced by catalytic coating. Clearly, Pd coating not only induces sensitivity but also the devices are selective to hydrogen. Pd gate MIS devices have been operated at elevated temperatures (above 100 °C) to detect hydrogen and have been shown to be sensitive to all molecules that can give hydrogen atoms such as hydrogen sulphide, ethanol, and

unsaturated hydrocarbons.[189] Further cross sensitivity to carbon monoxide has been observed in Pt doped holey rGO hydrogen sensors.[14] However, no response to ethanol or carbon monoxide was seen in the Pd-rGO devices.

5.6. Pd-graphene hydrogen gas sensor

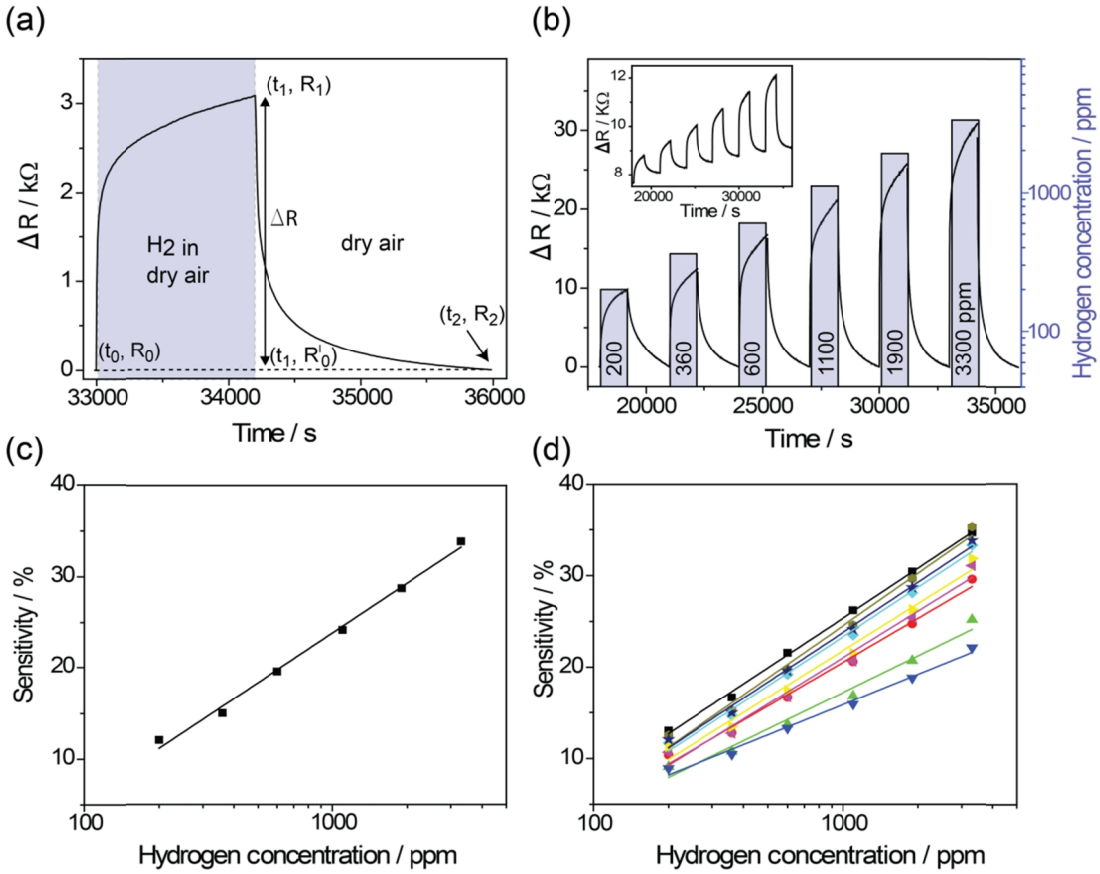

Figure 5.14 Resistance response of a Pd-graphene device to (a) 3300 ppm hydrogen gas at 50 °C, (background subtracted) and (b) various concentrations of hydrogen gas (inset shows raw data). (c) Sensitivity as a function of hydrogen concentration with a linear fit (solid line) for the data in (b). (d) Sensitivity as a function of hydrogen concentration with the linear fits (solid line) for 9 individual devices.

CVD grown graphene devices when coated with Pd also show a significant response to hydrogen. Data in *Figure 5.14* was obtained from a device containing a double

layer of graphene with ~1 nm thick Pd coating and operated at 75 °C in dry air. A prompt increase in resistance of the device is observed upon flow of 3300 ppm of hydrogen (*Figure 5.14a*). Additionally, the increasing resistance with increasing concentration of hydrogen (isotherm plot) shows a linear trend on a logarithmic scale (*Figures 5.14b* and *c*). Unlike rGO devices, these devices always showed a positive resistance response upon exposure to hydrogen. Again the sensitivity values of the individual devices of the same type differ from each other as evident in *Figure 5.14d*.

The logarithmic dependence of sensitivity on hydrogen concentration indicates that the sensing mechanism is likely to be the same for the Pd-graphene as that for Pd-rGO devices. The response of graphene samples was always positive, consistent with the fact that CVD grown graphene is more hydrophobic than rGO. For the set of data in *Figure 5.14d,* the values of hydrogen concentration at which the sensitivities are zero are between 35 and 55 ppm. These values are less than those obtained for rGO (between 90 and 130 ppm). The average sensitivity from 9 similarly prepared Pd-graphene devices (~0.6 nm thick graphene film and 1 nm thick Pd), for 3300 ppm hydrogen with 1 nm Pd, is 31 $\pm$ 4 % and that from 6 Pd-rGO devices (~2 nm thick rGO film and 1 nm thick Pd), for 3300 ppm Hydrogen, is 33 $\pm$ 26 %.

Graphene devices, possessing continuous layers and lower defects compared to rGO, showed less variation in the sensitivity values than the rGO devices. The thickness of a graphene device is estimated to be ~0.6 nm and that of the lowest thickness rGO device is ~2 nm. The layer of rGO was found to be discontinuous for thicknesses below 2 nm. Interestingly, the sensitivity of Pd-rGO is comparable to Pd-rGO, suggesting that the mobility of the starting material is not the dominant factor for the sensitivity.

5.6.1. Desorption time in Pd-graphene device

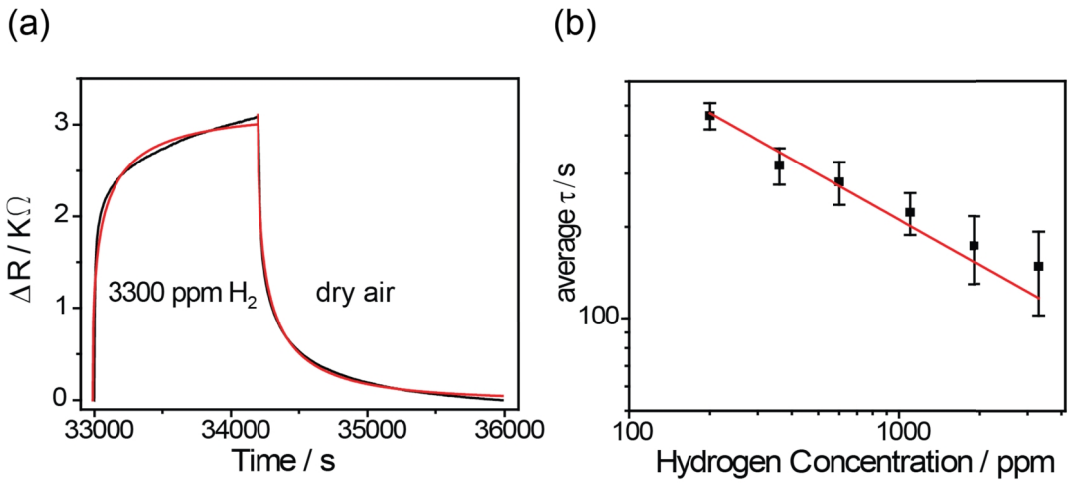

Figure 5.15 (a) Stretched exponential fit (red) to a 3300 ppm hydrogen response pulse (black) and (b) average desorption time as a function of hydrogen concentration for Pd-graphene devices.

To extract the average time taken by hydrogen atoms to desorb from Pd-graphene devices the stretched exponentials were fitted to each pulse and the extracted parameters averaged over several devices. *Figure 5.15a* shows a representative response pulse to 3300 ppm of H_2 (black) fitted with stretched exponential curve (red). The data is obtained from a devices consisting of 2 layers of graphene coated with 1 nm Pd. The average desorption time as function of hydrogen concentration shown in *Figure 5.15b,* decreases from 460 ± 50 s for 200 ppm of H_2 to 150 ± 50 s for 3300 ppm of H_2; these values are consistently higher than for rGO devices consisting of ~2 nm rGO coated with 1 nm Pd (340 ± 70 s for 200 ppm of H_2 and 80 ± 20 s for 3300 ppm of H_2). A linear fit with a fixed slope of -0.5 agrees well with the dataset in *Figure 5.15*b, as was the case for the Pd-rGO devices.

5.6.2. Temperature dependence in Pd-graphene devices

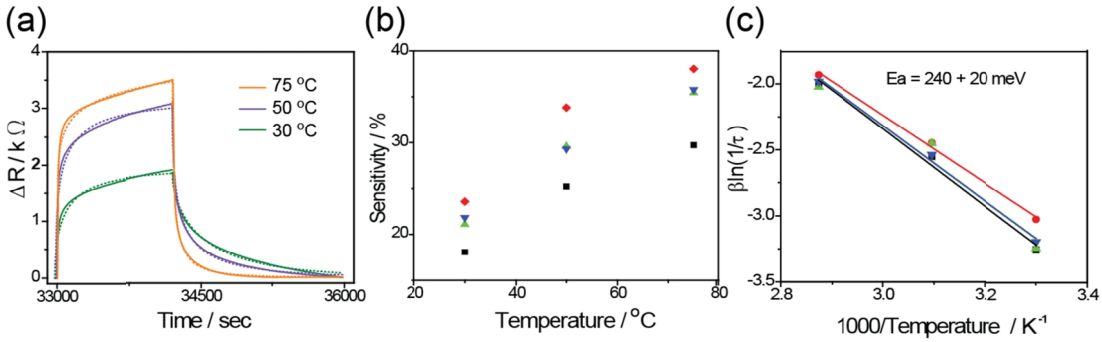

Figure 5.16 (a) Resistance response of a Pd-graphene device to 3300 ppm hydrogen at 30, 50 and 75 °C; the respective stretched exponential fits are shown in coloured dotted lines. (b) Sensitivity as a function of temperature for the data in (a). (c) Average desorption rate (1/τ) versus 1/temperature for 4 different devices. Solid lines are the linear fits to the respective data points.

Figure 5.16a shows the resistance response of a Pd-graphene device at 30, 50 and 75 °C with the stretched exponential fits to each dataset. The dependence of sensitivity and desorption time on temperature is shown in *Figures 5.16a and b* respectively. Clearly, with increasing temperature from 30 to 75 °C, desorption time decreases and the sensitivity increases by ~1.5 times; the increase is less than that in rGO (~2.5 times). From the Arrhenius plots (discussed in Section 5.3), *Figure 5.16c*, the desorption activation energy is found to be 240 ± 20 meV, consistent with a recent report[183] and a 100 meV higher than that for Pd-rGO devices. Again, as mentioned in the case of rGO devices, the activation energies must be treated with caution because of the Temkin isotherm and uncertainity over the rig characteristics.

As observed with rGO devices, at higher temperatures the increase in sensitivity is attributed to the increased catalytic dissociation of hydrogen molecules while the increased desorption rate is as expected with increased barrier for desorption to be more readily overcome.

5.7. Conclusions

Hydrogen gas sensors incorporating Pd–rGO devices were fabricated and studied under various operation conditions. The devices showed a logarithmic dependence of sensitivity on hydrogen concentration. In comparison with the widely studied hydrogen gas sensors operated at temperatures above 100°C[197-199] these devices showed a fast response at room temperature for hydrogen concentrations well below the lower explosive limit. In order to improve sensing performance the device fabrication parameters such as rGO thickness and Pd thickness were investigated and it was shown that sensitivity is increased by decreasing the rGO thickness (whilst maintaining a continuous layer) and increasing the Pd thickness (up to just below the percolation threshold). Further, although previously reported hydrogen sensors have been found to be sensitive to other gases like CO and alcohols or involve expensive production techniques,[176, 179, 199] these Pd-rGO devices showed no significant response to carbon monoxide, ethanol, or toluene and are cheap to fabricate. A comparative study of Pd coated rGO with Pd coated CVD grown graphene was also performed; a similar sensing mechanism was observed for both. Although, graphene devices showed less variation between the devices and indicated lower detectable limits than the rGO devices, their fabrication is more complex and expensive.

In summary, the fabrication and application of Pd coated rGO and graphene as hydrogen gas sensors was demonstrated. The sensors were capable of detecting < 200 ppm of H_2 with reproducible performance across a wide range of temperature and humidity. These devices have not been optimised yet and they are already a promising candidate for commercial applications because of 1) the low cost and simple fabrication technique of rGO devices, 2) room temperature operation, 3) fast response at ambient,

and 4) selectivity. Further device optimisation may result in a higher sensitivity and lower detectable limit for hydrogen. The selectivity, sensitivity and consistent performance of Pd-rGO/graphene sensors have shown that with suitable coating a wide variety of graphene sensors could be prepared.

Chapter 6. **Summary, Conclusions and Future Work**

The aim of my PhD was to produce graphene by chemical methods for organic photovoltaic cells, however, the rather high sheet resistances in these rGO films made them unsuitable for photovoltaic devices. Instead the study on the structure of GO revealed the crystallographic nature and high transparency of these films in TEM. These results turned out to be extremely important in shaping the outcome of my project.

As the explosion of research has occurred in the field of graphene, Chapter 1 has been utilised to introduce the background of the research relevant to the work done here. The methods for sample fabrication along with their standard characterisations and comparisons with reports in the literature are discussed in Chapter 2. The results on the structure of GO, hybrid-CMG structures and applications of metal-CMG as hydrogen gas sensor are discussed in Chapters 3, 4 and 5.

In TEM, GO sheets were found to be highly transparent, reasonably stable and possessing crystalline structure. The study on the structure using TEM showed that GO, on average, preserves the lattice structure and carbon–carbon bond length of the unmodified graphene. The compositional analysis revealed that the as-produced GO is actually composed of functionalised graphene like sheets (bwGO) to which oxidative debris is strongly adhered. Unlike GO the functionalised graphene like material, called bwGO, on its own is conducting and not suspendable in water. The oxidative debris strongly interferes with the intrinsic properties of the bwGO and its effects should be considered in the studies where direct covalent functionalization of the graphene lattice is required. To date, no model of GO, suggested in the literature, has accounted for the facts demonstrated in the study here, implying that the models for the as-produced GO need revisiting.

The growth and interactions of technologically important organic semiconductor (F_{16}CuPc) with GO was studied in TEM. GO acted as an excellent support for these materials as it provided a low background and well defined diffraction pattern for calibration. The study of F_{16}CuPc molecules on GO showed thin film morphology showing fibre texture down to sub-monolayer. The molecules lie perpendicular to the GO sheet; however, evidence of the molecules lying flat on the rGO sheet is also found and is attributed to the increase in the number of π-electrons in rGO. This suggests that by changing the functionalization of the CMG sheets the packing of the molecules can be changed and desired charge transport properties can be obtained.

The results of metal-CMG structures indicated that the morphology of the metal on CMG is determined by the metal-CMG interactions. A range of morphologies can be obtained depending on the theoretically predicted values of cohesive binding energies of the metal atoms and the energy diffusion barriers on graphene. Thus, by gaining understanding of the interactions a fine control over the morphology of a metal on CMG

could be obtained. This knowledge was utilised to fabricate a metal-rGO hydrogen gas sensor. Pd-rGO hydrogen gas sensors showed fast response at room temperature over a wide range of pressures well below the lower explosive limit of hydrogen. The study on hydrogen sensors has illustrated a simple method of fabrication of CMG based sensors. By applying a suitable coating to CMG devices, different types of sensors could be produced.

Future Works

From the study of GO in TEM the most obvious application was the use of these sheets as a TEM support film for studying nanoparticles and biological objects. We have already demonstrated successful usage of the GO support films for studying different materials.[130, 200] The first application of graphene discussed in the Nobel lecture by Prof. Novoselov, is its use as TEM support films and our work has been mentioned.[201] GO based support films can be further developed by changing the functionality of the GO sheets to make it applicable for a variety of materials. The technique of making TEM support films could be further developed for low cost production. Also, graphene based TEM supports are now commercially available.

The work in this thesis has opened several avenues to be explored and a number of PhD projects have been undertaken to carry out the research. The study on the structure and composition of GO and bwGO is taken further by Dr. Rourke's group in the Department of Chemistry, University of Warwick. The statistics on the growth of Au nanoparticles on GO is being further analysed in the light of Monte-Carlo simulations, using the data obtained in this study, in collaboration with Dr. Bell in the Department of Physics, University of Warwick. CMG based sensors are being further developed for other analytes and also to make the devices compatible with the existing technology. This work is carried out by the group of Dr. Covington in the School of Engineering, University of Warwick.

Abbreviations

aGO	as-produced graphene oxide
AFM	atomic force microscopy
bwGO	base washed graphene oxide
CIF	crystallographic information file
CMG	chemically modified graphene
CNT	carbon nanotube
CVD	chemical vapour deposition
DI	de-ionised
F16CuPc	fluorinated copper phthalocyanine
FLG	few layer graphene
FTIR	Fourier transform infrared spectroscopy
GO	graphene oxide – referred to as-produced graphene oxide
HOPG	highly oriented pyrolitic graphite
HR-TEM	high resolution transmission electron microscopy
ISD	island size distribution
MFC	mass flow controller

MMA	methylmethacryalate
NMP	n-methyl-2-pyrrolidone
OD	oxidative debris
PCB	printed circuit board
PMMA	polymethylmethacryalate
PPM	parts per million
PVD	physical vapour deposition
rGO	reduced graphene oxide
SAED	selected area electron diffraction
SCCM	standard cubic centimetre per minute
SEM	scanning electron microscopy
TEM	transmission electron microscopy
TGA	thermogravimetric analysis
UHV	ultra high vacuum
XPS	x-ray photo-electron spectroscopy
XRD	x-ray diffraction

Bibliography

1. Geim, A. K., Graphene: status and prospects. *Science* **2009**, 324, 1530-1534.

2. Lin, Y. M.; Dimitrakopoulos, C.; Jenkins, K. A.; Farmer, D. B.; Chiu, H.-Y.; Grill, A.; Avouris, P., 100-GHz Transistors from wafer-scale epitaxial graphene. *Science* **2010**, 327, 662-662.

3. Liu, Y.; Dong, X.; Chen, P., Biological and chemical sensors based on graphene materials. *Chemical Society Reviews* **2012**, 41, 2283-2307.

4. Geim, A. K.; Novoselov, K. S., The rise of graphene. *Nature Materials* **2007**, 6, 183-191.

5. Wallace, P. R., The band theory of graphite. *Physical Review* **1947**, 71, 622-634.

6. Wintterlin, J.; Bocquet, M. L., Graphene on metal surfaces. *Surface Science* **2009**, 603, 1841-1852.

7. Katsnelson, M. I., Graphene: carbon in two dimensions. *Materials Today* **2007**, 10, 20-27.

8. Morozov, S. V.; Novoselov, K. S.; Katsnelson, M. I.; Schedin, F.; Elias, D. C.; Jaszczak, J. A.; Geim, A. K., Giant intrinsic carrier mobilities in graphene and its bilayer. *Physical Review Letters* **2008**, 100, 016602-016605.

9. Balandin, A. A.; Ghosh, S.; Bao, W.; Calizo, I.; Teweldebrhan, D.; Miao, F.; Lau, C. N., Superior thermal conductivity of single-layer graphene. *Nano Letters* **2008**, 8, 902-907.

10. Nair, R. R.; Blake, P.; Grigorenko, A. N.; Novoselov, K. S.; Booth, T. J.; Stauber, T.; Peres, N. M. R.; Geim, A. K., Fine structure constant defines visual transparency of graphene. *Science* **2008**, 320, 1308-1308.

11. Lee, C.; Wei, X.; Kysar, J. W.; Hone, J., Measurement of the elastic properties and intrinsic strength of monolayer graphene. *Science* **2008**, 321, 385-388.

12. Xu, Y.; Long, G.; Huang, L.; Huang, Y.; Wan, X.; Ma, Y.; Chen, Y., Polymer photovoltaic devices with transparent graphene electrodes produced by spin-casting. *Carbon* **2010**, 48, 3308-3311.

13. Stankovich, S.; Dikin, D. A.; Dommett, G. H. B.; Kohlhaas, K. M.; Zimney, E. J.; Stach, E. A.; Piner, R. D.; Nguyen, S. T.; Ruoff, R. S., Graphene-based composite materials. *Nature* **2006**, 442, 282-286.

14. Vedala, H.; Sorescu, D. C.; Kotchey, G. P.; Star, A., Chemical sensitivity of graphene edges decorated with metal nanoparticles. *Nano Letters* **2011**, 11, 2342-2347.

15. Li, J.; Liu, C. y., Ag/graphene heterostructures: synthesis, characterization and optical properties. *European Journal of Inorganic Chemistry* **2010**, 2010, 1244-1248.

16. Xu, C.; Wang, X.; Zhu, J., Graphene – metal particle nanocomposites. *The Journal of Physical Chemistry C* **2008**, 112, 19841-19845.

17. Wan, X.; Huang, Y.; Chen, Y., Focusing on energy and optoelectronic applications: a journey for graphene and graphene oxide at large scale. *Accounts of Chemical Research* **2012**, 45, 598-607.

18. Chen, Z. H.; Lin, Y. M.; Rooks, M. J.; Avouris, P., Graphene nano-ribbon electronics. *Physica E-Low-Dimensional Systems & Nanostructures* **2007**, 40, 228-232.

19. Ishigami, M.; Chen, J. H.; Cullen, W. G.; Fuhrer, M. S.; Williams, E. D., Atomic structure of graphene on SiO_2. *Nano Letters* **2007**, 7, 1643-1648.

20. Meyer, J. C.; Kisielowski, C.; Erni, R.; Rossell, M. D.; Crommie, M. F.; Zettl, A., Direct imaging of lattice atoms and topological defects in graphene membranes. *Nano Letters* **2008**, 8, 3582-3586.

21. Zhang, Y.; Brar, V. W.; Wang, F.; Girit, C.; Yayon, Y.; Panlasigui, M.; Zettl, A.; Crommie, M. F., Giant phonon-induced conductance in scanning tunnelling spectroscopy of gate-tunable graphene. *Nature Physics* **2008**, 4, 627-630.

22. Banhart, F.; Kotakoski, J.; Krasheninnikov, A. V., Structural defects in graphene. *ACS Nano* **2011**, 5, 26-41.

23. Meyer, J. C.; Geim, A. K.; Katsnelson, M. I.; Novoselov, K. S.; Booth, T. J.; Roth, S., The structure of suspended graphene sheets. *Nature* **2007**, 446, 60-63.

24. Lui, C. H.; Liu, L.; Mak, K. F.; Flynn, G. W.; Heinz, T. F., Ultraflat graphene. *Nature* **2009**, 462, 339-341.

25. Wilson, N. R.; Pandey, P. A.; Beanland, R.; Rourke, J. P.; Umberto., L.; Rowlands, G.; Römer, R. A., On the structure and topography of free-standing chemically modified graphene. *New Journal of Physics* **2010**, 12, 125010-125031.

26. Castro Neto, A. H.; Guinea, F.; Peres, N. M. R.; Novoselov, K. S.; Geim, A. K., The electronic properties of graphene. *Reviews of Modern Physics* **2009**, 81, 109-162.

27. Dreyer, D. R.; Ruoff, R. S.; Bielawski, C. W., From conception to realization: an historial account of graphene and some perspectives for its future. *Angewandte Chemie International Edition* **2010**, 49, 9336-9344.

28. Boehm, H. P.; Stumpp, E., Citation errors concerning the first report on exfoliated graphite. *Carbon* **2007**, 45, 1381-1383.

29. Nakajima, T.; Matsuo, Y., Formation process and structure of graphite oxide. *Carbon* **1994**, 32, 469-475.

30. Hummers, W. S.; Offeman, R. E., Preparation of graphitic oxide. *Journal of American Chemical Society* **1958**, 80, 1339-1339.

31. Morgan, A. E.; Somorjai, G. A., Low energy electron diffraction studies of gas adsorption on the platinum (100) single crystal surface. *Surface Science* **1968**, 12, 405-425.

32. May, J. W., Platinum surface LEED rings. *Surface Science* **1969**, 17, 267-270.

33. Hamilton, J. C.; Blakely, J. M., Carbon segregation to single crystal surfaces of Pt, Pd and Co. *Surface Science* **1980**, 91, 199-217.

34. McConville, C. F.; Woodruff, D. P.; Kevan, S. D., The electronic structure of graphitic overlayers on Ni{100}. *Surface Science* **1986**, 171, L447-L453.

35. Van Bommel, A. J.; Crombeen, J. E.; Van Tooren, A., LEED and auger electron observations of the SiC(0001) surface. *Surface Science* **1975**, 48, 463-472.

36. Xuekun, L.; Minfeng, Y.; Hui, H.; Rodney, S. R., Tailoring graphite with the goal of achieving single sheets. *Nanotechnology* **1999**, 10, 269-273.

37. Novoselov, K. S.; Geim, A. K.; Morozov, S. V.; Jiang, D.; Zhang, Y.; Dubonos, S. V.; Grigorieva, I. V.; Firsov, A. A., Electric field effect in atomically thin carbon films. *Science* **2004**, 306, 666-669.

38. Berger, C.; Song, Z. M.; Li, T. B.; Li, X. B.; Ogbazghi, A. Y.; Feng, R.; Dai, Z. T.; Marchenkov, A. N.; Conrad, E. H.; First, P. N.; de Heer, W. A., Ultrathin epitaxial graphite: 2D electron gas properties and a route toward graphene-based nanoelectronics. *Journal of Physical Chemistry B* **2004**, 108, 19912-19916.

39. Hass, J.; Heer, W. A. d.; Conrad, E. H., The growth and morphology of epitaxial multilayer graphene. *Journal of Physics: Condensed Matter* **2008**, 20, 323202-323228.

40. Sutter, P. W.; Flege, J.-I.; Sutter, E. A., Epitaxial graphene on ruthenium. *Nature Materials* **2008**, 7, 406-411.

41. Ago, H.; Ito, Y.; Mizuta, N.; Yoshida, K.; Hu, B.; Orofeo, C. M.; Tsuji, M.; Ikeda, K.; Mizuno, S., Epitaxial chemical vapor deposition growth of single-layer graphene over cobalt film crystallized on sapphire. *ACS Nano* **2010**, 4, 7407-7414.

42. Li, X.; Cai, W.; An, J.; Kim, S.; Nah, J.; Yang, D.; Piner, R.; Velamakanni, A.; Jung, I.; Tutuc, E.; Banerjee, S. K.; Colombo, L.; Ruoff, R. S., Large-area synthesis of high-quality and uniform graphene films on copper foils. *Science* **2009**, 324, 1312-1314.

43. Kim, K. S.; Zhao, Y.; Jang, H.; Lee, S. Y.; Kim, J. M.; Kim, K. S.; Ahn, J.-H.; Kim, P.; Choi, J.-Y.; Hong, B. H., Large-scale pattern growth of graphene films for stretchable transparent electrodes. *Nature* **2009**, 706-710.

44. Eda, G.; Fanchini, G.; Chhowalla, M., Large-area ultrathin films of reduced graphene oxide as a transparent and flexible electronic material. *Nature Nanotechnology* **2008**, 3, 270-274.

45. Yang, D.; Velamakanni, A.; Bozoklu, G.; Park, S.; Stoller, M.; Piner, R. D.; Stankovich, S.; Jung, I.; Field, D. A.; Ventrice Jr, C. A.; Ruoff, R. S., Chemical analysis of graphene oxide films after heat and chemical treatments by x-ray photoelectron and micro-Raman spectroscopy. *Carbon* **2009**, 47, 145-152.

46. Becerril, H. A.; Mao, J.; Liu, Z.; Stoltenberg, R. M.; Bao, Z.; Chen, Y., Evaluation of solution-processed reduced graphene oxide films as transparent conductors. *ACS Nano* **2008**, 2, 463-470.

47. Wang, X.; Zhi, L.; Mullen, K., Transparent, conductive graphene electrodes for dye-sensitized solar cells. *Nano Letters* **2008**, 8, 323-327.

48. Wu, Z.-S.; Ren, W.; Gao, L.; Zhao, J.; Chen, Z.; Liu, B.; Tang, D.; Yu, B.; Jiang, C.; Cheng, H.-M., Synthesis of graphene sheets with high electrical conductivity and good thermal stability by hydrogen arc discharge exfoliation. *ACS Nano* **2009**, 3, 411-417.

49. Zhu, Y.; Murali, S.; Stoller, M. D.; Velamakanni, A.; Piner, R. D.; Ruoff, R. S., Microwave assisted exfoliation and reduction of graphite oxide for ultracapacitors. *Carbon* **2010**, 48, 2118-2122.

50. Stankovich, S.; Dikin, D. A.; Piner, R. D.; Kohlhaas, K. A.; Kleinhammes, A.; Jia, Y.; Wu, Y.; Nguyen, S. T.; Ruoff, R. S., Synthesis of graphene-based nanosheets via chemical reduction of exfoliated graphite oxide. *Carbon* **2007**, 45, 1558-1565.

51. Li, D.; Muller, M. B.; Gilje, S.; Kaner, R. B.; Wallace, G. G., Processable aqueous dispersions of graphene nanosheets. *Nature Nanotechnology* **2008**, 3, 101-105.

52. Pei, S.; Zhao, J.; Du, J.; Ren, W.; Cheng, H.-M., Direct reduction of graphene oxide films into highly conductive and flexible graphene films by hydrohalic acids. *Carbon* **2010**, 48, 4466-4474.

53. Wu, J.; Agrawal, M.; Becerril, H. c. A.; Bao, Z.; Liu, Z.; Chen, Y.; Peumans, P., Organic light-emitting diodes on solution-processed graphene transparent electrodes. *ACS Nano* **2009**, 4, 43-48.

54. Park, S.; An, J.; Jung, I.; Piner, R. D.; An, S. J.; Li, X.; Velamakanni, A.; Ruoff, R. S., Colloidal suspensions of highly reduced graphene oxide in a wide variety of organic solvents. *Nano Letters* **2009**, 9, 1593-1597.

55. Paredes, J. I.; Villar-Rodil, S.; Martínez-Alonso, A.; Tascón, J. M. D., Graphene oxide dispersions in organic solvents. *Langmuir* **2008**, 24, 10560-10564.

56. Mattevi, C.; Eda, G.; Agnoli, S.; Miller, S.; Mkhoyan, K. A.; Celik, O.; Mastrogiovanni, D.; Granozzi, G.; Garfunkel, E.; Chhowalla, M., Evolution of electrical, chemical, and structural properties of transparent and conducting chemically derived graphene thin films. *Advanced Functional Materials* **2009**, 19, 2577-2583.

57. Mao, S.; Cui, S.; Lu, G.; Yu, K.; Wen, Z.; Chen, J., Tuning gas-sensing properties of reduced graphene oxide using tin oxide nanocrystals. *Journal of Materials Chemistry* **2012**, 22, 11009-11013.

58. Zhang, X. Q.; Feng, Y. Y.; Tang, S. D.; Feng, W., Preparation of a graphene oxide-phthalocyanine hybrid through strong pi-pi interactions. *Carbon* **2010**, 48, 211-216.

59. de la Cruz, F. A.; Cowley, J. M., An electron diffraction study of graphitic oxide. *Acta Crystallographica* **1963**, 16, 531-534.

60. Nakajima, T.; Mabuchi, A.; Hagiwara, R., A new structure model of graphite oxide. *Carbon* **1988**, 26, 357-361.

61. Szabo, T.; Berkesi, O.; Forgo, P.; Josepovits, K.; Sanakis, Y.; Petridis, D.; Dekany, I., Evolution of surface functional groups in a series of progressively oxidized graphite oxides. *Chemistry of Materials* **2006**, 18, 2740-2749.

62. Lerf, A.; He, H.; Forster, M.; Klinowski, J., Structure of graphite oxide revisited. *The Journal of Physical Chemistry B* **1998**, 102, 4477-4482.

63. Dreyer, D. R.; Park, S.; Bielawski, C. W.; Ruoff, R. S., The chemistry of graphene oxide. *Chemical Society Reviews* **2010**, 39, 228-240.

64. Horiuchi, S.; Gotou, T.; Fuijwara, M.; Sotoaka, R.; Hirata, M.; Kimoto, K.; Asaka, T.; Yokosawa, T.; Matsui, Y.; Watanabe, K.; Sekita, M., Carbon nanofilm with a new structure and property. *Japanese Journal of Applied Physics Part 2-Letters* **2003**, 42, L1073-L1076.

65. Mkhoyan, K. A.; Contryman, A. W.; Silcox, J.; Stewart, D. A.; Eda, G.; Mattevi, C.; Miller, S.; Chhowalla, M., Atomic and electronic structure of graphene-oxide. *Nano Letters* **2009**, 9, 1058-1063.

66. Wang, G.; Yang, J.; Park, J.; Gou, X.; Wang, B.; Liu, H.; Yao, J., Facile synthesis and characterization of graphene nanosheets. *The Journal of Physical Chemistry C* **2008**, 112, 8192-8195.

67. Erickson, K.; Erni, R.; Lee, Z.; Alem, N.; Gannett, W.; Zettl, A., Determination of the local chemical structure of graphene oxide and reduced graphene oxide. *Advanced Materials* **2010**, 22, 4467-4472.

68. Gomez-Navarro, C.; Weitz, R. T.; Bittner, A. M.; Scolari, M.; Mews, A.; Burghard, M.; Kern, K., Electronic transport properties of individual chemically reduced graphene oxide sheets. *Nano Letters* **2007**, 7, 3499-3503.

69. Pacilé, D.; Meyer, J. C.; Fraile Rodríguez, A.; Papagno, M.; Gómez-Navarro, C.; Sundaram, R. S.; Burghard, M.; Kern, K.; Carbone, C.; Kaiser, U., Electronic properties and atomic structure of graphene oxide membranes. *Carbon* **2011**, 49, 966-972.

70. Lahaye, R. J. W. E.; Jeong, H. K.; Park, C. Y.; Lee, Y. H., Density functional theory study of graphite oxide for different oxidation levels. *Physical Review B* **2009**, 79, 125435-125443.

71. Boukhvalov, D. W.; Katsnelson, M. I., Modeling of graphite oxide. *Journal of American Chemical Society* **2008**, 130, 10697-10701.

72. Liu, L.; Wang, L.; Gao, J.; Zhao, J.; Gao, X.; Chen, Z., Amorphous structural models for graphene oxides. *Carbon* **2012**, 50, 1690-1698.

73. Bae, S.; Kim, H.; Lee, Y.; Xu, X.; Park, J. S.; Zheng, Y.; Balakrishnan, J.; Lei, T.; Kim, H. R.; Song, Y. I.; Kim, Y. J.; Kim, K. S.; Ozyilmaz, B.; Ahn, J. H.; Hong, B. H.; Iijima, S., Roll-to-roll production of 30-inch graphene films for transparent electrodes. *Nature Nanotechnology* **2010**, 5, 574-578.

74. Liu, W.; Jackson, B. L.; Zhu, J.; Miao, C.-Q.; Chung, C.-H.; Park, Y. J.; Sun, K.; Woo, J.; Xie, Y.-H., Large scale pattern graphene electrode for high performance in transparent organic single crystal field-effect transistors. *ACS Nano* **2010**, 4, 3927-3932.

75. Lee, W. H.; Park, J.; Sim, S. H.; Lim, S.; Kim, K. S.; Hong, B. H.; Cho, K., Surface-directed molecular assembly of pentacene on monolayer graphene for high-performance organic transistors. *Journal of the American Chemical Society* **2011**, 133, 4447-4454.

76. Zhou, M.; Zhang, A.; Dai, Z.; Zhang, C.; Feng, Y. P., Greatly enhanced adsorption and catalytic activity of Au and Pt clusters on defective graphene. *The Journal of Chemical Physics* **2010**, 132, 194704-194706.

77. Sicot, M.; Bouvron, S.; Zander, O.; Rudiger, U.; Dedkov, Y. S.; Fonin, M., Nucleation and growth of nickel nanoclusters on graphene Moire on Rh(111). *Applied Physics Letters* **2010**, 96, 093115-093117.

78. Zhou, Z.; Gao, F.; Goodman, D. W., Deposition of metal clusters on single-layer graphene/Ru(0001): factors that govern cluster growth. *Surface Science* **2010**, 604, L31-L38.

79. Zan, R.; Bangert, U.; Ramasse, Q.; Novoselov, K. S., Metal–graphene interaction studied via atomic resolution scanning transmission electron microscopy. *Nano Letters* **2011**, 11, 1087-1092.

80. Zhou, H.; Qiu, C.; Liu, Z.; Yang, H.; Hu, L.; Liu, J.; Yang, H.; Gu, C.; Sun, L., Thickness-dependent morphologies of gold on n-layer graphenes. *Journal of the American Chemical Society* **2009**, 132, 944-946.

81. Chen, X.; Wu, G.; Chen, J.; Chen, X.; Xie, Z.; Wang, X., Synthesis of "clean" and well-dispersive Pd nanoparticles with excellent electrocatalytic property on graphene oxide. *Journal of American Chemical Society* **2011**, 133, 3693-3698.

82. Kaniyoor, A.; Jafri, R. I.; Arockiadoss, T.; Ramaprabhu, S., Nanostructured Pt decorated graphene and multi walled carbon nanotube based room temperature hydrogen gas sensor. *Nanoscale* **2009**, 1, 382-386.

83. Yoo, E.; Okata, T.; Akita, T.; Kohyama, M.; Nakamura, J.; Honma, I., Enhanced electrocatalytic activity of Pt subnanoclusters on graphene nanosheet surface. *Nano Letters* **2009**, 9, 2255-2259.

84. Park, S.; An, J.; Piner, R. D.; Jung, I.; Yang, D.; Velamakanni, A.; Nguyen, S. T.; Ruoff, R. S., Aqueous suspension and characterization of chemically modified graphene sheets. *Chemistry of Materials* **2008**, 20, 6592-6594.

85. Pan, Y.; Gao, M.; Huang, L.; Liu, F.; Gao, H. J., Directed self-assembly of monodispersed platinum nanoclusters on graphene Moire template. *Applied Physics Letters* **2009**, 95, 093106-093109.

86. Hu, L.; Hu, X.; Wu, X.; Du, C.; Dai, Y.; Deng, J., Density functional calculation of transition metal adatom adsorption on graphene. *Physica B: Condensed Matter* **2010**, 405, 3337-3341.

87. Giovannetti, G.; Khomyakov, P. A.; Brocks, G.; Karpan, V. M.; van den Brink, J.; Kelly, P. J., Doping graphene with metal contacts. *Physical Review Letters* **2008**, 101, 026803-026807.

88. Chan, K. T.; Neaton, J. B.; Cohen, M. L., First-principles study of metal adatom adsorption on graphene. *Physical Review B* **2008**, 77, 235430-235448.

89. Zan, R.; Bangert, U.; Ramasse, Q.; Novoselov, K. S., Evolution of gold nanostructures on graphene. *Small* **2011**, 7, 2868-2872.

90. Luo, Z.; Somers, L. A.; Dan, Y.; Ly, T.; Kybert, N. J.; Mele, E. J.; Johnson, A. T. C., Size-selective nanoparticle growth on few-layer graphene Films. *Nano Letters* **2010**, 10, 777-781.

91. Yanjie Gan, L. S. F. B., One- and two-dimensional diffusion of metal atoms in graphene. *Small* **2008**, 4, 587-591.

92. Lee, J.; Novoselov, K. S.; Shin, H. S., Interaction between metal and graphene: dependence on the layer number of graphene. *ACS Nano* **2011**, 5, 608-612.

93. Li, W.; He, Y.; Wang, L.; Ding, G.; Zhang, Z.-Q.; Lortz, R. W.; Sheng, P.; Wang, N., Electron localization in metal-decorated graphene. *Physical Review B* **2011**, 84, 045431-045439.

94. Dimiev, A.; Kosynkin, D. V.; Sinitskii, A.; Slesarev, A.; Sun, Z.; Tour, J. M., Layer-by-layer removal of graphene for device patterning. *Science* **2011**, 331, 1168-1172.

95. Ramasse, Q. M.; Zan, R.; Bangert, U.; Boukhvalov, D. W.; Son, Y.-W.; Novoselov, K. S., Direct experimental evidence of metal-mediated etching of suspended graphene. *ACS Nano* **2012**, 6, 4063-4071.

96. Wu, Y.; Jiang, W.; Ren, Y.; Cai, W.; Lee, W. H.; Li, H.; Piner, R. D.; Pope, C. W.; Hao, Y.; Ji, H.; Kang, J.; Ruoff, R. S., Tuning the doping type and level of graphene with different gold configurations. *Small* **2012**, 8, 3129–3136.

97. Wan, X.; Long, G.; Huang, L.; Chen, Y., Graphene – a promising material for organic photovoltaic cells. *Advanced Materials* **2011**, 23, 5342-5358.

98. Wang, Y.; Chen, X.; Zhong, Y.; Zhu, F.; Loh, K. P., Large area, continuous, few-layered graphene as anodes in organic photovoltaic devices. *Applied Physics Letters* **2009**, 95, 063302-063304.

99. Miao, X.; Tongay, S.; Petterson, M. K.; Berke, K.; Rinzler, A. G.; Appleton, B. R.; Hebard, A. F., High efficiency graphene solar cells by chemical doping. *Nano Letters* **2012**, 12, 2745-2750.

100. Becerril, H. A.; Stoltenberg, R. M.; Tang, M. L.; Roberts, M. E.; Liu, Z.; Chen, Y.; Kim do, H.; Lee, B. L.; Lee, S.; Bao, Z., Fabrication and evaluation of solution-processed reduced graphene oxide electrodes for p- and n-channel bottom-contact organic thin-film transistors. *ACS Nano* **2010**, 4, 6343-6352.

101. Wassei, J. K.; Kaner, R. B., Graphene, a promising transparent conductor. *Materials Today* **2010**, 13, 52-59.

102. Li, S.-S.; Tu, K.-H.; Lin, C.-C.; Chen, C.-W.; Chhowalla, M., Solution-processable graphene oxide as an efficient hole transport layer in polymer solar cells. *ACS Nano* **2010**, 4, 3169-3174.

103. Hirsh, P. B.; Howie, A.; Nicholson, R. B.; Pashley, D. W.; Whelan, M. J., *Electron microscopy of the thin crystals*. 1 ed.; Butterworths: London, **1965**.

104. Gilje, S.; Han, S.; Wang, M.; Wang, K. L.; Kaner, R. B., A chemical route to graphene for device applications. *Nano Letters* **2007**, 7, 3394-3398.

105. Paredes, J. I.; Villar-Rodil, S.; Solis-Fernandez, P.; Martinez-Alonso, A.; Tascon, J. M. D., Atomic force and scanning tunneling microscopy imaging of graphene nanosheets derived from graphite oxide. *Langmuir* **2009**, 25, 5957-5968.

106. Park, S.; An, J.; Potts, J. R.; Velamakanni, A.; Murali, S.; Ruoff, R. S., Hydrazine-reduction of graphite- and graphene oxide. *Carbon* **2011**, 49, 3019-3023.

107. Diaz, J.; Paolicelli, G.; Ferrer, S.; Comin, F., Separation of the sp^3 and sp^2 components in the C1s photoemission spectra of amorphous carbon films. *Physical review. B, Condensed matter* **1996**, 54, 8064-8069.

108. Ago, H.; Kugler, T.; Cacialli, F.; Salaneck, W. R.; Shaffer, M. S. P.; Windle, A. H.; Friend, R. H., Work functions and surface functional groups of multiwall carbon nanotubes. *Journal of Physical Chemistry B* **1999**, 103, 8116-8121.

109. Mattevi, C.; Kim, H.; Chhowalla, M., A review of chemical vapour deposition of graphene on copper. *Journal of Materials Chemistry* **2011**, 21, 3324-3334.

110. Brodie, B. C., On the atomic weight of graphite. *Philosophical Transactions of the Royal Society of London* **1859**, 149, 249-259.

111. Gass, M. H.; Bangert, U.; Bleloch, A. L.; Wang, P.; Nair, R. R.; Geim, A. K., Free-standing graphene at atomic resolution. *Nature Nanotechnology* **2008**, 3, 676-681.

112. Schniepp, H. C.; Li, J.-L.; McAllister, M. J.; Sai, H.; Herrera-Alonso, M.; Adamson, D. H.; Prud'homme, R. K.; Car, R.; Saville, D. A.; Aksay, I. A., Functionalized single graphene

sheets derived from splitting graphite oxide. *The Journal of Physical Chemistry B* **2006**, 110, 8535-8539.

113. Meyer, J. C.; Geim, A. K.; Katsnelson, M. I.; Novoselov, K. S.; Obergfell, D.; Roth, S.; Girit, C.; Zettl, A., On the roughness of single- and bi-layer graphene membranes. *Solid State Communications* **2007**, 143, 101-109.

114. Doyle, P. A.; Turner, P. S., Relativistic Hartree–Fock x-ray and electron scattering factors. *Acta Crystallographica Section A* **1968**, 24, 390-397.

115. Sears, V. F.; Shelley, S. A., Debye-Waller factor for elemental crystals. *Acta Crystallographica Section A* **1991**, 47, 441-446.

116. Brian Shevitski; Matthew Mecklenburg; William A. Hubbard; E. R. White; Ben Dawson; M. S. Lodge; Masa Ishigami; Regan, B. C., Dark-field transmission electron microscopy and the Debye-Waller factor of graphene. *arXiv:1207.0040v1 [cond-mat.mes-hall]* **2012**, 1-10.

117. Tewary, V. K.; Yang, B., Singular behavior of the Debye-Waller factor of graphene. *Physical Review B* **2009**, 79, 125416-125420.

118. Hernandez, Y.; Nicolosi, V.; Lotya, M.; Blighe, F. M.; Sun, Z.; De, S.; McGovern, I. T.; Holland, B.; Byrne, M.; Gun'Ko, Y. K.; Boland, J. J.; Niraj, P.; Duesberg, G.; Krishnamurthy, S.; Goodhue, R.; Hutchison, J.; Scardaci, V.; Ferrari, A. C.; Coleman, J. N., High-yield production of graphene by liquid-phase exfoliation of graphite. *Nature Nanotechnology* **2008**, 3, 563-568.

119. Swift, P., Adventitious carbon—the panacea for energy referencing. *Surface and Interface Analysis* **1982**, 4, 47-51.

120. Kim, S.; Zhou, S.; Hu, Y.; Acik, M.; Chabal, Y. J.; Berger, C.; de Heer, W.; Bongiorno, A.; Riedo, E., Room-temperature metastability of multilayer graphene oxide films. *Nature Materials* **2012**, 11, 544-549.

121. Pantelic, R. S.; Meyer, J. C.; Kaiser, U.; Baumeister, W.; Plitzko, J. M., Graphene oxide: a substrate for optimizing preparations of frozen-hydrated samples. *Journal of Structural Biology* **2010**, 170, 152-156.

122. Fogden, S.; Verdejo, R.; Cottam, B.; Shaffer, M., Purification of single walled carbon nanotubes: the problem with oxidation debris. *Chemical Physics Letters* **2008**, 460, 162-167.

123. Acik, M.; Lee, G.; Mattevi, C.; Chhowalla, M.; Cho, K.; Chabal, Y. J., Unusual infrared-absorption mechanism in thermally reduced graphene oxide. *Nature Materials* **2010**, 9, 840-845.

124. Verdejo, R.; Lamoriniere, S.; Cottam, B.; Bismarck, A.; Shaffer, M., Removal of oxidation debris from multi-walled carbon nanotubes. *Chemical Communications* **2007**, 513-515.

125. Wang, Z.; Shirley, M. D.; Meikle, S. T.; Whitby, R. L. D.; Mikhalovsky, S. V., The surface acidity of acid oxidised multi-walled carbon nanotubes and the influence of in-situ generated fulvic acids on their stability in aqueous dispersions. *Carbon* **2009**, 47, 73-79.

126. Xiaobin Fan, W. P. Y. L. X. L. S. W. G. Z. F. Z., Deoxygenation of exfoliated graphite oxide under alkaline conditions: a green route to graphene preparation. *Advanced Materials* **2008**, 20, 4490-4493.

127. Szabó, T.; Tombácz, E.; Illés, E.; Dékány, I., Enhanced acidity and pH-dependent surface charge characterization of successively oxidized graphite oxides. *Carbon* **2006**, 44, 537-545.

128. Su, Q.; Pang, S.; Alijani, V.; Li, C.; Feng, X.; Müllen, K., Composites of graphene with large aromatic molecules. *Advanced Materials* **2009**, 21, 3191-3195.

129. Park, S.; Ruoff, R. S., Chemical methods for the production of graphenes. *Nature Nanotechnology* **2009**, 4, 217-224.

130. Sloan, J.; Liu, Z.; Suenaga, K.; Wilson, N. R.; Pandey, P. A.; Perkins, L. M.; Rourke, J. P.; Shannon, I. J., Imaging the structure, symmetry, and surface-inhibited rotation of polyoxometalate ions on graphene oxide. *Nano Letters* **2010**, 10, 4600-4606.

131. Gomez De Arco, L.; Zhang, Y.; Schlenker, C. W.; Ryu, K.; Thompson, M. E.; Zhou, C., Continuous, highly flexible, and transparent graphene films by chemical vapor deposition for organic photovoltaics. *ACS Nano* **2010**, 4, 2865-2873.

132. Ganhua, L.; Leonidas, E. O.; Junhong, C., Reduced graphene oxide for room-temperature gas sensors. *Nanotechnology* **2009**, 1-9.

133. Robinson, J. T.; Perkins, F. K.; Snow, E. S.; Wei, Z.; Sheehan, P. E., Reduced graphene oxide molecular sensors. *Nano Letters* **2008**, 8, 3137-3140.

134. Shan, C.; Yang, H.; Han, D.; Zhang, Q.; Ivaska, A.; Niu, L., Graphene/AuNPs/chitosan nanocomposites film for glucose biosensing. *Biosensors and Bioelectronics* **2009**, 25, 1070-1074.

135. Cheng, R.; Liu, Y.; Ou, S.; Pan, Y.; Zhang, S.; Chen, H.; Dai, L.; Qu, J., Optical turn-on sensor based on graphene oxide for selective detection of d-glucosamine. *Analytical Chemistry* **2012**, 84, 5641-5644.

136. Zhang, C.; Lv, W.; Yang, Q.; Liu, Y., Graphene supported nano particles of Pt–Ni for CO oxidation. *Applied Surface Science* **2012**, 258, 7795-7800.

137. Gao, M.; Pan, Y.; Zhang, C.; Hu, H.; Yang, R.; Lu, H.; Cai, J.; Du, S.; Liu, F.; Gao, H. J., Tunable interfacial properties of epitaxial graphene on metal substrates. *Applied Physics Letters* **2010**, 96, 053109-053113.

138. Anton, R.; Kreutzer, P., In situ TEM evaluation of the growth kinetics of Au particles on highly oriented pyrolithic graphite at elevated temperatures. *Physical Review B* **2000**, 61, 16077-16083.

139. Anton, R.; Schneidereit, I., In situ TEM investigations of dendritic growth of Au particles on HOPG. *Physical Review B* **1998**, 58, 13874-13881.

140. Hövel, H.; Becker, T.; Bettac, A.; Reihl, B.; Tschudy, M.; Williams, E. J., Crystalline structure and orientation of gold clusters grown in preformed nanometer-sized pits. *Applied Surface Science* **1997**, 115, 124-127.

141. Zhang, Y.; Franklin, N. W.; Chen, R. J.; Dai, H., Metal coating on suspended carbon nanotubes and its implication to metal-tube interaction. *Chemical Physics Letters* **2000**, 331, 35-41.

142. Zhou, X.; Huang, X.; Qi, X.; Wu, S.; Xue, C.; Boey, F. Y. C.; Yan, Q.; Chen, P.; Zhang, H., In situ synthesis of metal nanoparticles on single-layer graphene oxide and reduced graphene oxide surfaces. *The Journal of Physical Chemistry C* **2009**, 113, 10842-10846.

143. Rasband, W. S. *ImageJ*, U. S. National Institutes of Health: Maryland, USA, **2012**.

144. Kryukov, Y. A.; Amar, J. G., Scaling of the island density and island-size distribution in irreversible submonolayer growth of three-dimensional islands. *Physical Review B* **2010**, 81, 165435-165442.

145. Brault, P.; Thomann, A. L.; Andreazza-Vignolle, C., Percolative growth of palladium ultrathin films deposited by plasma sputtering. *Surface Science* **1998**, 406, L597-L602.

146. Venables, J. A.; Spiller, G. D. T.; Hanbucken, M., Nucleation and growth of thin films. *Reports on Progress in Physics* **1984**, 399 - 459.

147. Bunch, J. S.; Verbridge, S. S.; Alden, J. S.; van der Zande, A. M.; Parpia, J. M.; Craighead, H. G.; McEuen, P. L., Impermeable atomic membranes from graphene sheets. *Nano Letters* **2008**, 8, 2458-2462.

148. Khomyakov, P. A.; Giovannetti, G.; Rusu, P. C.; Brocks, G.; van den Brink, J.; Kelly, P. J., First-principles study of the interaction and charge transfer between graphene and metals. *Physical Review B* **2009**, 79, 195425-195437.

149. Liu, X.; Wang, C. Z.; Hupalo, M.; Lu, W. C.; Tringides, M. C.; Yao, Y. X.; Ho, K. M., Metals on graphene: correlation between adatom adsorption behavior and growth morphology. *Physical Chemistry Chemical Physics* **2012**, 14, 9157-9166.

150. Wu, W.; Liu, Z.; Jauregui, L. A.; Yu, Q.; Pillai, R.; Cao, H.; Bao, J.; Chen, Y. P.; Pei, S.-S., Wafer-scale synthesis of graphene by chemical vapor deposition and its application in hydrogen sensing. *Sensors and Actuators B: Chemical* **2010**, 150, 296-300.

151. Vegard, L., Crystal structure analysis. *Philosophical Magazine Series 6* **1916**, 32, 65-65.

152. Owen, E. A.; Yates, E. L., Precision measurements of crystal parameters. *Philosophical Magazine Series 7* **1933**, 15, 472-488.

153. Büttner, M.; Oelhafen, P., XPS study on the evaporation of gold submonolayers on carbon surfaces. *Surface Science* **2006**, 600, 1170-1177.

154. Callen, B. W.; Lowenberg, B. F.; Lugowski, S.; Sodhi, R. N.; Davies, J. E., Nitric acid passivation of Ti_6Al_4V reduces thickness of surface oxide layer and increases trace element release. *Journal of Biomedical Materials Research* **1995**, 29, 279-290.

155. McIntyre, N. S.; Zetaruk, D. G., X-ray photoelectron spectroscopic studies of iron oxides. *Analytical Chemistry* **1977**, 49, 1521-1529.

156. Benayad, A.; Shin, H. J.; Park, H. K.; Yoon, S. M.; Kim, K. K.; Jin, M. H.; Jeong, H. K.; Lee, J. C.; Choi, J. Y.; Lee, Y. H., Controlling work function of reduced graphite oxide with Au-ion concentration. *Chemical Physics Letters* **2009**, 475, 91-95.

157. Eastman, D. E., Photoelectric work functions of transition, rare-earth, and noble metals. *Physical Review B* **1970**, 2, 1-2.

158. Zan, R.; Bangert, U.; Ramasse, Q.; Novoselov, K. S., Interaction of metals with suspended graphene observed by transmission electron microscopy. *The Journal of Physical Chemistry Letters* **2012**, 3, 953-958.

159. Yong-Hui, Z.; Kai-Ge, Z.; Ke-Feng, X.; Jing, Z.; Hao-Li, Z.; Yong, P., Tuning the electronic structure and transport properties of graphene by noncovalent functionalization: effects of organic donor, acceptor and metal atoms. *Nanotechnology* **2010**, 21, 065201-065207.

160. Chunder, A.; Pal, T.; Khondaker, S. I.; Zhai, L., Reduced graphene oxide/copper phthalocyanine composite and its optoelectrical properties. *Journal of Physical Chemistry C* **2010**, 114, 15129-15135.

161. Liu, W.; Jackson, B. L.; Zhu, J.; Miao, C. Q.; Chung, C. H.; Park, Y. J.; Sun, K.; Woo, J.; Xie, Y. H., Large scale pattern graphene electrode for high performance in transparent organic single crystal field-effect transistors. *ACS Nano* **2010**, 4, 3927-3932.

162. Ren, J.; Meng, S.; Wang, Y. L.; Ma, X. C.; Xue, Q. K.; Kaxiras, E., Properties of copper (fluoro-)phthalocyanine layers deposited on epitaxial graphene. *Journal of Chemical Physics* **2011**, 134, 194706-194716.

163. Anthony, J. E.; Facchetti, A.; Heeney, M.; Marder, S. R.; Zhan, X., n-Type organic semiconductors in organic electronics. *Advanced Materials* **2010**, 22, 3876-3892.

164. Reese, C.; Roberts, M.; Ling, M.-m.; Bao, Z., Organic thin film transistors. *Materials Today* **2004**, 7, 20-27.

165. Bao, Z.; Lovinger, A. J.; Brown, J., New air-stable n-channel organic thin film transistors. *Journal of the American Chemical Society* **1998**, 120, 207-208.

166. Zhang, K. H. L.; Li, H.; Mao, H.; Huang, H.; Ma, J.; Wee, A. T. S.; Chen, W., Control of two-dimensional ordering of F_{16}CuPc on Bi/Ag(111): effect of interfacial interactions. *The Journal of Physical Chemistry C* **2010**, 114, 11234-11241.

167. Yang, J. L. Y. J. L.; Schumann, S.; Jones, T. S., Tuning the morphology and molecular orientation of copper hexadecafluorophthalocyanine thin films by solvent annealing. *Thin Solid Films* **2011**, 519, 3709-3715.

168. Yoon, S. M.; Song, H. J.; Hwang, I.-C.; Kim, K. S.; Choi, H. C., Single crystal structure of copper hexadecafluorophthalocyanine (F_{16}CuPc) ribbon. *Chemical Communications* **2010**, 46, 231-233.

169. Wang, T.; Ebeling, D.; Yang, J. L.; Du, C. A.; Chi, L. F.; Fuchs, H.; Yan, D. H., Weak epitaxy growth of copper hexadecafluorophthalocyanine (F(16)CuPc) on p-sexiphenyl monolayer film. *Journal of Physical Chemistry B* **2009**, 113, 2333-2337.

170. de Oteyza, D. G.; Barrena, E.; Osso, J. O.; Sellner, S.; Dosch, H., Thickness-dependent structural transitions in fluorinated copper-phthalocyanine (F_{16}CuPc) films. *Journal of the American Chemical Society* **2006**, 128, 15052-15053.

171. de Oteyza, D. G.; Barrena, E.; Sellner, S.; Ossó, J. O.; Dosch, H., Molecular structure and growth morphologies of pentacene/fluorinated copper-phthalocyanine heterostructures. *Thin Solid Films* **2008**, 516, 7525-7529.

172. Pandey, P. A.; Rochford, L. A.; Keeble, D. S.; Rourke, J. P.; Jones, T. S.; Beanland, R.; Wilson, N. R., Resolving the nanoscale morphology and crystallographic structure of molecular thin films: F_{16}CuPc on graphene oxide. *Chemistry of Materials* **2012**, 24, 1365-1370.

173. Yang, J. L.; Schumann, S.; Jones, T. S., Morphology and structure transitions of copper hexadecafluorophthalocyanine (F(16)CuPc) thin films. *Journal of Physical Chemistry C* **2010**, 114, 1057-1063.

174. Hill, E. W.; Vijayaragahvan, A.; Novoselov, K., Graphene sensors. *Sensors Journal, IEEE* **2011**, 11, 3161-3170.

175. Schedin, F.; Geim, A. K.; Morozov, S. V.; Hill, E. W.; Blake, P.; Katsnelson, M. I.; Novoselov, K. S., Detection of individual gas molecules adsorbed on graphene. *Nature Materials* **2007**, 6, 652-655.

176. Hübert, T.; Boon-Brett, L.; Black, G.; Banach, U., Hydrogen sensors – a review. *Sensors and Actuators B: Chemical* **2011**, 157, 329-352.

177. Dannetun, H. M.; Petersson, L. G.; Soderberg, D.; Lundstrom, I., A Hydrogen sensitive Pd-MOS structure working over a wide pressure range. *Applied Surface Science* **1984**, 17, 259-264.

178. Dus, R., Hydrogen adsorption and absorption on evaporated palladium films - study by surface-potential measurements. *Surface Science* **1974**, 42, 324-328.

179. Lundström, I.; Shivaraman, S.; Svensson, C.; Lundkvist, L., A hydrogen sensitive MOS field effect transistor. *Applied Physics Letters* **1975**, 26, 55-57.

180. Chu, B. H.; Lo, C. F.; Nicolosi, J.; Chang, C. Y.; Chen, V.; Strupinski, W.; Pearton, S. J.; Ren, F., Hydrogen detection using platinum coated graphene grown on SiC. *Sensors and Actuators B: Chemical* **2011**, 157, 500-503.

181. Shafiei, M.; Spizzirri, P. G.; Arsat, R.; Yu, J.; du Plessis, J.; Dubin, S.; Kaner, R. B.; Kalantar-zadeh, K.; Wlodarski, W., Platinum/graphene nanosheet/SiC contacts and their application for hydrogen gas sensing. *The Journal of Physical Chemistry C* **2010**, 114, 13796-13801.

182. Armgarth, M.; Soderberg, D.; Lundstrom, I., Palladium and platinum gate metal-oxide-semiconductor capacitors in hydrogen and oxygen mixtures. *Applied Physics Letters* **1982**, 41, 654-655.

183. Johnson, J. L.; Behnam, A.; Pearton, S. J.; Ural, A., Hydrogen sensing using Pd-functionalized multi-layer graphene nanoribbon networks. *Advanced Materials* **2010**, 22, 4877-4880.

184. Lange, U.; Hirsch, T.; Mirsky, V. M.; Wolfbeis, O. S., Hydrogen sensor based on a graphene – palladium nanocomposite. *Electrochimica Acta* **2011**, 56, 3707-3712.

185. Chuhei, O.; Ayato, N., Ultra-thin epitaxial films of graphite and hexagonal boron nitride on solid surfaces. *Journal of Physics: Condensed Matter* **1997**, 9, 1-21.

186. Covington, J. A.; Gardner, J. W.; Bartlett, P. N.; Toh, C. S., Conductive polymer gate FET devices for vapour sensing. *IEEE Proceedings-Circuits Devices and Systems* **2004**, 151, 326-334.

187. Eriksson, M., A model of the Temkin isotherm behavior for hydrogen adsorption at Pd-SiO_2 interfaces. *Journal of Applied Physics* **1997**, 82, 3143-3147.

188. Petersson, L. G.; Dannetun, H. M.; Fogelberg, J.; Lundstrom, I., Hydrogen adsorption states at the external and internal palladium surfaces of a palladium-silicon dioxide-silicon structure. *Journal of Applied Physics* **1985**, 58, 404-413.

189. Lundström, I.; Armgarth, M.; Spetz, A.; Winquist, F., Gas sensors based on catalytic metal-gate field-effect devices. *Sensors and Actuators* **1986**, 10, 399-421.

190. Ekedahl, L.-G.; Eriksson, M.; Lundström, I., Hydrogen sensing mechanisms of metal−insulator interfaces. *Accounts of Chemical Research* **1998**, 31, 249-256.

191. Kakalios, J.; Street, R. A.; Jackson, W. B., Stretched-exponential relaxation arising from dispersive diffusion of hydrogen in amorphous silicon. *Physical Review Letters* **1987**, 59, 1037-1040.

192. Sun, Y.; Wang, H. H., High-performance, flexible hydrogen sensors that use carbon nanotubes decorated with palladium nanoparticles. *Advanced Materials* **2007**, 19, 2818-2823.

193. Cabria, I.; López, M. J.; Fraile, S.; Alonso, J. A., Adsorption and dissociation of molecular hydrogen on palladium clusters supported on graphene. *The Journal of Physical Chemistry C* **2012**, 116, 21179-21189.

194. Paul, C. P. W.; Natacha, M.; Zhenni, T.; Yoji, M.; Carey, J. D.; Silva, S. R. P., The importance of oxygen-containing defects on carbon nanotubes for the detection of polar and non-polar vapours through hydrogen bond formation. *Nanotechnology* **2007**, 18, 175701.

195. Sundaram, R. S.; Gómez-Navarro, C.; Balasubramanian, K.; Burghard, M.; Kern, K., Electrochemical modification of graphene. *Advanced Materials* **2008**, 20, 3050-3053.

196. Mubeen, S.; Zhang, T.; Yoo, B.; Deshusses, M. A.; Myung, N. V., Palladium nanoparticles decorated single-walled carbon nanotube hydrogen sensor. *The Journal of Physical Chemistry C* **2007**, 111, 6321-6327.

197. Han, C.-H.; Hong, D.-W.; Kim, I.-J.; Gwak, J.; Han, S.-D.; Singh, K. C., Synthesis of Pd or Pt/titanate nanotube and its application to catalytic type hydrogen gas sensor. *Sensors and Actuators B: Chemical* **2007**, 128, 320-325.

198. Katti, V. R.; Debnath, A. K.; Gadkari, S. C.; Gupta, S. K.; Sahni, V. C., Passivated thick film catalytic type H_2 sensor operating at low temperature. *Sensors and Actuators B: Chemical* **2002**, 84, 219-225.

199. Varghese, O. K.; Gong, D.; Paulose, M.; Ong, K. G.; Grimes, C. A., Hydrogen sensing using titania nanotubes. *Sensors and Actuators B: Chemical* **2003**, 93, 338-344.

200. Wilson, N. R.; Pandey, P. A.; Beanland, R.; Young, R. J.; Kinloch, I. A.; Gong, L.; Liu, Z.; Suenaga, K.; Rourke, J. P.; York, S. J.; Sloan, J., Graphene Oxide: structural analysis and application as a highly transparent support for electron microscopy. *ACS Nano* **2009**, 3, 2547-2556.

201. Novoselov, K. S., Nobel lecture: graphene: materials in the flatland. *Reviews of Modern Physics* **2011**, 83, 837-849.